Wind turbine performance and wake development for various atmospheric, operational and siting conditions

A DISSERTATION
SUBMITTED TO THE FACULTY OF THE GRADUATE SCHOOL
OF THE UNIVERSITY OF MINNESOTA
BY

Kevin Benjamin Howard

IN PARTIAL FULFILLMENT OF THE REQUIREMENTS
FOR THE DEGREE OF
Doctor of Philosophy

Michele Guala, Leonardo P. Chamorro

September, 2014

Acknowledgements

There are many people who I would like to recognize for their assistance and advice along the way. The first group comes from the technical staff at the Saint Anthony Falls Laboratory, and are Richard Christopher, Ben Erickson, Matt Lueker, Chris Milliren (who also provided great support for accessing data from the Eolos database), Erik Steen and Jim Tucker for answering my continual questions and keeping the Eolos wind turbine up and running. SAFL is a very unique facility, but the tech staff makes the lab a world renowned location for fluid mechanics research. Also, a special thank you goes to my co-advisers Leonardo P. Chamorro and Michele Guala for guiding me in research, helping to further develop my skills as an engineer and push me to pursue meaningful research.

In addition, I would like to acknowledge those professors who have made a positive impact on my college career and life, they include Dr. Soon-Jo Chung, Dr. Fred Haan, Mr. Dana Haugli, Dr. Robert Prucka and Dr. John Ziegert. There are many others who have helped me along the way that I also wish to thank, including those in my internships, musical groups, and most especially my parents, Janice and Keith Howard, and family.

Dedication

To my friends and, most especially, my family, whose support has been unwavering throughout this journey.

Abstract

The performance of wind turbines depends entirely on the inflow conditions to which they are subjected. The research presented in this thesis follows the desire to improve wind turbine performance and lifespan by experimentally investigating the impact of a wide range of turbulence conditions on wind turbine operation as well as wake development. Testing was conducted at both the model-scale and full-scale utilizing an atmospheric boundary layer wind tunnel and the Eolos wind research field station, both of which are significant resources available through St. Anthony Falls Laboratory, University of Minnesota. Research findings presented herein provide unique tools and analysis techniques for model-scale wind tunnel testing, which were used throughout to inspect the influence of thermal stability and other perturbations on wind turbine performance, as well as for full-scale testing involving remote sensing devices, meteorological data and turbine operation data. The research conducted for this thesis contributes details pertinent to advancing the knowledge of the wind energy community in the specific areas of turbulence effects on performance (including exact measurements for upwind preview), wake development and meandering, and finally, techniques to modify total wind farm production.

Contents

List of Tables

List of Figures

Chapter 1

Introduction

Wind power has been around for centuries to provide everything from the mechanical force required to grind grain or pump water [2], the force to push a boat across a body of water, and, beginning in the late 19th century, to provide electricity [3]. In the early to mid 20th century, researchers began to focus the design of the wind turbines to produce power more efficiently [4]. The advances in wind turbine performance very much followed aviation research produced by groups like the national advisory committee for aeronautics (NACA), where the design and testing of new airfoils for different flow conditions provided specific details pertaining to the use of airflow to produce lift. Diversity in energy production found a foot hold during the fuel crisis of the late 1970s and a new phase of alternative energy was born. The U.S. government began to support research into wind turbine arrays and studies produced data on turbine interaction between two and three turbines (e.g. [5]). The evolution of wind power to the current turbines is debatable [4], but even as such, wind turbine companies have been attempting to develop new turbine designs that can be operated in a broad range of conditions that seek to approach the theoretical Betz limit for wind power (for two examples of the Betz limit see [6, 7]). Utilizing these turbine designs in energy production has produced the finding that, like the early turbines, when the turbines are operated in situ, production is often below rated power in addition to mechanical failure due to high loading. Therefore, to reduce the reliance on the operation of a single turbine, several wind turbines are grouped together to form a wind farm.

As wind energy receives more interest from countries, as well as private companies,

to produce energy from more alternative energy sources, the problem is now becoming that the best land to place these wind farms is quickly dwindling. To counteract this, researchers and companies alike have begun to design new turbines (i.e. the blimp lifted, high-altitude wind turbines first patented in the U.S. in 1985) and increase the size of the turbine for placement off-shore, for instance the 13.2 megawatt (MW) wind turbine designed by Sandia National Laboratory that uses a rotor diameter of 200 m [8]. These turbine farms (or wind turbine arrays) harness the wind resource in order to produce the most amount of power from windy areas on- (e.g. Alta wind energy center in California with a capacity of 1020 MW) and off-shore (e.g. Horns Rev 2 off the coast of Denmark with a capacity of 209 MW).

Even as the amount of installed wind power reached over 300 Gigawatts [9] in 2013, the many intricate details of power production from the wind remain tough to grasp for the wind energy development community, including, but not limited to, integration into the power grid, efficient transmission of wind produced power to areas of higher population density, and flow field / aerodynamic properties. This thesis sets out to help advance wind energy development in the areas related to turbulent flows, more specifically to the influence of inflow conditions on turbine performance (mean production and turbine loading) and wake flow characterization (pertinent to turbine wake-flow interaction, especially for wind farms).

Several key resources, which are unique to St. Anthony Falls Laboratory (SAFL), were utilized to complete the research presented herein. The majority of the research was conducted in the the SAFL atmospheric boundary layer wind tunnel in the small test section. This main test section has a cross section of 1.7 m by 1.7 m and can be thermally controlled to produce neutral, stable (floor surface cooler than air), or unstable (temperature of the floor surface is higher than the air) thermal boundary layers. This capability allows the researcher to induce a broad range of turbulent regimes and, as utility-scale wind turbines operate in all weather conditions, the ability of the wind tunnel to mimic the atmosphere is of great benefit. Detailed flow information throughout the duration of the research for this thesis was captured through several different techniques, including a Pitot-static tube, Scanivalve pressure taps, thermocouples, hotwire anemometry, and particle image velocimetry. A model wind turbine, originally design and built by Leonardo P. Chamorro and James Tucker to maintain a

fix tip-speed ratio, was used for the testing in the wind tunnel, and for the first time with these turbines, the voltage produced by the DC generators on the turbines was used as measure of turbine performance.

The other significant asset that SAFL maintains, and which was an integral component to the research for this thesis, is the Eolos wind research facility in Rosemount, MN. This 80 acre site is home to a 2.5 MW Clipper Liberty wind turbine, a 130 m meteorological tower and a WindCube V1 light detection and ranging (lidar) wind profiler. The Clipper wind turbine has a rotor diameter of 96 m and a hub height of 80 m and, while initially designed for commercial energy production, the engineering staff at SAFL installed several addition systems during on-site assembly which are used to monitor turbine operation. These research systems include foundation accelerometers, foundation/tower strain gages, blade accelerometers, blade strain gages and nacelle accelerometers. The meteorological tower, which spans the full rotor swept area of the turbine, is located 160 m due south of the turbine and is instrumented with three-component sonic anemometers, cup and vane anemometers, relative humidity sensors and barometric pressure sensor. The booms mounted to the meteorological tower, on which the anemometers are attached, are directed 30^o from due south (or 210^o from due north). All the data from the meteorological tower and turbine supervisory control and data acquisition (SCADA) data are stored on secure servers on-site. The WindCube lidar was an essential part in producing significant findings presented in this thesis, and an initial introduction to remote sensing was attained through my attendance of a PhD summer school co-sponsored by the Danish Technical University and the University of Colorado, Boulder. There I was introduced to great potential of these devices as well as their limitations (i.e. specifically for the WindCube is the unreliable capture of small scale turbulence). So, when the wind tunnel went down for renovation, research was able to continue through the use of the lidar and the other resources at the Eolos research station.

The methodology and focus of the individual chapters in this thesis are presented below.

- Chapter 2 provides the foundation on which all the wind tunnel testing herein is based. The focus of this chapter is on characterizing the operation of the model wind turbine to well defined perturbations (i.e. boundary layer flow, vertical

cylinder) as well as to situations which face utility-scale turbines (i.e. other wind turbines and inhomogeneous terrain). Flow data was collected for this study using a Pitot-static tube as well as a two-component hotwire anemometer. The Pitot profiles were used to provide mean statistics while the hotwire profiles were analyzed to investigate the fluctuations and other higher order statistics. The configurations investigated included placing the model turbine in the wake of a vertical cylinder (to track influence of von Kármán vortices on turbine), in the wake of an upwind turbine and three-dimensional, sinusoidal hill (on the scale of the turbine). The voltage data produced by the turbine in these different experiments were analyzed and provided the turbine operation characteristics from the point of view of the turbine.

- In Chapter 3, the turbine model and the related diagnostic tools developed in the previous chapter were put to the test by placing the turbine into three complex thermal stability regimes, which is one of the unique capabilities of the St. Anthony Falls Laboratory boundary layer wind tunnel. These tests were designed to inspect the influence of atmospheric stability and inhomogeneous terrain on turbine performance. The nine different configurations constructed to tested the turbine operation for three turbine perturbations (baseflow, upwind turbine, upwind hill) in each of the three thermal stability conditions (neutral, stable and convective). Flow information for this chapter was acquired through Pitot-static tube and thermocouple profiles paired with spatially resolved, wall-normal particle image velocimetry (PIV). Two cameras were used to simultaneously acquire the inflow and wake of the test turbine. A detailed analysis of the boundary layer flow is presented through the use of the two-point correlation to understand the change in turbulence characteristics between the three different thermal regimes. Voltage (mean, fluctuations, and spectral analysis) and PIV data then provide complimentary details to locate the main source of change in the mean and fluctuating voltage output between all of the cases.

- The specific influence of the wind flow at different elevations, or as it is called in the wind turbine controls community, upwind preview, is the main focus of Chapter 4. The Eolos wind research station provided the perfect setting to investigate

changes in inflow (data samples were collected for different wind directions, speeds and thermal regimes) and the resulting production of a utility-scale wind turbine. For inflow measurement, the WindCube lidar was placed at various distances upwind of the turbine in the primary wind direction. The velocity time signals measured by the lidar were then correlated to the power production time signal and blade strain time signal. From this correlation, the wind elevation with the most influence on turbine performance was located. To test if the same elevation is true for the model wind turbine in the wind tunnel, the spatially resolved PIV data from the camera upwind of the turbine was processed and placed into a time signal which was then correlated to voltage output of the model turbine. Once the process to correlate PIV and voltage proved to be robust, further configurations (specifically the test turbine in the wake of another turbine, which is pertinent for application within wind farms) could be tested in the wind tunnel. Prior to this, wake data taken with the lidar in the wake of the Eolos turbine was compared to wake data of the model turbine to ensure agreement.

- PIV is once again implemented in Chapter 5 to study the model wind turbine, however, this time the cameras are oriented to capture one continuous field of view in a wall-parallel plane, placed at the turbine hub height. The goal of this chapter is to statistically quantify the wake meandering produced by a wind turbine. This is accomplished through a link between the wind turbine wake and meanders studied in nature by the geomorphology community, such as river meanders. The PIV field of view captures a significant portion of the wake (3.6 D in the wind direction and 1.8 D in the lateral) such that the mean statistics of the wake meander and higher order statistics (slope, curvature and correlation) can be computed reliably. The information presented in this chapter not only can be used to produce more accurate wake models, but it also takes a significant step forward toward truly understanding wind turbine wake dynamics.

- Chapter 6 presents research which inspects the ability of two methods, implemented by changing the turbine control algorithm, to increase the total production of a wind farm with turbines aligned in the mean wind direction. It is reviewed

and presented in the chapter that a wind farm with staggered turbines is far superior to an aligned one, however, as the wind direction is never constant, a case may arise where a farm that is staggered in one wind direction may become aligned for another wind direction. Therefore, testing here in the wind tunnel is conducted on an aligned farm with changes that can be easily put into operation on existing wind turbines. The two methods, which have been inspected before computationally for one and two turbines, are yaw misalignment and tip-speed ratio adjustment. Yaw misalignment merely turns the turbine out of direct alignment with the mean wind direction and, as shown previously, reduces the efficiency as well as the structural loading. Tip-speed ratio adjustment (often called derating the turbine) changes the tip-speed ratio away from the most efficient operating condition, which also reduces the output of the turbine, but allows the lost wind to travel downwind to the subsequent rows in the turbine array. Analysis is carried out by inspecting the voltage output from the model wind turbines and wall-parallel PIV is used to provide supporting details.

- In Chapter 7, a brief summary of the significant findings from the completed work in the thesis is provided.

Significant contributions from this work include the model wind turbine, which was characterized for monitoring true turbine performance through the testing and analysis presented in Chapter 2. From this characterization, the output from the model turbines could then be analyzed for any real-world representative flow scenario with the added benefit of conducting the tests within a wind tunnel, which allows the control of the testing variables. To ensure the robustness of wind tunnel data, flow measurements from a lidar remote sensing device were coupled with turbine SCADA data taken at the Eolos wind research facility and were found to have a good representative comparison to inflow and wake measurements in the wind tunnel. In addition, and arguably the greatest contribution of this thesis, is the upwind preview information provided by correlating the inflow time signals to turbine performance (mean power and structural loading) at both the model-scale and full-scale. This upwind preview data is of great importance as the wind turbine controls community develops new methods to harness the wind more efficiently. Chapter 5, to the best of my knowledge, is first time detailed

statistical analysis has been presented on the precise turbine near wake meandering characteristics. Finally, implementing the findings from all the previous content, two methods to increase wind farm production, which in literature has only been completed with one or two turbines, are investigated in a large wind farm.

Chapter 2

Characterizing the response of a wind turbine model under complex inflow conditions

The focus of this chapter is to investigate and understand the response of the model wind turbine to a range of inflow conditions. Here a horizontal axis wind turbine model was tested in a closed-circuit wind tunnel under various inflow conditions. Separate experiments placed the test turbine (i) in the wake of a three-dimensional, sinusoidal hill, (ii) in the wake of another turbine and (iii) in the turbulent boundary layer, as a reference case. Simultaneous high-frequency measurements of the turbine output voltage, rotor angular velocity along with streamwise and wall normal velocity components were collected at various locations through the turbine's miniature DC generator, a high-resolution laser tachometer and cross-wire anemometer, respectively. Validation trials were conducted first in order to characterize the test turbine's output and response to the baseline turbulent boundary layer. Analysis was performed by comparing the cross-wire anemometry measurements of the incoming flow with the turbine voltage output to investigate the unsteady rotor kinematics under different flow perturbations. Using spectral, auto- and cross-correlation methods it was found that the flow structures developing downwind of the hill leave a stronger signature on the fluctuations and spectrum of the rotor angular velocity, as compared to those flow structures filtered

or deflected by placing a turbine upwind. In summary, we show that the effects on downwind turbines of complex terrain and multi-turbine arrangements are consistent with the induced modifications by the hill or turbine on the large scale structures in the incoming flow.

Originally published as:

Howard, K. B., Hu, J. S., Chamorro, L. P. and Guala, M. (2014), Characterizing the response of a wind turbine model under complex inflow conditions. Wind Energ. doi: 10.1002/we.1724

2.1 Introduction

Before large scale wind farms can utilize the wind's energy potential, several engineering, environmental and technical aspects need to be addressed in depth. For instance, the life span and optimum performance of wind turbines within wind farms can be severely affected by the topographical features of the surrounding terrain, especially those in the predominant wind direction. Predicting important parameters of wind turbines in complex terrains, such as power production, turbine fatigue life, and peak velocities, is complicated and requires the use of complex experiments (Yang et al. 2012 [10]) or very sophisticated computational fluid dynamics (CFD) tools (O'Sullivan et al. 2010 [11], Yang et al. 2012 [12]).

Recent CFD efforts have focused on the turbine interaction (Troldborg 2011 [13]) as well as the estimation of power production in wind farms and wake flow patterns in variable topography (Politis et al. 2012 [14]). In general, relatively small terrain variations can induce noticeable effects on wind turbines. In fact, a computational study by Gravdahl and Rorgemoen (2002 [15]) has shown that with variations in ground elevation of $z/z_{hub} \approx 0.23$, the power production of turbines can vary up to 25%. Experimental studies at laboratory and field scales can significantly contribute to our understanding of the interaction between wind turbines and the flow turbulence developed over mild and complex terrains. In particular, laboratory experiments have shown that varying wind loads (e.g. Hu et at 2012 [16]), terrain characteristics (e.g., Yang et al. 2012 [10]) and wind turbine layouts (e.g., Chamorro et al. 2011 [17]) strongly impact the performance

of wind turbines. Energetic turbulence patterns are induced in terrains of complex topologies and can severely affect the performance of a wind turbine and/or wind farm. A hill is a particular case of terrain inhomogeneity that induces spectral modifications in the surrounding atmospheric boundary layer (Tampieri et al. 2003 [18]), and therefore affects the overall performance of wind power plants. Moreover, wake characteristics of wind turbines are sensitive to surface roughness changes (Chamorro and Porte-Agel 2009 [19]). All of these studies provide information which can be used to develop efficient wake models to reduce the cost of wind turbine development and improve layout optimization criteria (Chamorro et al. 2009 [20], Gonzales-Longatt et al. 2012 [21], Husien et al. 2012 [22], Meneveau 2012 [23]). Vertical transport of turbulent kinetic energy, which is the main source of replenishing kinetic energy within wind farms (Cal et al. 2010 [24], Lebron et al. 2012 [25]), can be affected by the terrain topology. In the end, characterizing the flow turbulence in various topographic conditions is, therefore, a key component in any wind farm project.

This investigation uses model turbines as a probe for wind energy harvesting in controlled wind tunnel experiments, where turbines facing topographical disturbances serve as a scaled representation of a wind power plant in complex terrain. Two typical wind farm flow configurations, (i) sinusoidal hill-turbine and (ii) turbine-turbine interactions, are examined to elucidate relevant flow features both into and within wind farms. The voltage signal from a model turbine is tested for wind energy diagnostics and to inspect how the turbine responds to turbulent flow structures. Simultaneous acquisition of turbine voltages in a wind farm setting will allow wind tunnel experiments to be conducted with multiple turbines and a combination of topographic disturbances with the goal of finding optimal siting in complex terrain and layout conditions. A validation procedure, which consisted of three stages, is presented herein. The first stage characterizes the mean voltage at various incoming velocities. The next step delves into a study of the voltage temporal variation by focusing on the impact of a cylinder placed upwind of the turbine on its centerline. In the third stage of validation, the turbine voltage spectra is inspected and used to evaluate the ability of the voltage to capture energetic, unsteady motions, added to the inflow, again, by a vertical cylinder. This document is organized as follows. Section 2.2 explains the wind tunnel setup and instrumentation used. Section 2.3 is devoted to the voltage validations tests, while Section 2.4 discusses

Table 2.1: Model turbine diameter D and flow characteristics for TBL, profiles given in Figure 2.1.

D $[m]$	δ $[m]$	ν $[m^2\ s^{-1}]$	u_τ $[m\ s^{-1}]$	U_{hub} $[m\ s^{-1}]$	U_δ $[m\ s^{-1}]$	Re_τ [-]	Re_D [-]	Re_δ [-]
0.128	0.6	1.5e-5	0.34	7.1	8.3	13600	60587	332000

the results from the turbine-turbine and hill-turbine studies through the study of mean, fluctuating, and spectral statistics from both cross-wire anemometry measurements and turbine voltage output. Also included is a detailed examination of the turbine-turbine case by way of auto- and cross-correlation of the turbine voltage signal.

2.2 Experimental Setup

Testing was conducted in the closed-circuit wind tunnel at Saint Anthony Falls Laboratory, University of Minnesota. The wind tunnel is 37.5 m in length, with a 16 m test section whose cross-section is 1.7 m by 1.7 m. Just upstream of the main test section is a contraction which has an area ratio of 6.6:1. A flow straightener composed of aluminum honeycomb and a wire mesh generates uniform flow at the contraction inlet.

The model turbine operated in a zero pressure gradient turbulent boundary layer, developed over a smooth wall, under neutral thermal conditions. A 0.04 m picket fence placed at the beginning of the test section was used as a flow tripping mechanism to vary the boundary layer thickness δ between specific experiments. The negligible pressure gradient was achieved by adjusting the wind-tunnel ceiling height, while thermally neutral conditions were obtained by controlling both the floor and air temperatures independently. The air temperature was regulated through the use of a heat exchanger located just after the diffuser, downstream of the tunnel's driving fan. The floor temperature was maintained by circulating liquid through passages in the aluminum plates that make up the floor. Figure 2.1 displays the resulting tripped boundary layer (TBL) profile at the turbine location. Corresponding flow characteristics are displayed in Table 2.1. In the table, the Reynolds numbers are defined as, $Re_\tau = u_\tau \delta/\nu$, $Re_D = U_{hub} D/\nu$ and $Re_\delta = U_\delta \delta/\nu$.

The wind turbine model consisted of a fixed pitch, three-blade (GWS/EP-5030x3)

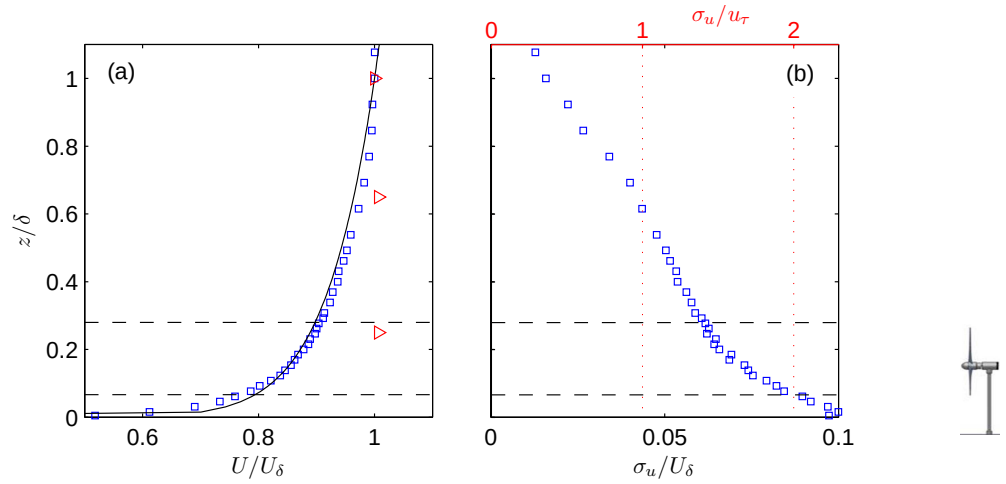

Figure 2.1: (a) Normalized streamwise velocity profile of the approach velocity from the TBL □ under neutral stratification, the solid black profile is the power law fit with an exponent of 0.085, and uniform inflow ▷; (b) normalized velocity r.m.s. σ_u/U_δ (where $U_\delta = U(z/\delta = 1)$) and σ_u/u_τ (where u_τ is the friction velocity), both shown as □. The black, horizontal, dashed lines give the location of the top and bottom tip of the rotor.

rotor with a diameter D =0.128 m attached to DC generator at a hub height of 0.104 m. The turbine hub location was placed within the lowest twenty-five percent of the boundary layer, similar to utility-scale turbines in the atmospheric boundary layer. The rotor is attached directly to the shaft of the DC generator, which produces the voltage signals used herein by passing the three poles (wire loops with precious metal brushes for commutation) on the rotor of the generator through the magnetic field. For the studies presented within this document, the voltage was produced in an open-circuit form (i.e. the poles of the motor were attached directly to the data acquisition system) and hence no power was captured. The turbine tip-speed ratio $\lambda = \Omega r/U_{hub}$ was held constant at approximately 4.5 by motor (motor construction leads to electrical and frictional torques increase proportionally with aerodynamic torque) and blade selection, no additional voltage or resistance was applied from an outside source to maintain the tip-speed ratio. Blade characteristics (pitch and chord length as function of the radius) of the turbine can be found in Table 2.2. This tip-speed ratio was selected as it is within of the range for tip-speed ratio of utility-scale turbines (λ between 3 and 9). Matching the full size tip-speed ratio allows the tip vortices to describe the same helical structure.

Table 2.2: Chord length (c) and twist angle (α) as a function of blade radius (r) of the blades.

r / D	0.0492	0.138	0.188	0.239	0.292	0.342	0.389	0.437	0.500
c / D	0.0890	0.115	0.116	0.116	0.112	0.102	0.0929	0.0770	0.0526
$\alpha[^\circ]$	13.4	18.0	19.0	20.0	17.6	13.5	12.6	10.8	10.0

Another parameter of particular importance is the height of the turbine with respect to the boundary layer. This ratio, specifically to ensure that the largest flow structures, of order of 6-10 delta (see Guala et al. 2011 [26]) are much longer than the turbine generated structures (governed by the tip-speed ratio). The reduction in Reynolds number at the small scale means that the turbulence in the near wake ($x/D < 1$) is driven by the specific geometry of the turbine and would not precisely match full scale turbulent structures. Geometric and kinematic similarity is approximately achieved, and Chamorro et al. (2012) [27] presented that the main flow statistics become independent of Reynolds number near $Re_D \approx 10^5$.

The blades employed herein are very nearly flat. A combination of wind tunnel and engine dynamometer tests were conducted to evaluate the performance of the rotor on the model turbine. In the wind tunnel with a constant hub velocity, the tip-speed ratio of the turbine was varied by applying a voltage to the DC generator which opposed the rotor rotation induced by the airflow with an external DC power supply. A few different hub velocities were selected. At each velocity, multiple resistive voltages were applied and the subsequent rotor angular velocity for each velocity-voltage combination was recorded. Moving to the engine dynamomter, the DC generator from the model wind turbine was attached to a stepper motor through a custom drivetrain (see picture for setup in Figure 2.2a). A symmetric beam was then mounted to the body of the DC generator and zeroed to a level state. The stepper motor was then driven at the rotational speeds that were previously recorded in the wind tunnel and, once the DC generator was up to required speed for each case, the resistive voltage was applied. Weights were then added on the moment arm until the beam reached the zeroed orientation. The product of the weight and moment arm equated to the aerodynamic torque produced by the blades for that given tip-speed ratio. The resulting power coefficient ($C_P = \frac{P_{produced}}{P_{available}}$) for the uniform inflow is shown in Figure 2.2b. $C_{P_{max}}$ was found to

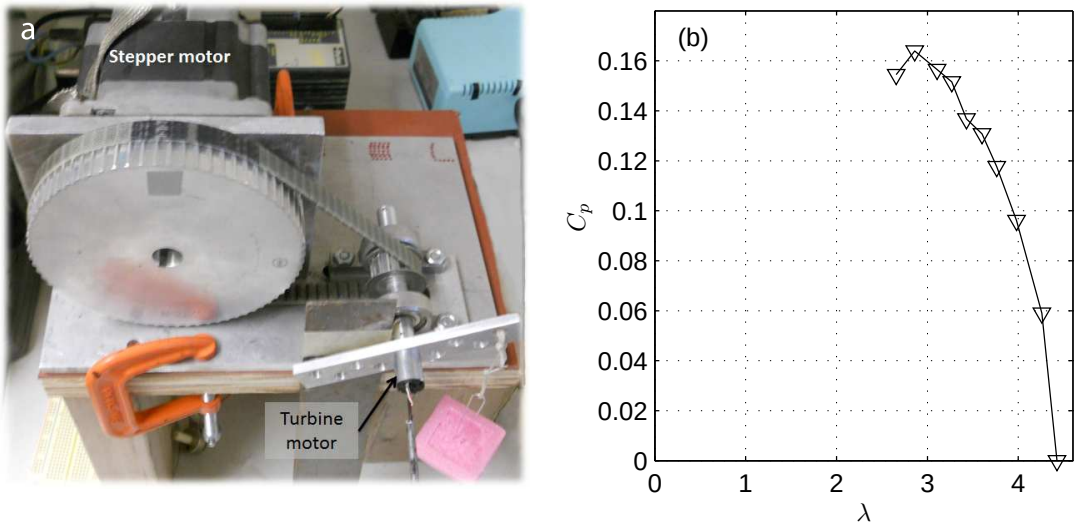

Figure 2.2: Testing performance of model wind turbine, (a) photograph of engine dynamometer test stand and (b) C_P curve versus tip-speed ratio.

be just over 0.16 at $\lambda \approx 3$. Note that for the experiments presented herein, the turbine was unloaded (frictional loading only), and thus was operating at the highest tip-speed ratio ($\lambda \approx 4.5$) with a $C_P = 0$.

A constant temperature anemometer (CTA) cross-wire was used to measure the streamwise and vertical velocity components with high-resolution. The cross-wire sensor consisted of two tungsten wires 5 μm in diameter. The sensor was connected to an A.A. Lab Systems AN-1003 10-channel CTA system. It was used to obtain the mean velocity profile and turbulence statistics of various flow conditions. Selected vertical profiles were taken between the heights of 0.0032 and 0.70 m ($0.031 < z/z_{hub} < 6.73$), with measurements taken every 0.01 m for heights between 0.01 and 0.20 m; above 0.20 m, the interval was increased to 0.02 m. At each measurement location, flow velocity was collected at a frequency of 10 kHz for a time interval of 120 s (sampling rate and time for all cases unless otherwise noted). The cross-wire was calibrated before and after the experiments to check for potential voltage drift. The calibration used nine velocities equally spaced, providing a velocity range larger than encountered in the testing. At each of the nine velocities, data was acquired in increments of ten degrees between negative and positive 30 degrees, with respect to streamwise (x) axis. The temperature

during the calibration was controlled to an accuracy of $\pm 0.2°$C with respect to the 22.5°C test temperature. A look-up table calibration method (using cubic-spline interpolation) was used to estimate the two instantaneous velocity components from the cross-wire voltage signals (Brunn 1995 [28]).

A Monarch Instruments laser tachometer was used to measure the angular velocity of the wind turbine. The tachometer was positioned to measure the time of consecutive blade passing at the top tip location. Highly reflective tape was placed near the tip on each of the three blades of the rotor to ensure a reading from the tachometer. A similar concept was used by Cal et al. (2010)[24] to measure rotational velocity of a model turbine. A stroboscopic light was used while testing the turbine under uniform inflow to measure the rotor rotation rate.

A three-dimensional, sinusoidal hill model and a wind turbine model were placed, for different experiments, upstream of the instrumented model turbine to study the influence of the incoming flow and terrain topography on the wind turbine. The hill had a height of 0.10 m, designed to coincide with the turbine hub height (0.104 m). The base of the hill had a diameter of 0.30 m, which then tapered as a function of height with respect to the defining sinusoid (Figure 2.3 shows model hill in situ). For each case, the test turbine was placed six rotor diameters ($6D$) downstream of the preceding obstacle and measurements were taken at $6D$ downwind to find the inflow condition for the turbine. The blockage ratio for the hill and turbine were 0.52% and 0.45%, respectively, and did not influence the zero pressure gradient boundary layer growth, as measured by static pressure ports equispaced in the test section.

2.3 Validation

The voltage signal produced by the turbine is characterized prior to investigating the complex topographic wind farm studies. For validation, a series of experiments were conducted which placed the model turbine under specific inflow conditions where the turbine response could be evaluated in light of the estimated incoming flow statistics.

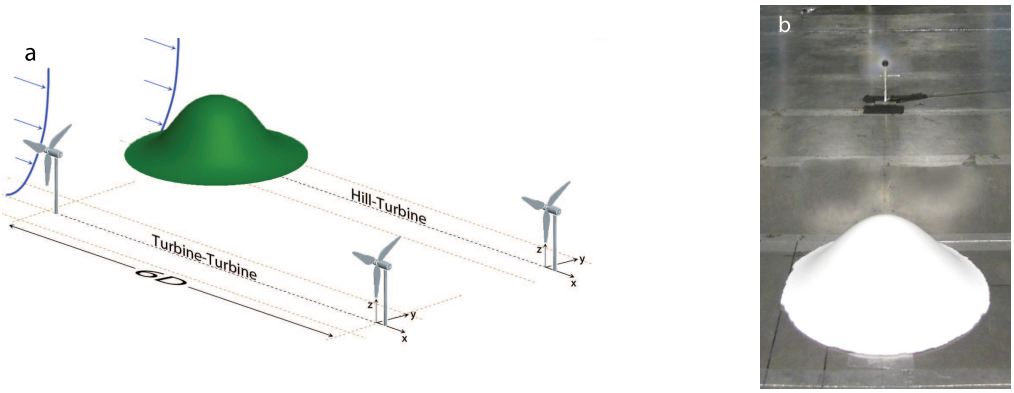

Figure 2.3: Schematic of the turbine-turbine and hill-turbine configurations (a) and photograph of the hill-turbine setup in the boundary layer wind tunnel (b).

2.3.1 Mean voltage

The first experiment was performed in the TBL by varying the mean velocity measured at hub height, U_{hub}. The turbine model was placed 13 m downwind from beginning of the test section and the turbine generator was connected to the data acquisition system. The mean voltage (V) produced by the wind turbine model was acquired simultaneously with the hub velocity, measured by a Pitot-static tube offset in the spanwise direction at the same streamwise position as the turbine model. The angular velocity of the turbine model was also estimated with a stroboscopic light for all velocities in this case. Figure 2.4 shows that (i) the voltage V and (ii) the mean rotational velocity Ω vary linearly with the hub velocity U_{hub}. Note that while the voltage is influenced by the flow velocity it should not be assumed to be power output, as the power produced is proportional to the cube of the incoming velocity. Again, no load was applied to maintain tip-speed ratio, but frictional and internal electrical loads applied an opposing torque that increased linearly with aerodynamic torque.

2.3.2 Voltage fluctuations

A series of runs were performed at approximately 13 m downwind from the beginning of the test section with the flow trip in place. In order to induce appreciable temporal variations of the inflow condition and test the capabilities of the voltage to respond to large scale flow perturbations (on the order of the rotor scale), the turbine was

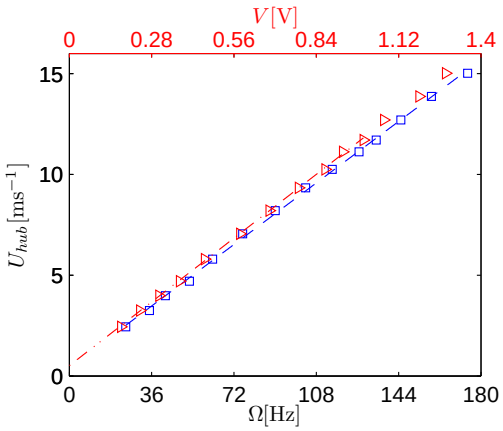

Figure 2.4: Linear relationship between mean voltage (▷) and turbine angular frequency (□) with the hub velocity.

positioned downwind of a vertical cylinder with a diameter $d_c = 0.22\ m$ ($d_c/D = 1.7$). Simultaneous high-frequency measurements of turbine voltage and turbine rotational velocity, from the laser tachometer, were obtained with a sampling frequency of 60 kHz at $U_{hub} = 4$ & $7\ m\ s^{-1}$. Additional measurements at 10 kHz were taken at freestream velocities of 4, 5.5, 7, 8.5 $m\ s^{-1}$ with and without the cylinder. The goal of this set of experiments was to statistically compare the fluctuation of the rotational velocity with the fluctuation of the turbine voltage.

The fluctuation of the voltage σ_v/V was compared to the fluctuation of the angular velocity σ_ω/Ω. The resulting values are within $\pm 5\%$ of each other (see Table 2.3), suggesting that the voltage signal can be used to estimate the turbine rotor unsteadiness induced by the turbulent flow. The resulting turbine voltage signal can therefore be used as a non-intrusive method of measuring turbine response.

The next step compares the fluctuations of the voltage output and the rotor angular velocity with the streamwise velocity fluctuation of the incoming flow. The rotor is expected to respond to mostly large scale velocity fluctuations (Chamorro et al. 2013 [29]), implying that the voltage fluctuations should be smaller when compared to the streamwise velocity fluctuations measured at the same location and inflow conditions. A cross-wire anemometer was used to measure the mean and fluctuating vertical velocity

Table 2.3: Mean statistics for the instantaneous turbine voltage v and angular velocity ω. Measurements were taken in the TBL with and without a cylinder of diameter 0.22 m, placed $6D$ upstream, centered on the turbine.

U_{hub} $[m/s]$	Cylinder	V [V]	σ_v [V]	$I_v = \frac{\sigma_v}{V}$	Ω [s]	σ_ω [s]	$I_\omega = \frac{\sigma_\omega}{\Omega}$	$\lvert\frac{I_v - I_\omega}{I_v}\rvert$ [%]
4.0	No	0.302	0.0104	0.0345	0.0248	8.28E-04	0.0334	3.19
	Yes	0.292	0.00940	0.0322	0.0256	8.00E-04	0.0313	2.80
7.1	No	0.556	0.0147	0.0264	0.0135	3.72E-04	0.0276	4.55
	Yes	0.533	0.0163	0.0306	0.0141	4.45E-04	0.0315	2.86

Table 2.4: Comparison between voltage and streamwise velocity statistics at different heights in the TBL with no cylinder. The cross-wire measurements shown as bottom, hub and top tip of the rotor are at $z = 0.04$, 0.10 and 0.17 m, respectively.

Baseline Case	Turbine V [V]	σ_V [V]	I_v	Cross-wire U $[m\ s^{-1}]$	σ_u $[m\ s^{-1}]$	I_u	$\frac{I_v}{I_u}$ [%]
Turbine	0.573	0.0157	0.0274				
Bottom Tip				6.47	0.658	0.102	26.9
Hub Height				7.12	0.547	0.0769	35.6
Top Tip				7.49	0.461	0.0615	44.6

profile at the same planar location of the turbine rotor. The two experiments were performed with a hub velocity of $U_{hub} = 7\ m\ s^{-1}$ in the TBL. Both the velocity and voltage signals were low-pass filtered with the same cutoff frequency, selected to include the turbine frequency (see next subsection for the definition of cutoff frequency).

Table 2.4 reports the mean statistics of the turbine voltage and streamwise velocity in the TBL at various heights corresponding to key vertical locations of the rotor components, namely the highest and lowest blade positions (top tip and bottom tip respectively) and the hub height. Results show that the turbine voltage captures approximately 27% of the turbulent fluctuations with respect to the cross-wire located at the bottom tip ($z = 0.04$ m), 36% at hub height ($z \approx 0.10$ m) and 45% at the top tip ($z \approx 0.17$ m). The variation in the rotor angular velocity can be thought of as a time-scale filtered and rotor plane averaged response to turbulent fluctuations, which incorporates the reduction of turbulence as the distance from the wall increases.

2.3.3 Turbine voltage spectra

In the previous set of experiments, the turbine voltage statistics were compared with the rotor velocity statistics and observed to be able to describe quantitatively the basic response of the turbine model. Here, the comparative analysis is extended further to investigate the spectral properties of both signals. Figure 2.5 shows that the raw energy density spectrum of the voltage signal has many high-frequency peaks. The first peak represents the turbine frequency, hereinafter indicated as f_t and appears in the voltage spectrum because of the construction of the DC generator. Recall that the generator has three poles, each which add to the voltage production equally. The subsequent voltage signal has three peaks for a single rotation of the rotor and, thus, the spectral decomposition in Figure 2.5 will include f_t as well as its higher order harmonics. Spectral estimates of the turbine frequency are confirmed by two independent measurements: i) a stroboscopic light, (ii) a tachometer, measuring the average time associated with the passage of three turbine blades (one revolution). The second peak in the voltage spectra represents the blade passing frequency $f_b = 3f_t$, while higher frequency peaks indicate harmonics. To remove both extraneous signal noise and the harmonics, a cutoff frequency was selected at a point where the turbine spectrum veers from downward slope of the turbulent spectrum. As shown by Chamorro et al. (2013) [29], the turning point depends on the turbine tip-speed ratio. The location where this deviation occurred was obtained by comparing the energy of the signal to the noise, all while maintaining the turbine frequency in the retained portion of the spectrum. The comparison between different methods of obtaining the turbine frequency is shown in Table 2.5. This table shows that spectra from the turbine voltage can be used to find the turbine frequency.

A series of tests positioning the turbine in the wake of vertical cylinders were performed to evaluate other features of the rotor kinematics, besides the turbine frequency; such as the effect of a topographic perturbation (as a generic source of large scale fluctuations in the incoming flow) on the mean and fluctuating components of the rotational velocity. A series of simple experiments designed to add a well-defined and discernible frequency to the flow upwind of the turbine were performed before attempting to provide a description of turbine performance with complex boundary conditions. Vertically oriented cylinders with diameters $d_c = 0.034\ m$ ($d_c/D = 0.27$) and $0.042\ m$ ($d_c/D = 0.33$) and heights of approximately $0.6\ m$ were used, in different runs, to induce theoretically

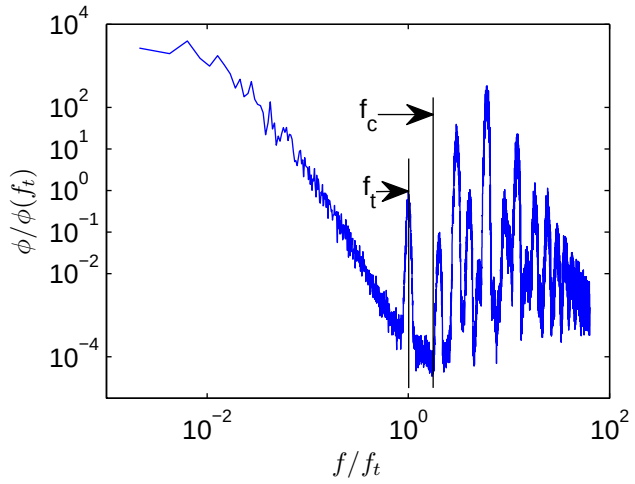

Figure 2.5: Raw turbine voltage spectrum obtained in the TBL with a hub velocity of 4 $m\ s^{-1}$. f_c and f_t are the cutoff frequency and turbine frequency, respectively.

predictable shedding frequencies in the same range of hub velocities described in the previous section. These specific diameters were selected after inspecting nine different cylinders due to their shedding frequency and its location relative to the turbine frequency. The von Kármán equation (2.1) was used to estimate the shedding frequency based on the diameter of the cylinder and a uniform incoming velocity (von Kármán 1911 [30]):

$$f_s = \frac{0.198U}{d_c}\left(1 - \frac{19.7}{Re}\right); \tag{2.1}$$

where f_s is the shedding frequency, U is the average streamwise velocity component and Re is the Reynolds number based on the cylinder diameter d_c. As equation (2.1) was developed for a uniform inflow condition, the shedding frequencies produced by the cylinder in the TBL were assumed to be near, but not exactly, the value produced from the equation. In the TBL, the shedding frequency of the cylinder was found to contain a small range of frequencies, rather than one specific frequency. This is attributed to the non-uniform velocity profile found in the boundary layer. However, please note that

Table 2.5: Comparison of the turbine frequency between measured values from (i) a stroboscopic light f_t^{Sb} and calculated value from (ii) the first peak in the voltage spectra f_t^{Sp} (value verified with turbine frequency prediction equation using the mean voltage). Measurements were taken in the TBL.

U_∞ $[m\ s^{-1}]$	f_t^{Sb} [Hz]	f_t^{Sp} [Hz]	$(f_t^{Sb}$ - $f_t^{Sp})/\ f_t^{Sp}$ [%]
2.4	24.65	22.25	10.8
4.0	42.00	39.75	5.66
7.1	75.83	75.25	0.77
10.3	115.00	111.40	3.23

the mean velocity varied only 11% over the vertical reach of the rotor. The goal is to identify the signature of the cylinder wake in the frequency domain of the voltage spectra. The power spectral density of both the high temporal resolution voltage and tachometer signals are compared with the shedding frequency of the cylinder. The signature of the shedding frequencies from two different sized cylinders can be seen in the voltage spectra shown in Figure 2.6.

Note that the predicted shedding frequency is within the spreading of the peak in the voltage spectra and it is not affected by the distance between the cylinder and the turbine (see Figure 2.7 and Table 2.6). In Figure 2.7, the frequency is normalized by the turbine frequency from each case, but the cylinder shedding frequency (which is constant in this figure) does not have a noticeable shift because the turbine frequency, that depends on the mean velocity across the rotor, only varies by approximately 2.5 Hz between the three cases (equating to just under 4% of the mean turbine frequency). A quantitative comparison of measurements and predicted values is shown in Table 2.7. It is important to remark that the voltage spectra has been low-pass filtered using the aforementioned cutoff frequency f_c. Different analog and digital filters were tested to ensure that the filter did not alter the data in any way. The adjusted parameters included the type of analog filter and the cutoff frequency (not shown here).

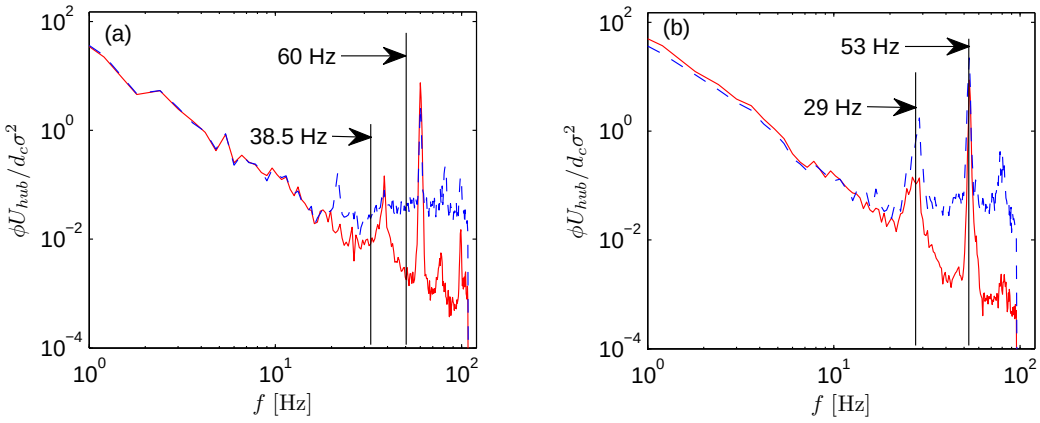

Figure 2.6: Comparison of tachometer and voltage spectra between (a) 0.034 m and (b) 0.042 m cylinder placed $4d_c$ upstream with a hub velocity of 7 $m\ s^{-1}$. Solid line represents the turbine voltage spectrum and the dashed line is the tachometer spectrum. The first and second spectral peaks in each plot represent the shedding and turbine frequency, respectively.

2.4 Turbine-Turbine and Hill-Turbine results and discussion

Two benchmark experiments were conducted to study the turbine output and, thus, the turbine's response to complex incoming flow conditions. The first case consisted of two streamwise aligned turbines (referred to as turbine-turbine interaction) separated by six rotor diameters ($6D$), immersed in the TBL. The second test case introduced complex topography by using a model hill placed $6D$ upstream of the test turbine (referred to

Table 2.6: Comparison of voltage statistics at different locations in the cylinder wake for the cases illustrated in Figure 2.7.

x/d_c	$V[V]$	$\sigma_v[V]$	I_v
2	0.36	0.026	0.073
4	0.42	0.026	0.061
6	0.47	0.026	0.056
No Cyl.	0.52	0.027	0.052

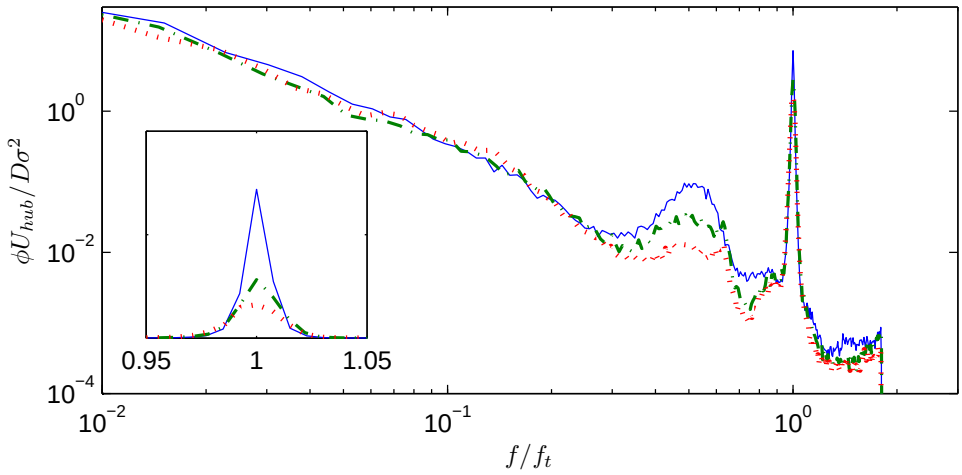

Figure 2.7: Comparison of voltage spectra between various spacing of the cylinder and turbine (cylinder $d_c = 0.034\ m$ upwind of the turbine). $2d_c$ upwind is denoted by the blue solid line, $4d_c$ by the green dash-dot line and $6d_c$ by the red dotted line. The subplot highlights spreading and magnitude change near the turbine frequency (f_t). The upwind hub velocity was 7 $m\ s^{-1}$ and measurements were taken in the TBL.

as hill-turbine interaction). Each case is then compared with a single turbine placed in the TBL with no upstream perturbation (referenced as the baseline case). A schematic of the two cases in question is shown in Figure 2.3a.

Figure 2.8 displays velocity profiles and turbulence intensities for the baseline flow, $6D$ downwind of the hill and of a turbine. The velocity profiles in Figure 2.8(a) illustrate the velocity deficit induced by both the hill (□) and the turbine (x). The shear layer between the wake and the incoming TBL flow for the turbine example is marked by an increase in root mean square (r.m.s.) velocity near the top tip height ($z/z_{hub} \approx 1.5$). The turbulence introduced in the hill case (setup pictured on right side of Figure 2.3), which is largely initiated by the peak of the hill, is clearly shown in Figure 2.8(b) as the increase in turbulence intensity from the surface up to $z/z_{hub} = 1$.

Figure 2.9 describes the spectra of the flow $6D$ downwind of the hill at various heights (green lines). Also, the vertical sweep from the baseflow case (shown in thick, red lines) is

Table 2.7: A comparison between both tachometer and voltage under different incoming flow conditions. Measurements were taken at $U_{hub} = 7\ m\ s^{-1}$ in all the cases. Two cylinders were used with diameters of 0.034 and 0.042 m. The predicted values for the shedding frequency (f_s) come from Equation 2.1, while the validated estimate of turbine frequency (f_t) is the mean rotational speed calculated from the tachometer signal. The measured values of f_t and f_s are found by inspecting the spectra from the respective time signals.

Cylinder	Type	Measured f_t [Hz]	Validated f_t [Hz]	Measured f_s [Hz]	Predicted f_s [Hz]
1	Ω_{tach}	60.0	63.6	38.5	41.1
	$V_{turbine}$	60.4	-	38.7	41.1
2	Ω_{tach}	53.0	56.5	29.0	32.8
	$V_{turbine}$	53.6	-	27.0	32.8

considered for comparison. The spectra of the streamwise velocity components indicate an increase in turbulent kinetic energy in the low frequency range, providing the insight that the hill generates a wide range of scales. The largest increase in low frequencies occurs just above $z/z_{hub} = 1$, which corresponds to the hill's height. The velocity spectra at each measurement elevation show an increase in energy in the high-frequency range, while nearing $z/z_{hub} = 1.6$ (rotor top tip location) a decrease of energy in the low frequency range occurs. It is inferred that the developing shear layer, around the rotor and including the tip vortices ($z/z_{hub} \approx 1.5$), is responsible for enhanced turbulence at scales smaller than the rotor, as compared to the baseflow case.

Moving to the turbine wake flow, it should be noted that even if the wind turbine were to be harvesting more power (i.e. running at a lower tip-speed ratio) the changes in velocity deficit and fluctuations (shown in Figure 2.8) would be minimal at $6D$ downwind. Hu et al. (2012) [16] found that changing the tip-speed ratio did affect the wake characteristics, however the largest deficit was only 0.25 $m\ s^{-1}$at $x/D = 0.5$ with a tip-speed ratio reduction of 1.5. In addition to this small deficit in the very near wake, the increased turbulent kinetic energy brings more energy into the wake, further reducing the deficit as the flow progresses downwind. Figure 2.10 delineates the streamwise velocity spectra taken $6D$ downwind of a turbine (shown in blue). These represent the scale-by-scale energetic content of the incoming flow for the downwind turbine in the

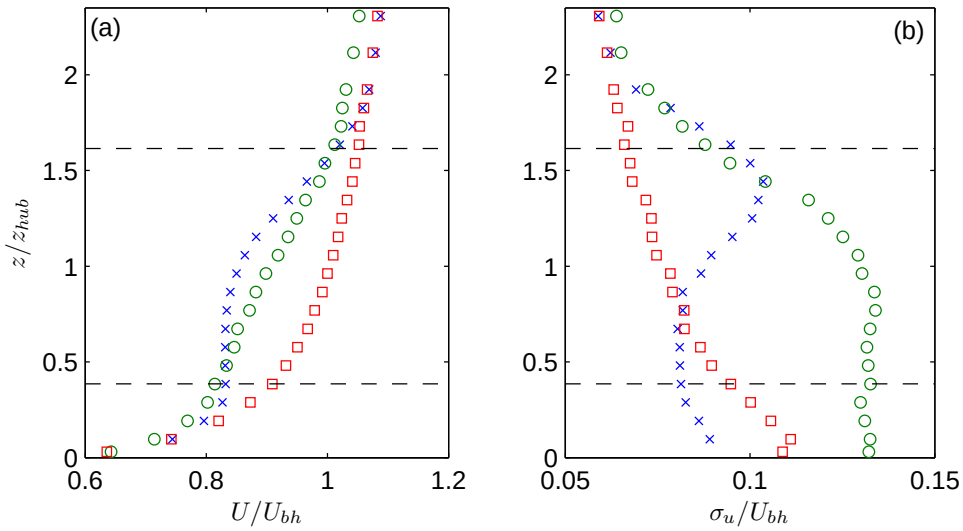

Figure 2.8: Incoming flow statistics: (a) vertical profiles of the mean velocity; (b) r.m.s. streamwise velocity component, all normalized by the mean hub velocity for the baseflow case U_{bh}. The red □ represents the baseflow (incoming flow for the single turbine case), the green ∘, $6D$ downwind of the hill (incoming flow for the hill-turbine case), and the blue x, $6D$ downwind of a turbine (incoming flow for the turbine-turbine case). Measurements taken in the TBL at $U_{hub} = 7\ m\ s^{-1}$. The black, horizontal, dashed lines give the location of the top and bottom tip of the rotor.

turbine-turbine case. As observed by Chamorro et al. (2012) [31], the spectra exhibit a decrease in the low frequency range and an increase in the high-frequency range from the bottom tip ($z/z_{hub} \approx 0.4$) to very near the top tip ($z/z_{hub} \approx 1.6$), as compared to the baseflow case. The energetic increase in the intermediate to high-frequency range is not as relevant as in the hill case, but strongly depends on the vertical position. In particular, near the top tip of the rotor, at $z/z_{hub} = 1.5$, a strong energetic contribution is observed in the low frequency range that is believed to be related to the incoming large scale structures developing over the unperturbed boundary layer, traveling above and around the turbine, and then being entrained and interacting with the turbine wake and rotor tip vortices.

The turbine is observed to attenuate the incoming large scales close to the wall,

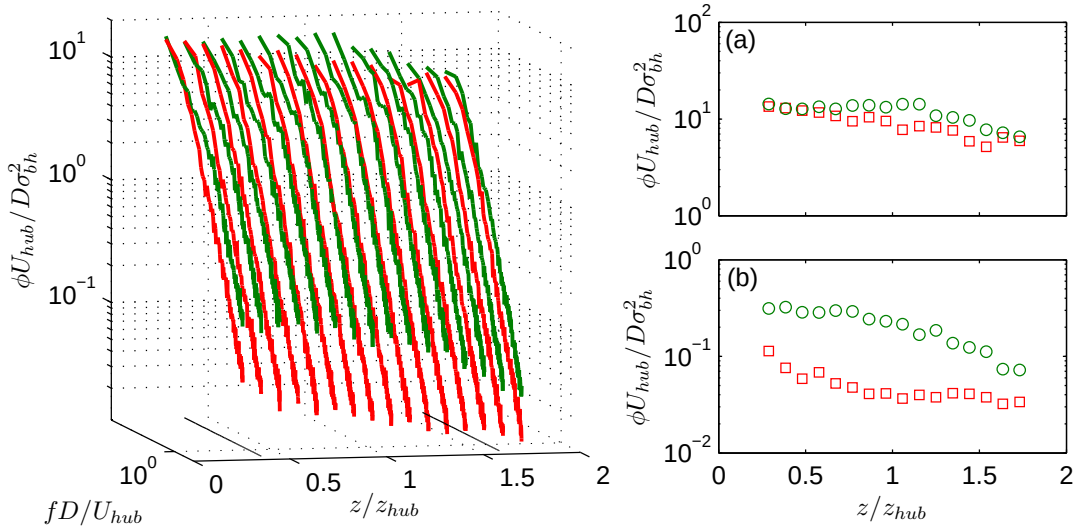

Figure 2.9: Hill-baseflow spectra comparison of the streamwise velocity components obtained in the baseflow (red) and in the flow behind the hill (green) at different heights. For the latter case, cross-wire measurements were obtained $6D$ downwind of the hill. The spectrum is normalized by U_{hub}, D and σ_{bh}^2, where σ_{bh}^2 is the integral of the frequency spectrum of the baseline case at hub height. Solid black lines indicate the rotor bottom tip ($z/z_{hub} \approx 0.4$) and top tip ($z/z_{hub} \approx 1.6$). Panels (a), (b) present slices of the spectra at $fD/U_{hub} \approx 0.02$ and 1.4, respectively. The red $\square$ represents the baseflow (incoming flow for the single turbine case) and the green $\circ$, $6D$ downwind of the hill (incoming flow for the hill-turbine case). Measurements were taken in the TBL at $U_{hub} = 7\ m\ s^{-1}$.

exerting a confinement effect between the bottom rotor tip and the wall, thereby producing a local flow acceleration, as shown in Figure 2.8a. The increased local mean shear, combined with the progressive interaction between the turbine wake and the local wall turbulence may explain the slight increase of turbulent kinetic energy in the high-frequency range flow near the wall. Flow measurements at $4D$ in the wake of the turbine show a larger turbulent kinetic energy increase in this high frequency range, which demonstrates that the interaction between the turbine near wake shear layer and the surface shear layer is stronger closer to the turbine. As z/z_{hub} increases well above 1.5, the velocity spectra in the turbine wake tend to approach those from the baseflow

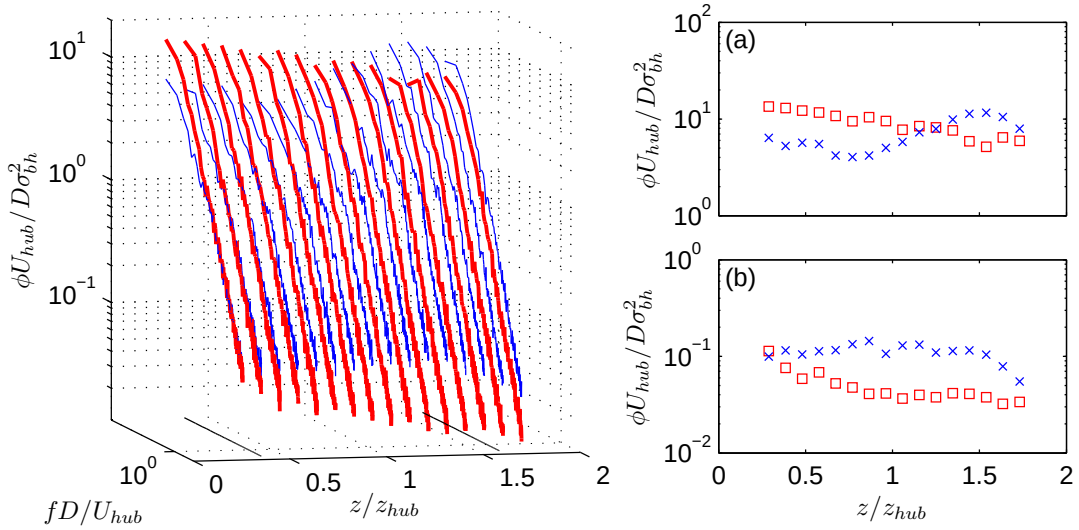

Figure 2.10: Turbine-baseflow spectra comparison of the streamwise velocity components obtained in the baseflow (red) and flow behind a turbine (blue) at different heights. The cross-wire profile was taken $6D$ downwind of the turbine. The spectrum is normalized by U_{hub}, D and σ_{bh}^2, where σ_{bh}^2 is the integral of the frequency spectrum of the baseline case at hub height. Solid black lines indicate the rotor bottom tip ($z/z_{hub} \approx 0.4$) and top tip ($z/z_{hub} \approx 1.6$). Panels (a), (b) present slices of the spectra at $fD/U_{hub} \approx 0.02$ and 1.4, respectively. The red $\square$ represents the baseflow (incoming flow for the single turbine case) and the blue x, $6D$ downwind of a turbine (incoming flow for the turbine-turbine case). Measurements were taken in the TBL at $U_{hub} = 7\ m\ s^{-1}$.

case.

To provide a direct comparison between the flow past the hill and flow past a turbine, Figure 2.11 shows the two streamwise velocity spectra together. The energetic content of the flow past the hill manifests an increase in the streamwise turbulent kinetic energy in the low frequency range, occurring between bottom tip and top tip. The maximum difference is observed at hub height, as compared to the flow downwind of a turbine.

Interpreting the turbine voltage signals provided the insight needed to understand how the turbine responds to the differences in inflow. Figure 2.12 shows a sample of filtered turbine voltage for the single turbine case. The very small fluctuations in the signal are at the turbine frequency. The signal exhibits fluctuations in time-scales

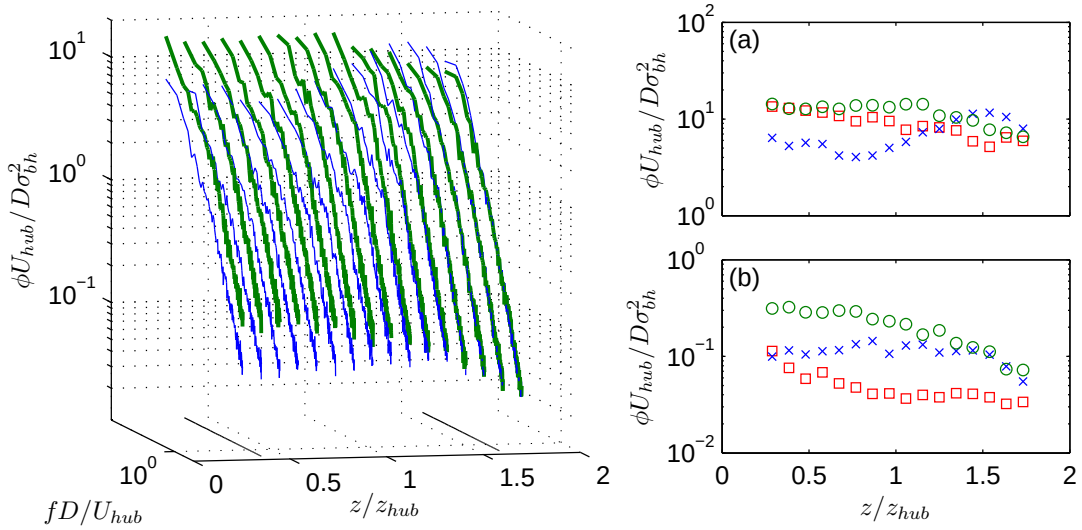

Figure 2.11: Hill and turbine spectra comparison of the streamwise velocity components obtained in a turbulent flow $6D$ behind the turbine (blue) and $6D$ behind the hill (green). The spectrum is normalized by U_{hub}, D and σ_{bh}^2, where σ_{bh}^2 is the integral of the frequency spectrum of the baseline case at hub height. Solid black lines indicate the rotor bottom tip ($z/z_{hub} \approx 0.4$) and top tip ($z/z_{hub} \approx 1.6$). Panels (a), (b) present slices of the spectra at $fD/U_{hub} \approx 0.02$ and 1.4, respectively. The red $\square$ represents the baseflow (incoming flow for the single turbine case), the green $\circ$, $6D$ downwind of the hill (incoming flow for the hill-turbine case), and the blue x, $6D$ downwind of a turbine (incoming flow for the turbine-turbine case). Measurements were taken in the TBL at $U_{hub} = 7\ m\ s^{-1}$.

ranging from a fraction to several seconds. These fluctuating features are similar to those found in the time signals for both the turbine-turbine and hill-turbine cases. As shown in Table 2.8, the test turbine (downwind turbine) has a reduced mean voltage output for both cases. The fluctuations, on the other hand, are reduced for the test turbine in the turbine-turbine case while increased in the hill-turbine case. The spectra of the turbine voltage signal were computed to further quantify the turbine response.

The voltage spectra from the reference turbine in the two benchmark and baseline case studies, shown in Figure 2.13, can be interpreted using the knowledge gleaned from the cylinder study experiments on the velocity spectra of the respective incoming

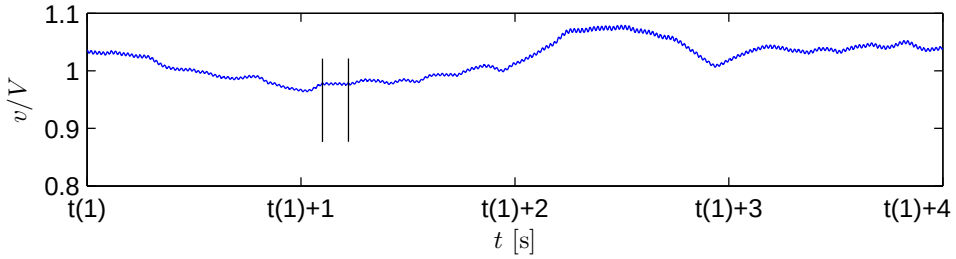

Figure 2.12: Sample of the low-pass filtered turbine voltage signal in time (single turbine in the TBL). The voltage is normalized by its mean. The two vertical lines just after t(1)+1 indicate the average time required for two rotor revolutions or six full blade passes, as shown by small peaks in signal.

Table 2.8: Comparison between the mean and r.m.s. voltages in the two case studies. V_{ref} and $\sigma_{v_{ref}}$ indicate the mean and r.m.s. voltages of the single turbine reference case, respectively

	Turbine-Turbine [%]	Hill-Turbine [%]
V/V_{ref}	75.7	87.0
$\sigma_v/\sigma_{v_{ref}}$	70.0	107.5

flows. The turbine frequency stands out as the dominant peak in the voltage spectra for all three cases, due to generator construction; however, the voltage spectra for the turbine-turbine case shows an increased energetic content in the frequency range below the turbine frequency ($0.15 < f/f_t < 0.7$) while the hill-turbine case has increased energy in an even larger range ($0.02 < f/f_t < 0.7$), with respect to the single turbine case. The effect of the hill on the turbine voltage (in particular on the fluctuating component) is expected to be similar to the one exerted by the vertical cylinder, as with bluff body shedding vortices, but disparate to a turbine extracting energy from the flow. Specifically, Figure 2.13 shows the turbine voltage reacting to the hill-induced large scale perturbations at $f/f_t \approx 0.15$, thus equating to scales roughly six times larger than the rotor diameter. This means that the larger turbulent scales developed within the incoming boundary layer and those generated by the hill are felt by the turbine and resolved in the voltage signal.

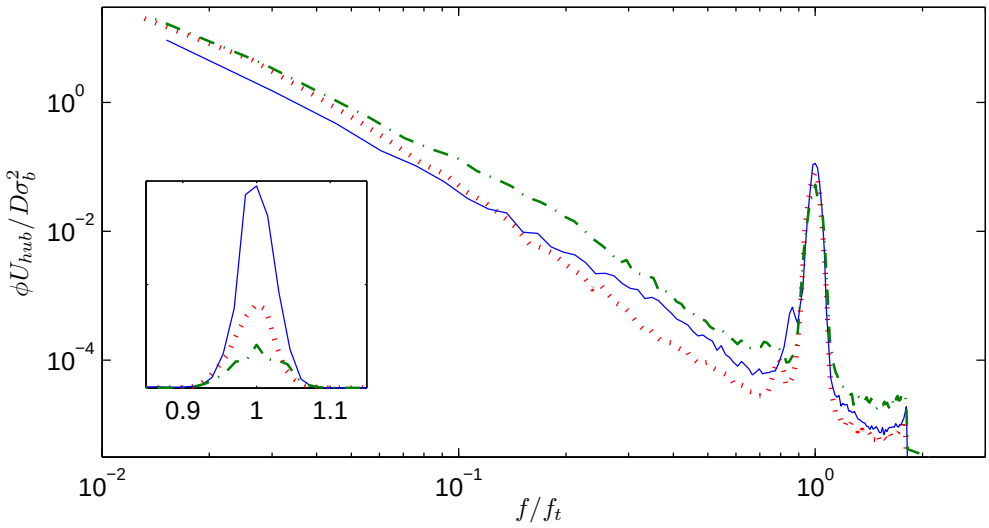

Figure 2.13: Spectral comparison between the single turbine (baseline), turbine-turbine and hill-turbine cases for the downwind turbine. All the cases were performed in the TBL with tunnel speed constant hub velocity of 7 $m\ s^{-1}$. Red dotted, blue solid, and green dash-dotted lines represent the single turbine, turbine-turbine, and hill-turbine cases, respectively.

For the turbine-turbine interaction case, the front turbine introduces turbulent kinetic energy mostly in the range of intermediate and high frequencies, $f/f_t > 0.2$. The resulting upwind turbine wake can either act constructively or destructively on the amplitude of the turbine frequency of the trailing turbine, as both turbines have a similar turbine frequency ($f_t = 77$ [Hz] and $f_t = 67$ [Hz], for the upwind and downwind turbines, respectively). The turbine-turbine case spectrum, shown in Figure 2.13, displays an amplified turbine frequency in comparison with the baseflow case, suggesting a constructive interaction. According to those results, the front turbine exerts a stabilizing contribution to the rotor angular velocity of the downwind turbine, which is consistent with the lower r.m.s. voltage reported in Table 2.8. However, note that the mean voltage output for the downwind turbine is lower as compared to the upwind turbine.

The auto- and cross-correlation functions of the turbine voltage time signals are used to further examine the downwind turbine response in the case of turbine-turbine

interaction. The auto-correlation for the upwind (UW) ρ_{UW} and downwind (DW) ρ_{DW} turbines can be found in Figure 2.14(a). The voltage correlation function is defined in the following equation:

$$\rho_{xy}(\tau) \equiv \frac{\overline{v_x(t)v_y(t+\tau)}}{\sqrt{(\overline{v_x^2})(\overline{v_y^2})}}; \tag{2.2}$$

where ρ_{xy} is the correlation between instantaneous voltage signals v_x and v_y, t is the time and τ is a time lag (x and y signify generic turbine voltage signals). The temporal voltage auto-correlation is calculated using Equation 2.2 by placing a single voltage signal into both v_x and v_y (i.e. $v_x = v_y = v_{UW}$). As seen in the figure, the DW turbine has increased auto-correlation through the range of lags $0.1 < \tau < 1$ when compared to the UW turbine. This trend was counter intuitive, when compared to the auto-correlation of a cross-wire signal, and thus drove the decision to assess the cross-correlation, which is also shown in Figure 2.14(a). The cross-correlation ρ_{DU} is found to reach a maximum of $\rho_{DU} = 0.85$ on a well defined peak located at $\tau \approx 0.18$ s. The high correlation and specific peak location of the cross-correlation show that the DW turbine, after a specific time lag, responds to flow structures energetically similar (though attenuated, recalling the normalization by the local voltage variance) to those impacting the UW turbine. While the UW turbine has an effect on the amplitude of the DW turbine frequency, due to similar turbine frequencies and subsequent tip vortex spacing, the overall impact of the UW turbine on the DW turbine's variation in voltage may originate from a few different physical mechanisms: (i) the signature of the incoming flow remaining in the wake; (ii) the spatially persistent effect of the tip vortices in the wake;(iii) the effect of large scale structures deflected by the UW turbine and entrained back into the wake; (iv) the effect of wake meandering, amplifying the variability of the incoming flow. The consistent long tails in the voltage auto-correlation suggest that the largest scales of the incoming flow play a key role in the UW turbine far wake. On the other hand, as demonstrated by Chamorro et al. 2012 [31], the signature of the large scale structures is drastically reduced in the near wake, where the tip vortices prevail. This implies that the large scale flow structures impacting the UW turbine voltage output are not likely to survive in the near-far wake transition but rather are deflected and entrained

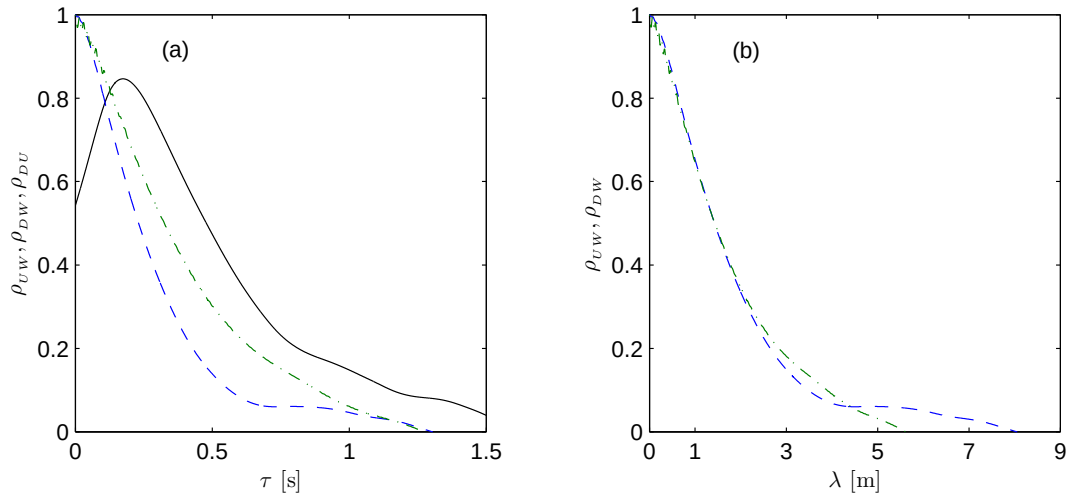

Figure 2.14: (a) Temporal auto-correlation of v_{UW} (ρ_{UW} - dash) and v_{DW} (ρ_{DW} - dash-dot) turbine and cross-correlation of v_{DW} to v_{UW} (ρ_{DU} - solid line). (b) Spatial auto-correlation for the UW and DW turbine calculated using their respective convection velocity, $\lambda = \tau u_c$.

or allowed to induce large scale variability in the wake, ultimately influencing the DW turbine.

The cross-correlation peak location coupled with Taylor's assumption of frozen turbulence, allowed the time lags τ to be converted to length scales λ using an adequate convection velocity U_c for each turbine. U_c is defined as the velocity at which the majority of the scales are convected downwind. The UW turbine convection velocity $U_{c_{UW}}$ is computed from the linear trend between the mean turbine voltage and flow velocity (see Figure 2.4) and was found to be $U_{c_{UW}} = 7.0\ m\ s^{-1}$. U_c for the DW turbine ($U_{c_{DW}}$) is calculated by dividing the distance separating the turbines (6D in this case) by the lag time τ where the peak in the cross-correlation curve occurs ($\tau \approx 0.18$ s) which gives a value of $U_{c_{DW}} = 6.2\ m\ s^{-1}$. Note that the difference in convection velocity has an impact on the integral time-scale due to the differing time that structures have to advect and interact with each turbine; this alludes to the reason why the temporal auto-correlation for the DW turbine increases, as compared to the UW turbine, for a wide range of time lags τ. The spatial auto-correlation functions are plotted against the length scales λ in Figure 2.14(b).

In Figure 2.14(b) the UW and DW turbine voltages exhibit similar spatial auto-correlation in the range $0.3 < \rho(\lambda) < 0.9$. For $\rho > 0.8$ (thus for $\lambda < 6D$) the DW turbine voltage, as opposed to the UW signal, exhibits a weakly oscillatory auto-correlation due to the more pronounced turbine frequency (as shown in the voltage spectra in Figure 2.13). Below $\rho \approx 0.3$, corresponding to length scales λ up 2 m (approximately 3δ), the DW signal starts to be influenced by larger structures than the UW. At $\rho = 0.2$, again with $U_{c_{UW}} = 7.0$ and $U_{c_{DW}} = 6.2$ $m\ s^{-1}$, the difference in length scales λ felt by the turbines is approximately 0.2 m. This length difference may be due to the stretching of the flow structure as it travels around the UW turbine. Below $\rho = 0.1$ the UW turbine appears to react to scales larger than 7δ, classified as very large scale motions (Balakumar and Adrian 2007 [32], Guala et al. 2011 [26]), which do not appear in the DW turbine signal. Those large scale structures are inferred to be formed by spanwise alignment of δ scale (or ramp like) structures (Adrian et al. 2007 [33]), which would break up if a portion of them was entrained in the UW turbine wake. The recognition of these very large scales of motion by the turbine is notable but we acknowledge that the correlation function may not be well converged or reliable for values below 0.1; therefore, the precise length cannot be accurately quantified. Indeed, while velocity scales of 6 to 10 δ are realistic in turbulent boundary layers, as confirmed by the auto-correlation of the streamwise velocity (observed energetically relevant length scales up to 3 m), a scale of 8 m as compared to an available fetch of 13 m appears overestimated.

Given the information presented in the correlation figures, a description of the flow between the turbines can now be provided. The first point noted above from the voltage auto-correlation is that of the increased integral scale for the DW turbine. The auto-correlation plotted versus length scale λ, assuming Taylor's hypothesis of frozen turbulence, reveals, however, that both turbines see roughly the same size of energetic scales. Pair this fact with the high cross-correlation value and it can be considered that the length scales which interact with the UW turbine also have an impact on the DW turbine. Previous research (Chamorro et al. 2011 [17], 2012 [31]) has shown that length scales larger than the rotor which directly hit the turbine are heavily truncated. Herein, it is suggested that those large turbulent length scales which do not directly strike the turbine are not entirely destroyed but are rather displaced and redirected by the UW turbine's rotor stagnation zone, allowing re-entrainment into the turbine wake,

and eventually affecting the DW turbine.

Recall that the turbine voltage spectra showed that the largest scales in the flow have the greatest impact on the rotor fluctuations because the turbine can only respond to the scales which are energetic enough to influence the rotational inertia of the rotor. The large, energetic scales which collide with the UW turbine (which experiences high fluctuations) are reduced in strength as a result of some energy having been transferred from the flow structures into voltage production. As the large scale structures continue downwind, they are coerced into interacting with the turbine wake and shear layer which further reduces their vivacity before they encounter the DW turbine. The DW turbine voltage signal is thereby influenced by the incoming turbulent length scales (shown in the Figure 2.14) with reduced intensity (reduced fluctuations as shown in Table 2.8). This argument can explain the reduced voltage fluctuations and the high cross-correlation.

With the current data, it is acknowledged that the energetic contribution of large scale structures that are deflected and entrained back can not be distinguished from those that pass through the rotor. However, near wake measurements in [31] indicate that the large scales (scales greater than the rotor diameter) are not present in the near wake. Therefore it is suggested here that the large scale impacting the turbine rotor may have a spanwise extent larger than the rotor itself, implying that a portion of them is destroyed by the rotor, another fragment is deflected and then entrained in the wake to impact the downwind turbine and the remaining is just advected without affecting either turbine. PIV measurements in the wall parallel plane will be employed to quantify these contributions.

2.5 Summary

A series of validation tests were successfully performed in the SAFL wind tunnel to relate (i) the mean hub velocity to the mean voltage output of a miniature wind turbine, (ii) the fluctuations of the rotor angular velocity to voltage fluctuations, and (iii) the mean rotor angular velocity with a specific peak in the voltage spectra. In addition, the turbine voltage spectrum was found to correctly estimate not only the turbine frequency but also the signature of incoming, coherent, large scale turbulent flow structures, such as, in a particular test case, von Kármán vortices shed from vertically oriented cylinders

upwind of the turbine.

Two benchmark cases relevant to the study of turbine layout in a wind power plant in complex terrain (turbine-turbine and hill-turbine interactions) were then conducted. Cross-wire velocity measurements behind a turbine and a sinusoidal hill, along with the downwind turbine voltage (used to study the turbine response in terms of mean and fluctuating rotor angular velocity), revealed that the turbine perceived the different incoming flow conditions. Results showed that an upwind turbine reduced both the mean voltage by 25% and the impact that the large scale structures have on the downwind turbine, thus causing a 30% reduction in the downwind voltage r.m.s. An upwind hill, while decreasing the mean voltage by 13%, introduced large flow scales, causing a 7% increase in the downwind turbine voltage r.m.s.

The inspection of the correlation functions in the turbine-turbine case corroborated the finding that the upwind turbine lessened the impact that the high energy, large flow structures have on the downwind turbine. The cross-correlation shows that, while the upwind turbine takes the brunt of the incoming turbulent fluctuations, the upwind turbine does not entirely remove the energetic scales from the flow but it is inferred from our results to deflect a portion of them and then entrains them back in the wake, possibly destabilizing the wake itself. The voltage signals from the upwind and downwind turbines exhibit a high cross-correlation value. In addition, when the temporal auto-correlations of the turbine voltages are plotted as a function of a spatial lag using Taylor's hypothesis, both turbines are found to interact with flow structures of similar size distribution. Both observations suggest the dominant effect on the rotor kinematics is exerted by the large scale flow structures of the incoming turbulent boundary layer.

We suggest that optimal turbine siting under various complex inflow conditions can indeed be determined as a first approximation through the voltage signal, which provides a measure of the steady and unsteady kinematic response of the rotor. Further, analysis of the correlation functions from many turbine voltages will bestow a great understanding as to the scale-by-scale energetic content of the turbulent flow perceived by the turbines and responsible for their unsteady loads.

Chapter 3

On the Response of a Wind Turbine Model to Atmospheric and Terrain Effects

Utilizing the research and findings presented in Chapter 2 about the model wind turbine, the current chapter delves into investigating the complexities of turbine operation introduced by changing atmospheric stability and the surrounding terrain. A series of experiments were conducted in a boundary layer wind tunnel in which the model wind turbine was exposed to three thermally different boundary layer flows and three simple arrangements relevant to wind farm applications (single turbine in boundary layer, turbine-turbine aligned, and a three-dimensional hill aligned upwind of the turbine). The response of the turbine to the various inflow conditions was investigated through detailed inspection of the voltage produced by the model turbine's DC generator. Particle image velocimetry was utilized to provide a description of the flow upwind and downwind of the turbine rotor for neutral, weakly stable and weakly convective thermal stratifications, while a Pitot-tube and thermocouple were used to determine the mean flow boundary conditions (mean velocity and temperature profiles of the incoming flow). The voltage signal was used to track, simultaneously, the response of the turbine to changes in the mean flow (from mean voltage) and to large turbulent flow structures that impinge upon the turbine rotor (captured in voltage fluctuations).

The two-point streamwise velocity correlation map revealed that large scale motions in the hill wake were attenuated under stable temperature conditions. The premultiplied voltage spectra further confirmed a non-trivial link between thermal stratification and terrain complexity, revealed in the size and intensity of the energy containing flow structures impacting the rotor.

Submitted in current form to *Boundary-Layer Meteorology*, June 2014.

3.1 Introduction

Wind energy is rising in importance not only as a renewable energy source, but also as a major component of energy production for many nations around the world. However, even as governments are pushing for higher power production from the wind, there are still many complex problems surrounding wind energy that are not well grasped. The areas in need of further research include gearbox design, power transmission from source to end user, atmospheric turbulence influence on turbine and wind turbine control (to increase efficiency and reduce structural fatigue), to name a few. Herein we will focus on the fluid mechanic aspects of wind power production, particularly boundary layer flows and the complexities introduced by thermal and topographic boundary conditions. Early experiments in this area dealt with describing and understanding both local blade aerodynamics for optimal energy capture and the associated complex wake flow produced by wind turbines (Buck and Renne 1985 [5], Vermeer et al. 2003 [34] and Sørensen 2011 [35], Gonzales-Longatt et al 2012 [21], Husien et al 2012 [22], Meneveau 2012 [23]). While the assumption of a vertically uniform velocity over the entire rotor (i.e. no wind shear) reduces the problem's complexity, it introduces a disconnect from turbines operating in a boundary layer, requiring further investigations to study wind turbine performance and wake evolution within a turbulent boundary layer flow (Chamorro and Porte-Agel 2009 [20], Cal et al 2010 [24], Lebron et al 2012 [25], Hu et at 2012 [16], Howard et al. 2013 [1], among others).

All of the current utility-scale wind turbines operate in the lower portion of the atmospheric boundary layer (ABL), with the exception of the recently reinvigorated blimp lifted, high-altitude wind turbines, and are thus subject to high shear and turbulence levels that accompany near surface flow, including large scale motions [32] generated by

terrain inhomogeneity and Chamorro and Arndt [7] show that including shear across the rotor impacts the theoretical Betz's limit. A large majority of the previous research combining wind turbines and the ABL have investigated turbine wake flows with little emphasis on the variability of the inflow conditions. Again, Vermeer et al. (2003) [34] provides a thorough list of wind tunnel studies related to the aerodynamics of wind turbines and Sørensen (2011) [35] discusses and lists a wide range of topics (i.e. blade element theory, wind capture performance, and various equations to predict power coefficients) while referring to previous research for the given areas. Further research has been conducted to describe how the flow within and above a wind farm develops and interacts with the individual turbines using both experimental (e.g. Frandsen 1992 [36], Corten et al. 2004 [37], Cal et al. 2010 [24], Chamorro and Porté-Agel [38]) and computational methods, e.g. Ivanova and Nadyozhina 2000 [39], Calaf et al. 2010 [40], Porté-Agel et al. 2011 [41], Yang et al. 2012 [12].

The majority of the research involving the ABL and wind turbines has been performed in neutrally stratified conditions. However, as shown by Stull (1988) [42], during an average day (twenty-four hour period) the ABL shifts between a convective boundary layer (positive, vertical buoyancy produced by daytime heating of the earth's surface) and a stable, or nocturnal, boundary layer (thermal striation caused by surface cooling). Therefore, the neutral boundary layer only occurs during the short transition between the other two states, and subsequently, wind turbines operate primarily in non-neutral stratification. In the atmosphere, temperature, wind and other conditions (pressure, relative humidity, etc.) are continuously changing throughout the day, thus varying the buoyancy effects on boundary layer structures, including the large and very large motions affecting turbine performance [1]. Wind energy research conducted in the stable ([20]) and convective boundary layers ([43]) in the St. Anthony Falls Laboratory (SAFL) wind tunnel encompass single turbine wake studies and full wind farm analyses. Along with changes in thermal stability, simple topographic perturbations alter both the mean velocity distribution in the ABL and the intensity of the large scale coherent motions controlling the unsteadiness of wind turbine performance (e.g. fluctuations in rotor angular velocity, and subsequently, torque and power).

Much research has been conducted examining the surface roughness and its impact

on boundary layer flow (Brunet et al. 1994 [44], Ishihara et al. [45], Chamorro and Porté-Agel [19], among others). Some early experiments studied the effect of different terrain on the turbulent quantities (Finnigan et al. 1990 [46]), while others inspected subsequent relation of turbulence to particle dispersion (Castro and Snyder 1982 [47], Arya and Gadiyaram 1986 [48], Snyder and Britter 1987 [49]). Snyder and Britter inspected the influence of different two-dimensional, triangular shaped hills as well as a bell-shaped, three-dimensional hill on particle concentration. To further move toward the ABL, both surface roughness and topography were introduced together and examined in Ch. 1 of the book Wind and Trees (Ch 1, pp 3-40 Finnigan & Brunet [50]). Others also investigated the effect of hills (Carpenter and Locke 1999 [51], Kanda et al. 2013 [52]) and roughness over different shaped hills (Ayotte and Hughes 2003 [53], Harman and Finnigan 2013 [54]). Neff and Meroney [55] produced results pertaining to flow over hills with vegetation and the wind power available for wind turbines. Including atmospheric conditions in addition to complex topography allows for an even better representation of the ABL (Takahashi et al. 2005 [56], Howard et al. 2013 [1]).

Topography effects on power production in wind farms and wake flow patterns have been addressed by Politis et al 2012 [14], Gravdahl and Rorgemoen 2002 [15], Yang et al 2012 [10], and recently by Howard et al. [1] for a sinusoidal hill. A hill is a simple case of terrain inhomogeneity that alters the large scales of the incoming turbulence (Tampieri et al 2003 [18]) and sheds large scale vortices (as compared to the rotor diameter) able to leave a signature on the instantaneous power or rotor angular velocity [1].

The effect of terrain complexity on the large scale structures of the ABL, however, strongly depends on the local thermal stability regime, shown particularly well by the ability of topographic perturbations to induce large scale instabilities (Kelvin-Helmholtz and internal waves) in strongly stratified flows. Such phenomena are common in the atmospheric surface layer at night and are not well parameterized by micro-meteorological models ([57]), thus requiring further investigation. Even though strongly stratified conditions could not be reproduced in our wind tunnel, we observed that combining thermal and topographic variability of the inflow conditions had a strong and non-intuitive signature in the voltage produced by the model-turbine in the testing and discussion presented in Howard et al. [1]. We therefore decided to (i) maintain the sinusoidal hill as the simplest finite three-dimensional perturbation, scaling with the turbine hub

height, (ii) combine turbine voltage measurements with detailed flow field measurements through PIV, and (iii) expand the range of data pertinent to thermal influences on turbine operation.

It is the goal of this work to study how changes in atmospheric stability coupled with complex terrain features, in a controlled experimental setup, impact wind turbine performance and operation. In particular, we focus on how the different boundary conditions alter the large scale motions of the turbulent boundary layer which consistently leave their signature on both spatial flow statistics and turbine voltage statistics. While we must acknowledge that topographic effects are marginally investigated, we stress that under varying stability regimes even a simple hill had major implications on the turbine performance. We reiterate herein the concept that combined flow and turbine data are needed to understand (i) how optimal turbine siting in a wind farm can be attempted based on the planimetric distribution of topographic features and (ii) how turbine unsteady production can be used as a measure of the large scale variability of the incoming flow for multi-turbine power plant control. The remainder of this document covers the experimental setup in Section 3.2, PIV and voltage output results in Section 3.3 and summary and conclusions in Section 3.4.

3.2 Experimental Setup

The experiments were conducted in a closed loop wind-tunnel with a 200 horse-power fan at St. Anthony Falls Laboratory (SAFL) on the campus of the University of Minnesota. The test section has a cross-section of 1.7 m by 1.7 m and a length of 16 m, a portion of the full tunnel fetch of 37.5 m. The flow is conditioned by coarse wire mesh and a honeycomb flow straightener before entering a 6.6:1 aspect ratio contraction located just upwind of the main test section. A 0.040 m picket fence trip produced a turbulent boundary layer with flow that is characterized by a well-developed surface layer with a constant shear stress and logarithmic velocity profile. The ceiling panels were adjusted to provide zero pressure gradient through the length of the test section. The boundary layer was developed over a smooth floor surface made up of aluminum plates with streamwise lengths of 0.3 m. Each of the panels can be heated or cooled to produce the desired thermal stratification. The air temperature is controlled by a large heat

Table 3.1: Characteristics of the thermal boundary layers. T_s and T_δ are the temperatures for the floor surface and freestream flow, respectively. U_{hub} and u_* are the hub and shear velocities, while Θ is the momentum thickness. $Re_\Theta = U_\infty \Theta/\nu$, $Re_\delta = U_\delta \delta/\nu$ and Ri_B is the bulk Richardson number

Stability	T_s [° C]	T_δ [° C]	U_{hub} [ms^{-1}]	u_* [ms^{-1}]	Θ [m]	δ [m]	Re_Θ [-]	Re_δ [-]	Ri_B [-]
Neutral	14.0	14.0	2.31	0.113	0.039	0.58	6930	4148	0
Stable	14.0	55.0	2.52	0.104	0.044	0.60	8678	4078	0.09
Convective	74.0	12.0	2.40	0.115	0.016	0.40	2177	2570	-0.11

exchanger located just past the drive fan diffuser. Herein, the three thermal settings held the floor and freestream air temperatures independent. The thermal system of the wind tunnel has the ability to hold the temperature to within ± 0.2°C.

Three thermal stability conditions (neutral, stable and convective stratifications) were tested to inspect their influence on the wind turbine performance. The specific set points for the different boundary layers are shown in Table 3.1. The boundary layer thickness $\delta = z(0.99U_\infty)$ was located with measurements from a Pitot-static tube profile for each stability condition, while the thermal boundary layer height δ_T, determined from thermocouple measurements, was found to be consistent with δ. The standard assessment of the thermal conditions in the atmospheric surface layer is provided by z/L, where z is the vertical distance and L the Obukhov length defined as $L = -u_*^3 T_v / \left(\kappa g (\overline{w\prime T\prime_v})_s\right)$, where u_* is the shear velocity, T_v is the average virtual potential temperature, κ is the von Kármán constant, g is the gravitational constant and $(\overline{w\prime T\prime_v})_s$ is the virtual potential temperature flux at the surface. The Obukhov length is interpreted as the height at which the turbulent kinetic energy (TKE) produced by buoyancy is equal to that produced by shear. However, to calculate L, a direct estimate of the vertical heat flux is needed, requiring simultaneous high frequency measurements of air temperature and velocity, which were not available during our PIV experiments. In our current setup we estimated the bulk Richardson number, defined as $Ri_B = g\delta\Delta T_s / \left(T U_\infty^2\right)$; where ΔT_s is the temperature difference between T_∞, the free stream air at $z \simeq \delta$, and the tunnel floor surface T_s, T is the average temperature and U_∞ is the freestream velocity of the boundary layer. Ri_B provides a bulk indication of the buoyancy effect with respect to the wind shear.

The three cases selected to investigate turbine response were (i) a single turbine in the turbulent boundary layer (referred to as single turbine or ST hereafter), (ii) a turbine placed six rotor diameters (D) upwind of the test turbine (turbine-turbine or TT hereafter) and (iii) a three-dimensional sinusoidal hill $6D$ upwind of the test turbine (hill-turbine or HT hereafter). The spacing distance of $6D$ was chosen as it is a representative spacing used in current utility scale wind farms. The scale model wind turbine used in this study has a three-blade GWS/EP-5030x3 rotor (designed for model aircraft, but blade profiles are nearly flat) with a diameter (D) of 0.128 m and a hub height of 0.104 m. Specific rotor geometry can be found in Howard et al. [58]. The hub height was placed inside the lowest 25 % of the boundary layer, which is typical for utility-scale turbines in the ABL. The tip-speed ratio $\lambda \approx 4.5$ of the turbine model is within the design range for utility-scale turbines, typically between $\lambda \approx 3.5$ and 10, while the physical model dimensions were scaled to roughly match a full-scale turbine. The hub velocity used for each of the cases presented herein was approximately 2.4 ms^{-1}, independent of thermal stability. The speed selected was above the lowest cut-in speed of the turbine (2.1 ms^{-1}), yet allowed the largest impact from thermal effects. The tunnel drive fan was held at a constant rpm (as prescribed by measurements from a Pitot-static tube at hub height in the baseflow for each stratification).

The test turbine produces voltage through a DC generator that had an electrical load and mechanical torque proportional to the generator speed that was driven by the wind force, not by an outside electrical source. The generator was able to produce power at the angular velocity of the rotor such that no gearbox was required. The peak coefficient of power for this rotor-turbine configuration is 0.17 [58]. This model is the same turbine used by Chamorro et al. (2009)[20] and Zhang et al. [43] and it should be noted that the instantaneous near wake flow ($x/D < 0.5$) is dominated by the specific geometry of the model and therefore cannot be directly related to full scale turbines. However, the information this study provides on the incoming flow conditions and mean wake regions for the turbine can be used as a first-order investigation for full-scale turbine siting and as a validation tool for computational models (Yang et al. [59]).

A three-dimensional, sinusoidal hill was designed to study the influence of terrain variation on wind turbines and wind farms. The hill design has a circular plan view and

a sinusoidal front profile with a crest height of 0.10 m (same as the turbine hub height) and a base diameter of 0.30 m [profile shown in Figure 3.1(b)]. The hill was made from plaster using a female mold milled by a computer numerical control (CNC) machine.

A PIV system was employed to capture detailed flow field information upwind and downwind of the turbine as well as in the wake of the hill. The PIV system was comprised of TSI Insight 4G software coupled with a TSI synchronizer, which controlled the timing between the Big Sky dual-head Nd:YAG laser and, two TSI PowerView Plus cameras. The 532 nm YAG laser was used to illuminate olive oil seeding particles in the flow, with diameter on the order of 10 microns [60] generated by forcing compressed air through a Laskin nozzle placed in a container of liquid olive oil. Images were acquired simultaneously from both 2048 pixel x 2048 pixel CCD cameras in standard PIV mode. Capturing with two cameras extended the investigation window, and in turn, provided a flow field with a total x-axis breadth $\approx 2.5D$. The sampling frequency for the PIV system was 7.25 Hz while obtaining data with the wind turbine and 3.63 Hz for the three baseflow tests to provide a longer capture time for the ensemble average.

The cameras were positioned to capture the inflow, from nearly $1.2D$ upwind, and the wake, to $1.3D$ downwind of the rotor plane [as shown in cross-hatched portion of Figure 3.1(b)]. Placing the cameras near the turbine provided an estimate of the turbulent flow structures which directly impinge upon the rotor. A series of positions along the centerline in the hill wake were taken to contribute information on the wake development and to characterize the turbulent flow interaction between the topographic perturbation and boundary layer [all frames, including cross-hatched, in Figure 3.1(b)].

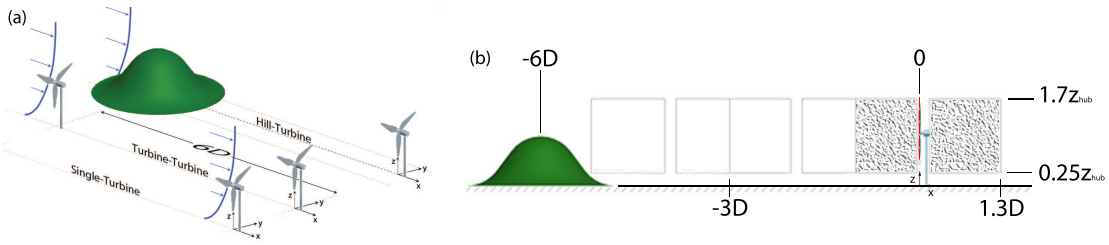

Figure 3.1: Schematics depicting (a) the three test arrangements (ST, TT, HT) and (b) the PIV measurement locations for experiments with the turbine (shown as cross hatched area) and for the hill wake (all frames outlined by grey rectangles)

3.3 Experimental Results

3.3.1 Boundary Layer Flow Characterization

The flow structures present in the ABL have been shown to influence both mean and unsteady quantities of turbine performance ([58]). We first investigate the mean and fluctuating velocity field statistics of the baseline turbulent boundary layer, in the three thermal stability regimes investigated here. Figure 3.2(a) provides the mean flow profiles and thus the stability-specific mean shear that characterizes the rotor area. The temperature profiles for the stable and convective boundary layers are included in Figure 3.2(b). The thermal shear over the rotor is found to be greater under the convective condition, as compared to that of the stable thermal stratification. Our shear velocity estimate for the neutral condition was confirmed by direct measurements of the Reynolds stresses, fitting of the logarithmic law on the mean velocity profile and through a comparison with normalized near wall statistics provided in Adrian et al. (2000)[61]. The shear velocities for the convective and stratified regimes were estimated from the peak of the Reynolds stresses, $u_* = \sqrt{\overline{(u'w')}_{max}}$. Figure 3.3 shows the streamwise turbulence intensity, vertical turbulence intensity and Reynolds stresses versus momentum thickness Θ.

Next we inspect the organization and inclination of the coherent motions of turbulent structures in the baseline boundary layer for each thermal stability condition and compare them to those found in the ABL (structure inclination shown by Chauhan et al. [62]) using the two-point correlation function as defined in Equation 3.1, assuming homogeneity in the flow direction:

$$R_{u'u'}(r_x, z, z_{ref}) = \frac{\langle\langle u'(x, z_{ref}, n)u'(x + r_x, z, n)\rangle_x\rangle_n}{\sigma_{u(z_{ref})}\sigma_{u(z)}}; \tag{3.1}$$

where u' is the fluctuating velocity in the x-direction, r_x is the radius separating the two inspection points and n refers to the vector field number. Figure 3.4 shows the correlation map that provides the means to calculate the structure inclination angle γ, as computed using 2000 vector fields. The z_{ref} denoted in Equation 3.1 was taken as the lowest z-elevation in the PIV field of view not influenced by edge effects, namely $z/\delta \approx 0.08$. Marusic and Heuer [63] showed that computing the inclination angle using τ (i.e. $R_{\tau,u}$) produced γ angles independent of the elevation of z_{ref}. However, as we

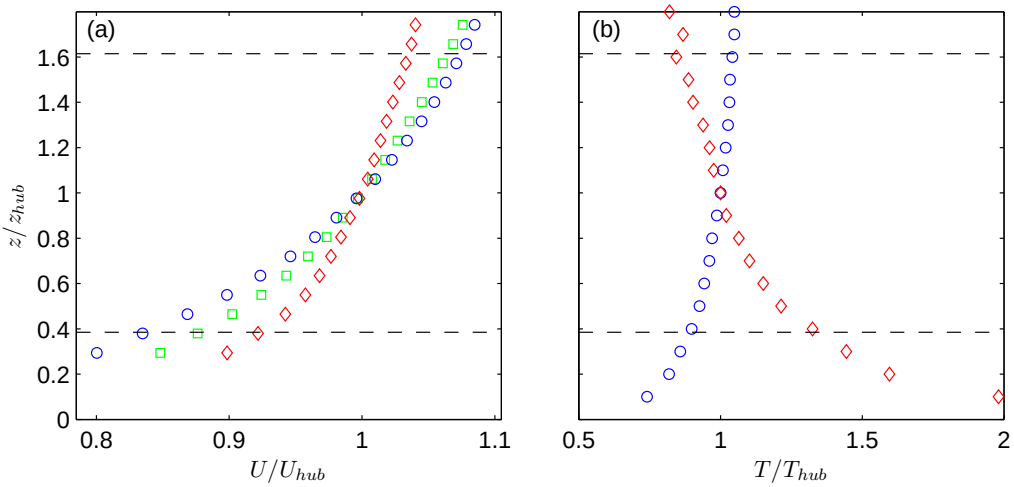

Figure 3.2: Lowest portion of boundary layer profiles where rotor operates: (a) mean streamwise velocity U normalized with the mean hub velocity (U_{hub}) and (b) the temperature profiles normalized with the temperature at the hub (T_{hub}). $\square$ indicates neutral stratification, while $\circ$ and $\diamond$ refer to stable and convective stability, respectively. The black, horizontal dashed lines represent the bottom and top-tip elevations of the rotor.

did not directly measure the local shear stress, our estimate of γ was calculated using the streamwise and vertical distances separating the reference location and the greatest linear distance of a given value of R_{uu} (0.6 was used herein) [64]. Under neutral stability [$Ri_b = 0$, shown in Fig. 3.4(a)], γ was found to be 9.3^o. It is in agreement with ABL measurements from Marusic and Heuer [63] ($\gamma = 11.8^o$), but much lower than that of Carper and Porté-Agel [65] ($\gamma = 16^o$). An alternative method to calculate γ consisting of coupling R_{uu} at constant heights ([62], among others) was found to produce values above 20^o. Marusic and Heuer (2007)[63] also showed that γ is nearly independent of Reynolds number, and therefore, our results in the neutral regime are assumed to be comparable to those from the ABL.

Under thermally stable stratification, the structure angle was estimated using the $R_{uu} = 0.6$ contour plotted in Fig. 3.4(b), leading to $\gamma = 11.8^o$, a value higher than the correspondent one in the neutral case. Carper and Porté-Agel [65] also provided data suggesting that weakly stable conditions (near-neutral) in the ABL might have

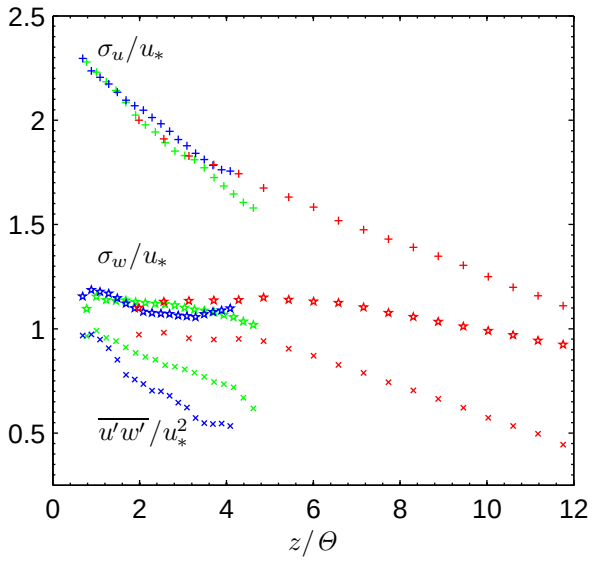

Figure 3.3: Root mean square of streamwise (+) and wall-normal ($\star$) velocities and Reynolds stress (x) normalized by the shear velocity u_* for the respective thermal condition. The colors green, blue and red represent neutral, stable and convective profiles, respectively.

an increased range of inclination angles. It should also be noted that the contours in the stable case do not expand in the vertical direction as much as either the neutral or convective stability conditions, which corroborates findings by Chauhan et al. [62] that the inclined structures in the stable regime near the surface are still present, but with far less vertical extent when compared to neutral or convective stability regimes. Also, as our tests were conducted in a weakly stable boundary layer, the effects of thermal stratification have less ability to alter the inclination angle, as compared to stable boundary layers with larger temperature gradients.

The cross-correlation for the convective boundary layer is shown in Fig. 3.4(c) and the structure inclination was calculated to be $\gamma = 11.7^o$. This is much less than the $\gamma = 34$ found by Chauhan et al. [62], but is closer to the weakly convective conditions presented by Carper and Porté-Agel [65] with angles estimated between 15^o and 17^o. Opposite to the stable case, the convective correlation contour exhibits an expansion

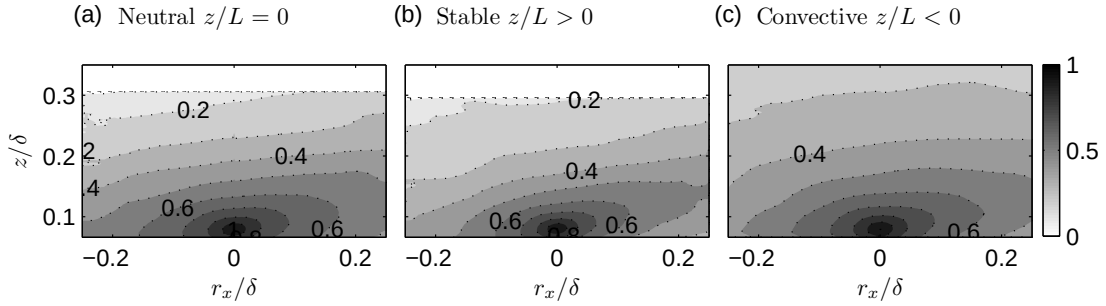

Figure 3.4: Two-point correlation of the baseflow for (a) neutral, (b) stable and (c) convective thermal stratifications. Both the x and z axes are normalized by the boundary layer thickness of the thermal stratification in question.

in the vertical direction; this suggests that the positive buoyancy created by the warm air rising from the surface of the wind tunnel interacts with and modifies the turbulent flow structures in a similar manner to that expected in the ABL.

It is important to note that the boundary layer thickness might be another factor to consider when comparing the inclination angle between various thermal stratifications. As shown in Stull (1988)[42], the convective ABL height is larger than the stable and neutral cases. However, wind tunnel measurements in the convective regimes (here and Zhang et al. 2013 [43]) show a reduced δ and increased shear at the wall, as compared to the other stability conditions. We infer this is not an artifact but rather an effect of the Reynolds number: the ABL δ is roughly defined as the top of the mixed layer which cannot be observed at the laboratory scale (without heavy modification to the standard tunnel design) due to fetch limitation (or resident time) which hampers the growth of large scale structures and restricts the interaction between well developed large scale thermal plumes and the boundary layer structures. Therefore, the increased mean shear results in a reduced δ, which then restricts the vertical growth of the ramp like structures, induced by a decrease in TKE production far from the wall (driven by the decrease of dU/dz as $z \to \delta$). Here we again note that the restriction in thermal stratification imposed by the range of operating temperatures for the floor surface and air, in addition to flow speed, also limits the vertical transfer of TKE and subsequent

vertical growth of ramp like structures. We provide here an attempt to compensate for the vertical confinement of the boundary layer by introducing a correction factor defined as δ_N/δ_S, where N indicates neutral condition and S indicates a specific thermal condition. The resulting compensated inclination angles γ_{SC} can be computed thus as $\gamma_{SC} = \gamma_S * \delta_N/\delta_S$. From a pure phenomenological perspective, the inclination angle is adjusted in reference to the boundary layer height in order to compensate for the (Reynolds number dependent) confinement effect exerted on the growth of stablility-specific ramp like structures. The resulting compensated inclination angles are $\gamma_{SC} = 9.3^o, 11.4^o$ and 17.0^o for the neutral, stable and convective boundary layers, respectively. The compensated convective inclination is closer to that presented in Carper and Porté-Agel [65] for the weakly convective conditions. Although this discussion remains at the speculative level, it does originate from a legitimate question: how is the larger mean shear of the surface layer in the convective regime (observed here and in the ABL across a wide range of Reynolds numbers) related to boundary layer height, specifically in the absence of a well defined mixed layer.

3.3.2 Combined Thermal and Topographic Effects on the Flow

We inspect here the inflow conditions for the turbine under different stability and upwind perturbations (i.e. baseflow for ST, another model turbine for TT, and the sinusoidal hill for HT). The normalized mean streamwise velocity profiles $1D$ upwind of the turbine are shown for the turbulent boundary layer, turbine wake and hill wake in Figure 3.5(a), (b) and (c), respectively. The largest difference between the inflow for the three cases (ST, TT, HT) is the overall shape of the profiles. The boundary layer is slightly modified by the thermal stability upwind of the rotor for the single turbine case [Fig. 3.5(a)], but also note that the mean velocity at $1D$ upwind of the turbine is modified by the turbine presence; therefore, normalized velocity statistics are not expected to collapse at z_{hub}, as would be the case for undisturbed flow (Fig. 3.2). While the mean shear exhibits the same qualitative behavior observed in the undisturbed boundary layer, the effect of the hub and rotor blockage depends on the stability regime and rotor angular velocity. The mean velocity profiles shown in Figure 3.5 (b) and (c) are dominated by the respective upwind perturbation. In Figure 3.5(b), the preceding turbine hub exerts a blockage causing the deepest reduction in mean velocity while the upper and lower shear

layers develop as a result of the interaction between the turbine wake, tip vortices and turbulent boundary layer. Chamorro et al. [31] proposed that the turbine removes the largest flow scales from the wake, and as such, adjusts the energetic content of the wake flow (significant large flow scale removal noted into far wake, precise downwind distance depends on flow speed). Here we corroborate the idea that the wake is controlled by the mixing induced by the turbine rotor, given the small difference in velocity profiles for the inflow to the downwind turbine in the turbine-turbine case, see Figure 3.5(b). The largest difference between thermal regimes occurs near the bottom-tip of the rotor where turbulent heat flux and mean temperature gradient effects modify the transfer of energy in the wake, and in the convective case, the wake deficit is reduced through higher vertical mixing. Enhanced turbulent fluctuations, similar to those induced by the turbine rotor, are found in the wake of the hill [Fig. 3.5(c)]; however, as the flow is accelerated over and around the hill, the signature of the thermal stability regime is not entirely removed, as buoyancy still influences the mean shear and mixing processes. The hill wake is characterized by a velocity deficit that follows the width of the hill [i.e. the deficit is proportional to the hill width, see Fig. 3.5(c)]. The neutral and stable profiles are very similar, however, the shear over the rotor plane and streamwise acceleration over the top of the hill are observed to be attenuated in the convective case.

A greater departure between profiles due to thermal effects can be seen from the r.m.s. of the streamwise velocity, shown in Fig. 3.6. As in the case of the mean velocity, the distinct shape of the profiles in Fig. 3.6(a), (b) and (c) are due to their respective inflow conditions (turbulent boundary layer, turbine wake and hill wake). The turbulence intensity (σ_u/U_{hub}) profiles for the turbulent boundary layer are found to be similar to those presented by Zhang et al. [43]. Note the PIV window presented here does not capture the near wall region ($z^+ < 200$) where the convective ($\Diamond$) condition exhibits the highest fluctuations, as compared with to the other two regimes. In the wake of the turbine for all thermal regimes [Fig. 3.6(b)], the velocity deficit introduced by the upwind turbine and the tip vortices produce a shear layer near the top-tip with increased streamwise fluctuations with respect to the baseflow case shown in Fig. 3.6(a). This figure also shows the influence of convective stratification on the streamwise r.m.s. velocity, most notably the increase in the lower half of the profile in the turbine wake Fig 3.6(b), supporting the results of Zhang et al. [43] and Howard et al. [1]. The increase in

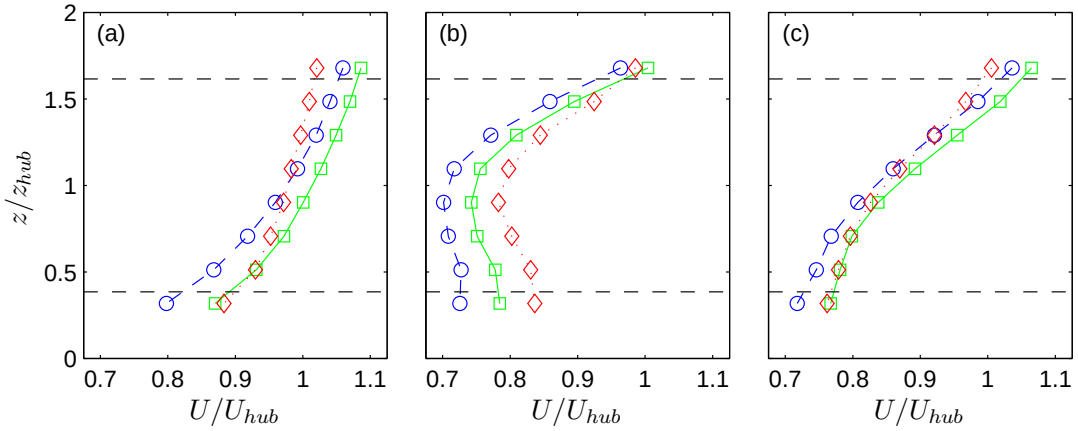

Figure 3.5: Streamwise velocity profiles taken $1D$ upwind of the model turbine normalized by the stability specific U_{hub} from baseflow condition (no turbine) for the (a) single turbine, (b) turbine-turbine and (c) hill-turbine cases. $\square$ indicates neutral stratification, while $\circ$ and $\diamond$ refer to stable and convective stability, respectively. Horizontal dashed lines represent the bottom and top-tip locations of the turbine rotor.

fluctuations is assumed to originate from the increased Reynolds stress of the convective boundary layer across the entire rotor region (Fig. 3.3) (coupled with contributions from an increased mean shear adding to higher TKE production) in conjunction with the low speed wake and mixing introduced by the rotor. Note that the elevated streamwise turbulence intensity observed in the convective turbine-turbine case is consistent with the observed reduced wake deficit (i.e. faster wake recovery) as a result of more effective entrainment, opposite to the hill-turbine case where similar turbulence intensities [Fig. 3.6(c)] between the thermal regimes lead to similar mean wake velocity profiles. The hill wake turbulence intensity profiles do show that flow acceleration occurs over the crest of the hill as well as around the side, in addition to vortex shedding from the hill precipice as indicated by an increase in r.m.s at $z/z_{hub} = 1$. The flip in highest fluctuations between the convective ($\Diamond$), neutral ($\square$) and stable ($\circ$) profiles as z increases can be attributed to the difference in mean shear and turbulence levels.

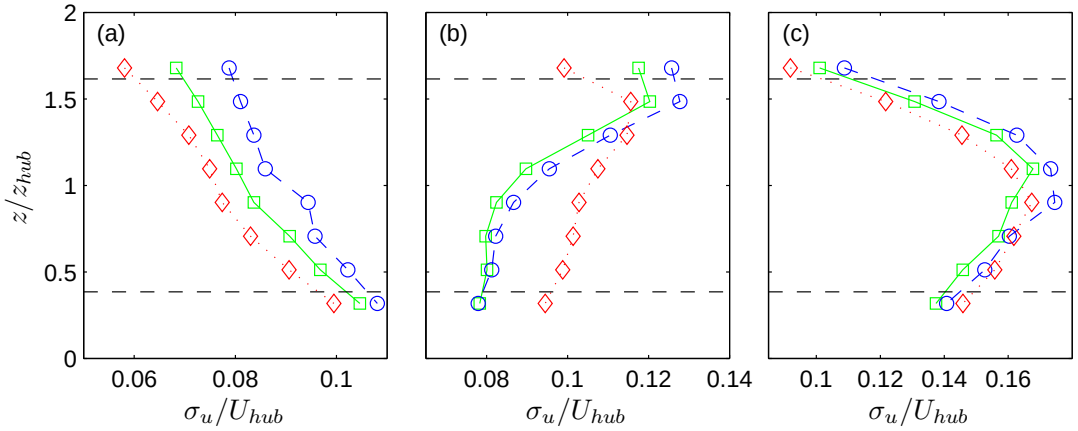

Figure 3.6: Turbulence intensity (σ_u/U_{hub}) $1D$ upwind of the turbine for the (a) single turbine, (b) turbine-turbine and (c) hill-turbine cases. $\square$, $\circ$, $\diamond$ indicate neutral, stable and convective stability, respectively. Horizontal dashed lines represent the bottom and top-tip locations of the turbine rotor.

3.3.3 Turbine Voltage Statistics

The turbine voltage mean and r.m.s. values are given in Table 3.3.3. As expected, the voltage comparison shows that an upwind blockage causes a reduction in mean voltage due to the reduction in mean velocity (as shown by the inflow profiles in Figure 3.5) [1]. The thermal stability of the boundary layer does not have a large impact on the mean voltage trend for each of the cases, but minor differences do show that the increased mixing within the convective boundary layer for the turbine-turbine and hill-turbine cases cause the downwind turbine to have a mean voltage production greater than or equal to the single turbine case, as compared to the other stability conditions. Table 3.3.3 also shows the result of the linked effects from stability parameters and flow perturbations on the fluctuating voltage, a quantity which can be used as a measure of unsteady loads induced by the turbulence.

Table 3.2: Turbine voltage under different flow conditions (format taken after [1]).

Turbine	Neutral			Stable			Convective		
Operation	ST	TT	HT	ST	TT	HT	ST	TT	HT
Voltage [V]	0.164	0.124	0.143	0.165	0.123	0.143	0.160	0.134	0.143
$\frac{V_{xT}-V_{ST}}{V_{ST}}$ [%]		-24.3	-13.0		-25.5	-13.3		-16.3	-10.5
Voltage RMS [V]	0.0034	0.0019	0.0036	0.0037	0.0021	0.0033	0.0029	0.0026	0.0032
$\frac{V_{RMS_{xT}}-V_{RMS_{ST}}}{V_{RMS_{ST}}}$ [%]		-44.1	5.9		-44.2	-10.8		-10.3	10.3

V_{ST} = ST mean voltage;
V_{xT}, variable replaced by V_{TT} or V_{HT} dependent on case;
$V_{RMS_{ST}}$ = ST fluctuating voltage;
$V_{RMS_{xT}}$, variable replaced by $V_{RMS_{TT}}$ or $V_{RMS_{HT}}$ dependent on case

The reduction in voltage fluctuations between the single turbine and turbine-turbine cases is similar for all stability conditions, again supporting the findings of Chamorro et al. [20, 17] and Howard et al. [58] that an upwind turbine reduces the energy of the large scales of the incoming flow, modifying the flow power spectral density in the wake [66], and ultimately sheltering downwind turbines from significant flow length scales at or above the rotor scale. The neutral and stable turbine-turbine cases had similar fluctuation reductions of 44% as compared to the single turbine in their respective thermal condition, which is in agreement with the nearly identical profiles shown in Figures 3.5(b) and 3.6(b). A reduction, although smaller at 10%, is recorded for the convective turbine-turbine case and again is similar to the increase shown by the $\Diamond$ profile in Fig. 3.6(b). However, while the voltage and velocity fluctuations statistics for the turbine-turbine case support one another, the hill-turbine voltage r.m.s. values do not reflect the minimal changes found in the profiles displayed in Fig. 3.6(c).

In the hill-turbine case, the downwind turbine voltage fluctuations increased for both the neutral and convective stratifications, at 6% and 10% respectively. This increase is due to vortex shedding from the hill peak $z/z_{hub} = 1$ [streamwise direction as found in Fig. 3.6(c)] and von Kármán vortex shedding (spanwise direction), as discussed in Howard et al. [58]. Essentially, the hill introduces large scale motions (larger than the rotor scale) to which the downwind turbine is observed to respond. However, under stable thermal stratification, the turbine voltage in the hill wake exhibits a reduction in fluctuations of nearly 11%, as compared to the single turbine case under the same stratification. While the single turbine case for the stable boundary layer has the highest fluctuations out of all three stratifications, the percentages are calculated with respect to each of the stability specific single turbine cases. The decrease in turbine voltage fluctuations for the stable hill-turbine case must therefore be an idiosyncrasy of the complex linkage between hill shed vorticies and thermal effects of the stable stratification on the evolution of large scale motions. To investigate this linkage, we move to inspecting the hill wake.

3.3.4 Hill Wake Evolution

The contours of streamwise velocity and turbulence intensity downwind of the hill are shown in Figure 3.7(a) and (b) respectively, both under neutral thermal conditions. The

mean velocity shows a large velocity deficit with recirculation (reverse flow in region near $x/D \approx -5$ and $z/z_{hub} \approx 0.5$) in the near wake with gradual velocity increase farther downwind, indicative of a blunt body wake. The contour of streamwise fluctuating velocity highlights the vortex rolling off the hill peak along with the spanwise shedding of von Kármán vortices. Windows (c), (d), (e) in Fig. 3.7 show the influence of thermal stratification on the streamwise velocity fluctuations at top-tip, hub and bottom-tip elevations, respectively. Fig. 3.7(f), (g) and (h) track vertical fluctuations in the hill wake for the same top-tip, hub and bottom-tip locations. Inspecting the comparison panels does not lead to any noticeable deviations that may describe changes in the flow that would cause the difference in voltage fluctuations between the thermal conditions. The largest difference in fluctuations, both streamwise and vertical, is at the bottom-tip near $x/D \approx -4$, thus close to the wall where thermal effects are significant due to the large gradient in mean temperature and low mean velocity. At hub height, the wake is clearly driven by the geometry of the hill, as no significant deviation appears between the three temperature stratifications. The wake comparison at the top-tip shows a slight difference between the convective case and the neutral and stable [Fig. 3.7(c)]. The reduction in σ_u here for the convective case is due in part to the reduced local shear at this elevation (based on boundary layer thickness), which is driven by the relative height of the hill with respect to the boundary layer height. The vertical fluctuations at the top-tip location do not exhibit any large variation in horizontal profiles between the different stratifications, including the location of the shear layer growth in Fig. 3.7(f), starting around $x/D = -2$. However, the PIV is capturing fluctuating velocities which originate from all sizes of turbulent structures, and because the turbine cannot respond to any fluctuating scales smaller than half a rotor diameter, a statistical inspection of the impinging turbulent scale sizes (cause) is required to investigate the source of the voltage fluctuations (effect).

3.3.5 Large Scale Turbulence Effects on Turbine Voltage Statistics

The fixed reference two-point correlation, defined in Equation 3.2, correlates the velocity field with the velocity at a reference location and provides statistical, quantitative information on the length and orientation of the dominant structures present in the flow. As large turbulent scales have more influence on the voltage fluctuations, two PIV windows

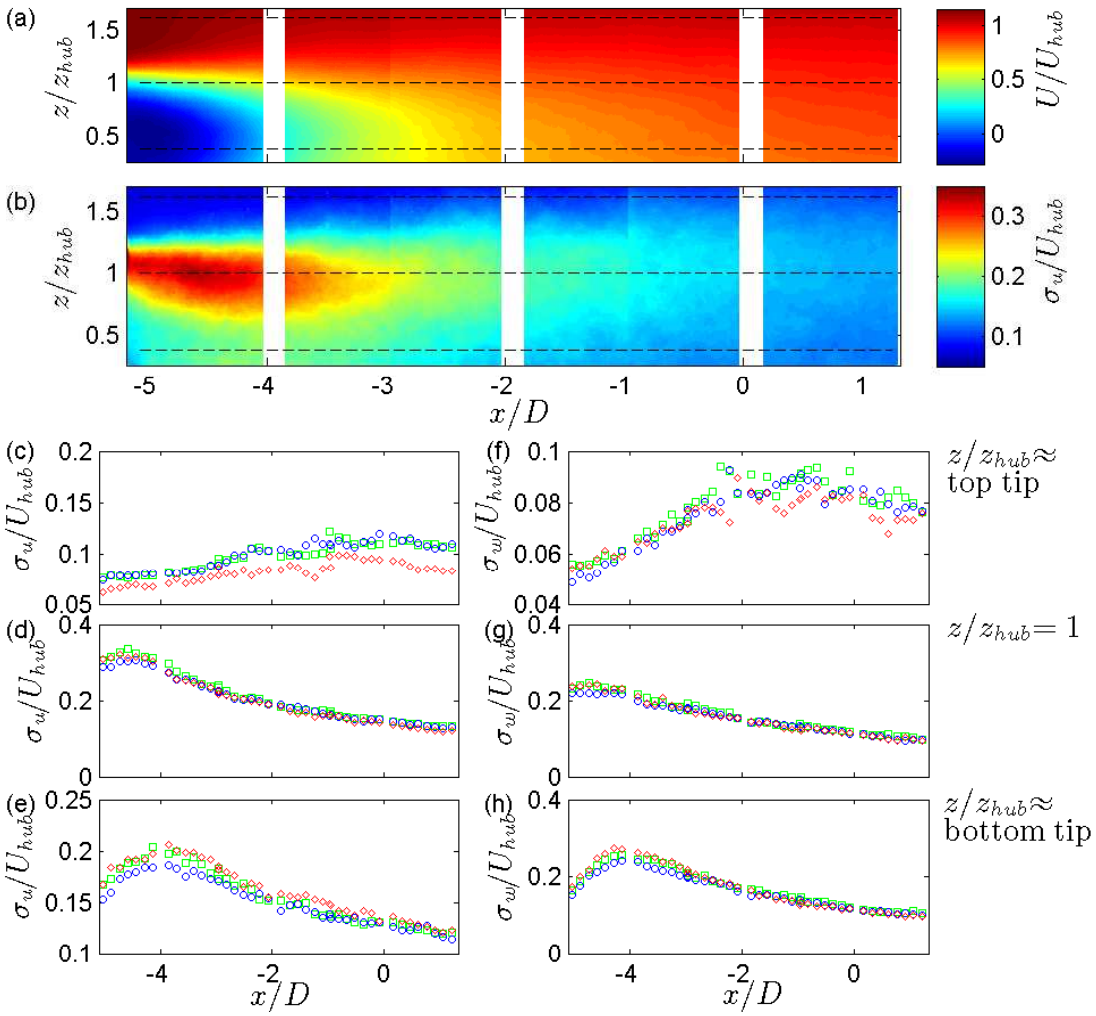

Figure 3.7: Contours of (a) mean streamwise velocity and (b) streamwise velocity fluctuations in the wake of the hill for neutral thermal condition, both normalized by the incoming neutral hub velocity. Dotted horizontal lines indicate top-tip, hub and bottom-tip. Streamwise velocity fluctuations in the hill wake are shown in (b), (c) and (d) for the top-tip, hub height and bottom-tip, respectively. Vertical velocity fluctuations downwind of the hill are shown in (f) for the top-tip, (g) for hub height and (h) for rotor bottom-tip. □ indicates neutral stratification, while ∘ and ⋄ refer to stable and convective stability, respectively. The hill is centered at $x/D = -6$.

taken simultaneously were used to compute $R_{u'u'}$, doubling the correlation field, and subsequently increasing the maximum length scale capturable. Since the flow is inhomogeneous in the vertical (typical of boundary layers) and horizontal directions (due to wake evolution), the reference value is a physical location in the flow field (x_{ref}, z_{ref}), not just a distance to the wall as was used in the estimate of the structure inclination angle.

$$R_{u'u'}(x, z, x_{ref}, z_{ref}) = \frac{\langle u'(x_{ref}, z_{ref}, n)u'(x_{ref} + r_x, z_{ref} + r_z, n)\rangle_n}{\sigma_{u(x_{ref},z_{ref})}\sigma_{u(x_{ref}+r_x,z_{ref}+r_z)}}. \tag{3.2}$$

Figure 3.8 displays a comparison between neutral (a, c) and stable (b, d) stratifications for the turbulent baseflow (a,b) and hill wake (c,d) without the turbine. First, comparing neutral to stable thermal conditions for the baseflow case, we see that structures in the stable thermal stratification have a longer spatial correlation (i.e. $R_{u'u'} = 0.5$, a contour value resolved in all four plots, extends further downwind in the stable case); this corroborates the finding that the single turbine in the stable case has a higher voltage fluctuation as compared to the neutral condition (see Table 3.3.3). Now, when comparing the baseflow to the hill wake, both thermal regimes have a reduction in correlation, as expected due to the disruptive effects of the hill; however, under stable conditions, the hill wake correlation experienced a greater curtailment: for $R_{u'u'} = 0.5$, under the stable regime, the contour is shortened from $x/D \approx 0.75$ in the baseflow to $x/D \approx -0.53$ in the hill wake, whereas in the neutral case, it only changes from $x/D \approx 0.32$ to $x/D \approx -0.54$. The result is a larger reduction in the size of statistically dominant turbulent structures present in the wake of the hill. In order to explore which turbulent length scales are impacting the turbine, we now analyze the turbine voltage signal.

Figure 3.9 shows the premultiplied voltage spectra from each turbine arrangement within the three stability regimes, neutral, stable and convective in panels (a), (b) and (c), respectively. The spectra are normalized with the variance of the single turbine case for each specific thermal stability condition, which allows the comparison of the scale-by-scale energetic budget. For instance, inspecting the HT case in neutral condition, red dotted line in Fig. 3.9(a), we observe that the turbine is registering higher voltage fluctuations as compared to those measured by the turbine in the baseflow (blue solid line) at a normalized frequency $fD/U_{hub} \approx 0.02$ (equivalent to turbulent length scales

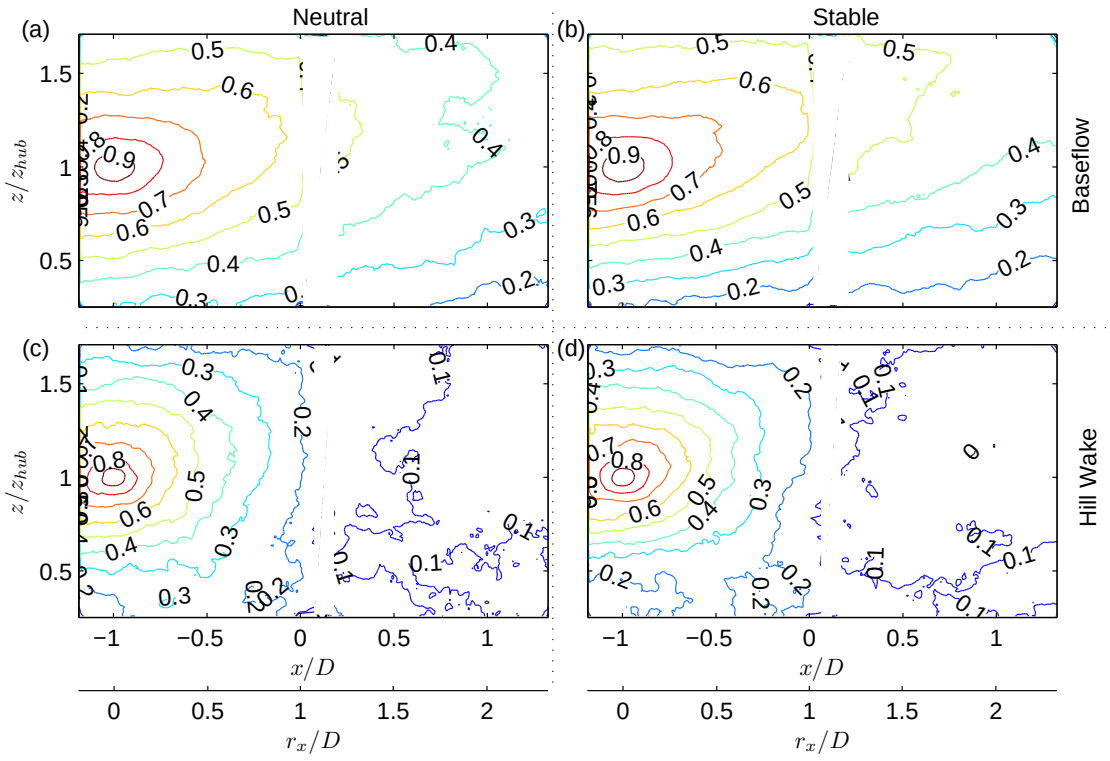

Figure 3.8: Two-point correlation contours of streamwise velocity for neutral boundary layer (a) baseflow, (c) hill wake (hill center placed at $x/D = -6$) and stable thermal stratification (b) baseflow, (d) hill wake.

on the order of 10δ). Note that this length scale is consistent with the largest scale of the turbulent boundary layers (see Hutchins & Marusic [67], Smits et al. [68], Guala et al. [26], among others); however, while it remains notably smaller than the upwind fetch, the actual length may also be slightly overestimated due to the inertia of the turbine rotor. Inspecting the voltage spectra in the convective regime, Fig. 3.9(c), a prominent peak at a higher frequency than the largest scale structures is seen in the hill-turbine spectra at $fD/U_{hub} \approx 0.1$. Using Taylor's hypothesis of frozen turbulence and von Kármán's vortex shedding equation to provide a rough estimate, it was found that the frequency range around this peak is actually the von Kármán vortex shedding from the hill, $f_s D/U_{hub} = [0.198U/d_{hill}(1 - 19.7/Re_{hill})]D/U_{hub} \approx 0.1$, using $U = 2[ms^{-1}]$,

$d_{hill} = 0.2[m]$. As was proposed by Howard et al. [58], the hill can be characterized as a cylinder of varying diameter, which will produce a range of vortex sizes. This means that the fluctuations caused by the hill and registered in the voltage can be found in the spectra within the frequency range defined by the hill cross-section size. In viewing windows (a) and (b) in Fig. 3.9, the influence of the hill can be found around $fD/U_{hub} \approx 0.1$ (on the order of 2δ). This means that in the stable case, the added turbulence by the hill is still felt by the turbine; however, it appears that the hill is deflecting some of the largest energy containing turbulent structures (see the reduction of the peak at large scale in the stable stratification for the hill case) that are the main contributors to the voltage fluctuations. Here we suggest that the reduction in the r.m.s. voltage is due to the combined effects of upwind topography (the blockage and vortex shedding from the hill) integrated with changes of the large scale energetic motions induced by the stable stratification. The dampening of turbulent fluxes and vertical fluctuations are expected to favor spanwise motions and thus the deflection of energetic turbulent structures by the hill, leading to a sheltering effect for the $6D$ downwind turbine.

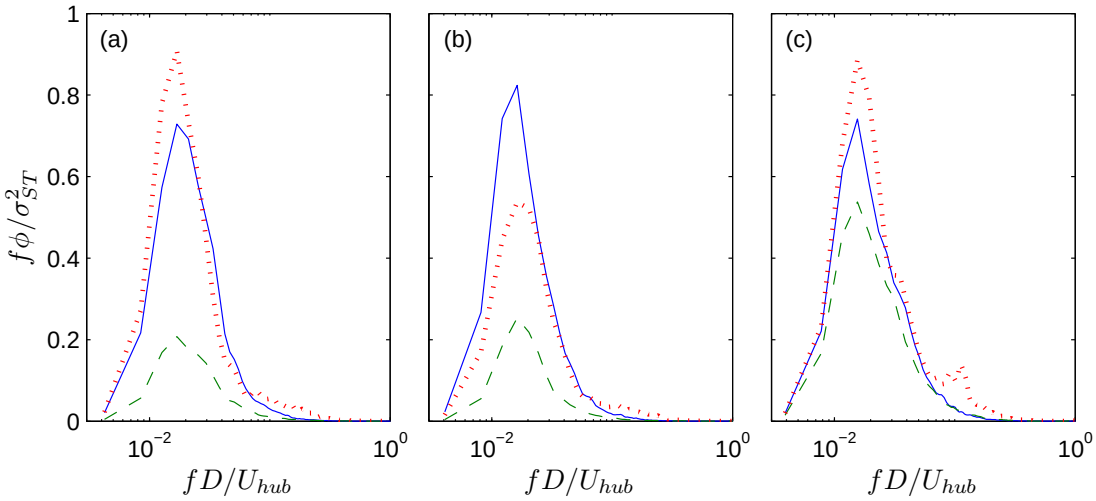

Figure 3.9: Pre-multiplied turbine voltage spectra from each case (ST, TT, HT) for (a) neutral, (b) stable and (c) convective stratifications. Normalization is completed using the variance from the single turbine (σ_{ST}) case under the respective thermal stratification and ϕ is the voltage spectrum. Solid line indicates single turbine, dashed line denotes turbine-turbine and the dotted line displays the hill-turbine case.

3.4 Summary

Experiments were performed in the SAFL atmospheric boundary layer wind tunnel to study the response of a model wind turbine to a set of upwind perturbations. Weakly stable and convective boundary layers were reproduced by independently controlling the temperatures of the freestream air and the wind tunnel floor. A three-dimensional sinusoidal hill and a turbine were selected as upwind perturbations for the model test turbine in an effort to distinguish flow complexities experienced by turbines in hilly terrain. PIV flow measurements allowed the comparison of mean and higher order flow statistics in the wake of the turbine and the hill to those obtained in the undisturbed turbulent boundary layer. In conjunction with the flow data for the nine cases (three thermal stabilities for the three turbine configurations of single turbine, turbine-turbine and hill-turbine), the turbine response was recorded through the output voltage of the turbine's DC generator (see Howard et al. [58]). Particular emphasis was devoted to couple turbine voltage statistics with a statistical description of the turbulence structures impinging upon the rotor. We first investigated the effects of the different thermal stability conditions on turbulent statistics of the boundary layer flow. The mean and fluctuating velocity components profiles, in addition to the large scale turbulent structure inclination angle, were compared to quantify stability-specific differences in the incoming flow perceived by the turbine model. Then we compared various hill-turbine(s) configuration, under the three stability conditions. The major findings of this work can be summarized as follows:

- The mean turbine voltage, which describes the average angular velocity of the rotor, was observed to be reduced from the single turbine case when the test turbine was placed either in the wake of a turbine or in the wake of a hill, independent of the thermal stability. This was consistent with the observed mean velocity deficits.

- In all thermal stability conditions, an upwind turbine causes a reduction in the downwind turbine voltage r.m.s. as the large scales of the incoming turbulent flow (which are strong enough to induce changes in rotation speed) are, at least partially, removed from the wake (see also Howard et al. [58]).

- The convective thermal regime has the greatest influence on the mean and r.m.s.

velocity profiles in the turbine wake, enhancing wake recovery through increased mixing (as compared to the other thermal conditions, see Figure 3.6(b)).

- The interpretation of voltage r.m.s. for the hill-turbine case was not trivial and required combined statistical analysis of the flow and voltage data for the three thermal regimes. Contrary to the other two regimes, the stable hill-turbine case showed reduced voltage fluctuations. The two-point correlation of the streamwise velocity fluctuations pointed to a reduction in the largest turbulent length scales in the hill wake for the stable regime, which was confirmed in the analysis of the premultiplied voltage spectra. Not only was it found that the vortices shed by the hill could be identified via the von Kármn equation and the spectral data, but also that the energetically relevant, incoming, large flow structures are governed by coupled topography-thermal stratification effects. Under thermally stable conditions, we infer that the large scale structures from the incoming flow are diverted in the spanwise direction, thereby limiting their induction into the hill wake, such that ultimately they do not impact the turbine rotor. This phenomenon can be labeled as a thermal stability-specific hill sheltering effect.

Future work will explore spanwise flow measurements and various hill-turbine spacing to understand how the naturally present turbulent flow structures interact with the hill-induced turbulence. Also, the three simple cases (single turbine, turbine-turbine and hill-turbine) will be expanded to include multiple rows of turbines and complex topographic arrangements to provide high fidelity benchmark experiments for full wind farm applications and numerical code validation.

Chapter 4

Analysis of atmospheric inflow conditions for upwind preview to a horizontal axis wind turbine: a wind tunnel and field-scale study

This chapter takes a step toward (i) ensuring that the model wind turbine used in the tunnel is representative of what occurs at the full-scale and (ii) applies the knowledge gleaned from the previous two chapters on turbine operation and atmospheric influences and investigates how the inflow influences the turbine output. Data collected at the Eolos wind research facility and in the SAFL atmospheric boundary layer wind tunnel are used to study the impact of turbulent inflow conditions on the performance of a horizontal axis wind turbine. The Eolos test facility comprises a 2.5 megawatt (MW) Clipper Liberty C96 wind turbine, a meteorological tower and a WindCube lidar wind profiler. A second set of experiments was completed using particle image velocimetry (PIV) upwind of a miniature turbine in the wind tunnel to complement lidar measurements near the Eolos turbine. Joint statistics, most notably the temporal cross-correlations between wind velocity at different heights and turbine performance, are presented and compared at both the laboratory and field-scales. The work (i) confirms that the turbine exerts a blockage effect on the mean flow and (ii) provides a key identification of a

specific elevation, above hub height, where the incoming velocity signals are statistically relevant to turbine operation and control. Wind tunnel measurements however suggest that hub height velocity measurements are optimal for wind preview in aligned turbine configurations, and can thus be used as input to active control strategies for turbines within wind farms.

Submitted in shortened form to *Wind Energy*, June 2014.

4.1 Introduction

Renewable forms of energy production, such as wind power, have been gaining recognition and support as alternative power sources in an effort to mitigate climate change and anthropogenic effects on the environment. U.S. energy production from wind was at just over 60,000 megawatts (MW) at the end of 2012 (AWEA 2013 [69]), marking a 28% increase in power production with respect to the previous year by adding 6,751 turbines. As the number of turbines increase worldwide, there is a pressing need to improve material properties (Buckney et al. 2013 [70]), to better understand causes of failure, to increase the device lifetime and discern placement effects of turbines on non-ideal terrain.

Energy production from a horizontal axis wind turbine depends, among other factors, on the local incoming wind flow to the rotor and its temporal and spatial variability. As the size of the turbines increases (average rotor diameter now around 100 m), even sections of the individual blades can experience different local flow conditions leading to blade deformation and aeroelastic behavior due to the complexity and variability of the atmospheric surface layer. Spatio-temporal flow inhomogeneities thus have a strong effect not only on power fluctuations but most importantly on turbine blade loads. Researchers are now developing new ways of mitigating loading damage caused by wind gusts and continual variations of turbulent intensities by employing updated control logics, new blade designs and incoming flow forecasting. Wind turbine control designs include a wide spectrum of implementations, ranging from pitch control (Muljadi and Butterfield 1999 [71], Larsen et al. 2005 [72], Ozdemir et al. 2011 [73], Johnson et al. 2012 [74], etc.), to smart rotors and active flow control (Wingerden et al. 2008 [75], Lackner and van Kuik 2010 [76], Johnson et al. 2010 [77]), combining incoming

flow measurements with new control algorithms (Dunne et al. 2010 [78], Simley et al. 2012 [79], Mikkelsen et al. 2013 [80], etc.). All these techniques address the problem of maintaining high energy production while diminishing the detrimental impact wind gusts and turbulent fluctuations have on the turbine drivetrain and structural health.

Unfortunately, extreme wind events occurring in the operating range of wind turbines are not perceived by the feedback control in the majority of current utility-turbines, which, in fact, does not allow the prediction of instantaneous turbine loads (Moriarty et al. 2002 [81]); this is why recent advancements in remote sensing technology, e.g. forward facing light detection and ranging (lidar) devices mounted on utility-scale turbines, are envisioned to monitor the incoming wind conditions as an input to the control system. Outlier events, particularly in region 2 where nominal wind speeds are below the rated speed and the turbine is predominantly operated to increase generator speed (thereby increasing production), can be quite detrimental to the health and lifespan of turbine components. The control logic employed in the majority of wind turbines in the field today does not have the ability to foresee these wind gust events and, therefore, can only use real-time time analysis (feedback control loop) on the mechanical system to gauge the wind impact on the turbine. This means, that by the time the turbine feels a gust of wind impacting the blades and adjusts its operating condition, potential damage (high blade loading, large impulse to drivetrain, etc.) has already been incurred. Wind forecasting is a great tool that can track abrupt changes to the incoming flow in order to reduce loads, increase turbine lifespan and avoid catastrophic failure. As a first approximation, a simple and efficient turbine control system, designed to account for temporal variability of the incoming turbulent flows, may only require one specific velocity timeseries to be representative of the wind impacting the rotor, rather than a spatially resolved flow field.

The main focus of this manuscript is to utilize lidar instantaneous velocity profiles simultaneously acquired with the Eolos turbine's operational supervisory control and data acquisition (SCADA) data to study at which height the wind velocity gives the most representative velocity time history (where "representative" is intended with respect to power fluctuations and blade deformation). The proposed analysis is based on temporal cross-correlation of instantaneous power (from the turbine generators) and blade strain (from strain gauges mounted inside the blades) with velocity timeseries at different

heights (from lidar measurements). Because the wind turbine is expected to disturb the incoming flow in the close proximity of the rotor, we must first quantify the distortion of the mean flow field where upwind measuring sensors are likely to be placed. In other words, the question of defining the most representative velocity timeseries upwind of the rotor cannot be decoupled from the question on the local upwind flow distortion induced by the turbine itself. The method, description of meteorological conditions, and some results were presented in [82]. Here we expand on lidar specific postprocessing methods and introduce new experiments in the wind tunnel for comparative analysis on inflow, wake flow, and correlation statistics.

Wind tunnel testing is employed to study the mean and fluctuating velocity characteristics in the region upwind of the rotor using particle image velocimetry (PIV) and in the wake region using a high frequency hotwire anemometer. The wind tunnel data is compared with lidar data obtained at the same upwind and downwind locations of the Eolos turbine in addition to being used to explore velocity-power temporal cross-correlations in an aligned turbine-turbine configuration. We acknowledge that the voltage signal from the DC motor mounted on the turbine model [58] is only qualitatively comparable with the actual power from the Eolos turbine; however, when synchronized with PIV acquisition, it provides the opportunity to investigate turbine configurations that can not be studied at the Eolos field site. Wind tunnel measurements of spatially resolved flow fields (PIV) are thus important to (i) validate the lidar sampling technique in complex flows (see Section 4.2.1), (ii) confirm that correlation-based statistics are not contaminated by the lidar spatial averaging procedure, (iii) extend field scale results on optimal velocity input for wind preview to power plant scale applications (at least as guidelines in scaled wind tunnel experiments). The hotwire anemometer data taken in the turbine wake were used to ensure that the scale-model produced representative flow features.

This paper is outlined as follows. Section 4.2.1 describes the Eolos research facility, as well as the measuring equipment and the specific orientations of the WindCube lidar used in this research, and Section 4.2.2 provides a micro-meteorological description of the selected runs. Section 4.2.3 is devoted to the wind tunnel experiments, while the results from all tests are discussed in Section 4.3, and conclusive remarks follow.

4.2 Experimental Facilities and Setup

4.2.1 The Eolos research facility

The field-scale experimental data presented in this paper were collected at the Eolos wind energy research station located on the University of Minnesota Outreach, Research and Education Park (UMore Park) in Rosemount, Minnesota. This 5,000 acre complex is a part of the University of Minnesota and includes eighty acres devoted to wind energy research. On site equipment consists of a fully instrumented 2.5 MW wind turbine and a meteorological tower (denoted as met tower hereafter), in addition to a mobile WindCube lidar wind profiler. The terrain surrounding the turbine and met tower primarily consists of low, rolling farm land (local elevation change of 1-3 m with respect to the turbine base elevation), shown in Figure 4.1, with a few sparse tree patches and a few two-story buildings within a 2 km radius.

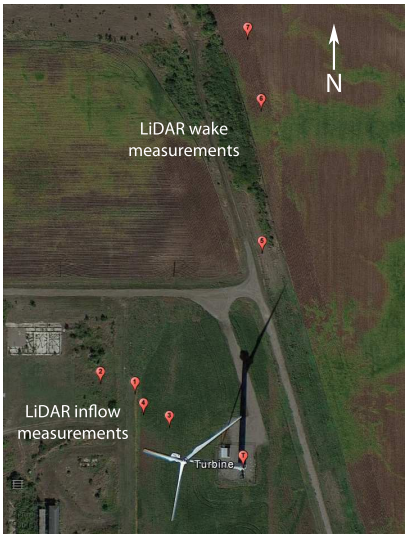

Figure 4.1: Satellite photo of Eolos research facility (Google map) with the GPS locations of the lidar deployment and measurements

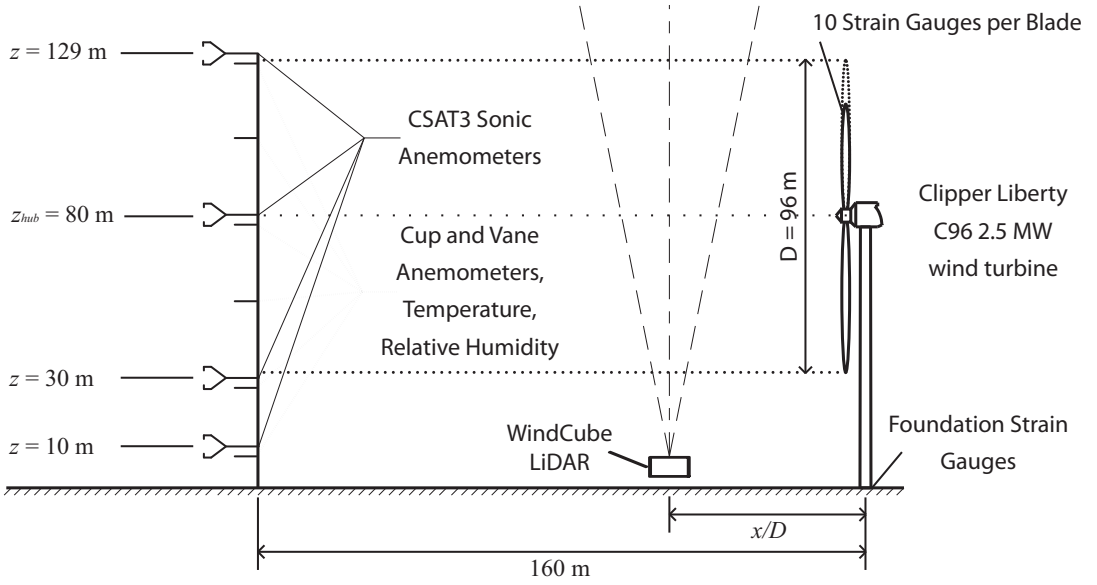

Figure 4.2: Schematic of data acquisition systems on the Eolos test site (adapted from Chamorro 2014).

Utility Scale Turbine

The Eolos wind turbine is a highly instrumented 2.5 MW Clipper Liberty C96 with a hub height z_{hub} =80 m and a rotor diameter D =96 m. Aside from the standard turbine supervisory control and data acquisition (SCADA) system which continuously monitors hundreds of variables on turbine operation, the Eolos turbine is equipped with twenty strain gauges placed at the connection between the base of the tower and the foundation to measure bending forces and moments. In addition, to quantify blade loading, strain gauges have been attached during turbine assembly inside each blade on both low and high pressure sides (at progressive distances from the root, specifically 0, 25, 37.5, 44.4 % of radius) and integrated into the data acquisition system together with two extra strain gauges at the leading and trailing edges on the blade root. All the data from the turbine is stored on local servers with a site-universal time stamp.

Meteorological Tower

A 130 m tall research met tower is located 160 m, approximately 1.7 D, due south of the Eolos wind turbine. The tower vertically covers the entire swept rotor area with three sonic anemometers (Campbell Scientific CSAT3) located at z = 30, 80, 129 m above ground, corresponding to approximately the turbine bottom-tip, hub height and top-tip, respectively, providing three components of wind velocity and temperature at 20 Hz for each location. Six additional instrumented arms (at z = 7, 27, 55, 77, 105, 126 m) are equipped with low frequency (1Hz) temperature, relative humidity and cup and vane anemometer sensors, see Figure 4.2. One additional CSAT3 is positioned at z =10 m for boundary layer parametrization and assessment of thermal stability conditions. Barometric pressure for the site is recorded at the z =7 m boom.

WindCube lidar

A WindCube V1 wind profiling lidar, manufactured by LeoSphere, is used herein to provide a time-resolved description (1Hz) of the incoming velocity profile to the turbine, with z ranging from 40 to 160 m. Wind speed and direction information is captured, stored every second onto an internal hard drive and synchronized with the unique time stamp of the Eolos database systems through a local network connection. The WindCube V1 estimates the air velocity along four line of sight (LOS) measurements oriented 90 degrees from one another in the horizontal plane and inclined at an angle of $\phi = 27.8$ degrees from vertical (known as the cone angle). The LOS directions with respect to a fixed reference system are determined by the WindCube specific orientation. In this study, two different WindCube alignments were tested: (i) adopting the standard orientation which points the lidar due north (defined here as global alignment along the cardinal directions and utilizing all four LOS measurements to calculate the three components of velocity); (ii) directing the north-south LOS plane to be perpendicular to the turbine rotor plane (denoted as local alignment, and can use the two LOS along the mean wind direction to measure the velocity in that plane). Three methods of calculating the velocity components from the lidar measurements can be utilized, and are: (i) use all four LOS measurements to calculate the spatially averaged velocity (intrinsic procedure for pulsed lidar software to resolve u, v, w); (ii) use two LOS measurements

180 degrees from one another to get averaged planar velocity (two components only); (iii) use one LOS measurement in addition to the vertical velocity w calculated from the four beam average (allows estimation of LOS local planar velocity). Here, method (i) is employed for data taken in global lidar orientation and (iii) for data acquired in local lidar alignment. The two calculations are introduced in more detail below.

Standard method for lidar velocity calculation

The lidar software implements the following procedure to estimate the three components of velocity using all four velocity measurements along the LOS (see Equations 4.1-4.3). Note that regardless of the lidar orientation this standard method of velocity calculation is utilized and synchronized to the turbine operational data to allow correct joint statistics. The four LOS method allows the lidar to remain in a fixed location yet capture the wind direction changes that inevitably cause the turbine to yaw away from the initial alignment with the lidar.

$$u = \frac{RWS_N - RWS_S}{2sin\phi}; \tag{4.1}$$

$$v = \frac{RWS_E - RWS_W}{2sin\phi}; \tag{4.2}$$

$$w = \frac{RWS_N + RWS_S + RWS_E + RWS_W}{4cos\phi}; \tag{4.3}$$

where, u, v and w are the velocity components in the x, y and z directions, while RWS_N, RWS_S, RWS_E and RWS_W stand for the radial wind speed (RWS) along the LOS in the north, south, east and west directions, respectively.

Quasi 2D method for lidar velocity calculation

The second method uses Equation 4.3 from method (i) in addition to Equations 4.4 and 4.5 and computes the instantaneous velocity component along the mean wind direction using the measured RWS and the spatially averaged mean vertical velocity.

$$M = \frac{w}{sin\alpha} = \frac{RWS_{LOS}}{cos\beta}; \tag{4.4}$$

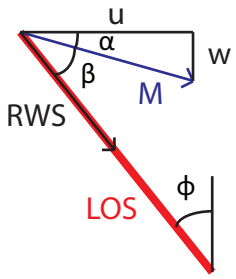

Figure 4.3: Geometry used to calculate the horizontal, in-plane velocity u from the lidar measured radial wind speed (RWS) and the vertical velocity w, as computed from Equation 4.3. The line of site (LOS) beam is emitted from the lidar (lidar located at the base of LOS) and represents one of the beams emitted from the lidar.

$$u_{LOS} = \frac{w}{tan\alpha}; \tag{4.5}$$

where, M is the in-plane wind vector containing the u and w components of velocity (streamwise, vertical), α is the angle between the horizontal plane and the wind vector M, and β is defined as the angle between the LOS beams and the wind vector M. A schematic of the measurement is shown in Figure 4.3. Note that to calculate the streamwise velocity profile for this method, spatial averaging is performed only on the plane aligned with the mean wind direction; thus, contamination is minimized from the spanwise velocity measured along the two LOS perpendicular to the mean wind (not necessarily confined within the rotor area, and may be altered by the spanwise flow distortion due to the turbine). This method for obtaining the velocity is utilized for determining the mean profile immediately upwind of the turbine and in the turbine wake.

4.2.2 Description of the field measurements

Several field measurements with lidar deployments were conducted in the late summer, early fall of 2012 and 2013 to probe the incoming flow and wake profiles for the Eolos wind turbine. A brief summary of the experimental conditions is given in Table 4.1. The first experiments conducted in 2012 deployed the lidar at various distances upwind of the turbine following the global alignment orientation. During the summer of 2013, the lidar was oriented along the wind direction (local alignment) such that two of the four

beams defined a measurement plane perpendicular to the rotor plane, consistent with the laser sheet employed for PIV measurements in the wind tunnel. When selecting the measurement location (specifically, the distance from the turbine along the wind direction), given our lidar half angle of 27.8 degrees, we were limited by the occurrence of blade-lidar beam interference; the shortest distance between the lidar and the turbine rotor plane for non-interaction was 68 m ($x/D = 0.71$).

Table 4.1: Meteorological conditions for the specific lidar measurements used herein. Positive lidar positions indicate upwind flow measurements, negative values indicate wake measurements.

Run	Date	Lidar Position (+ UW) [m]	Start Time CDT	U_{hub} [ms^{-1}]	Thermal Stability $\zeta = z/L$	Duration [hr]	Mean Wind Direction
1	16 Aug. 2012	68.5	16:34	7.8	-0.29	2	NW
2	16 Aug. 2012	97.5	19:13	6.8	0.31	1	NW
3	9 Aug. 2013	61.8	14:14	6.0	-0.63	1.5	NW
4	9 Aug. 2013	76.8	16:00	5.4	-0.56	2	NW
5	9 Oct. 2013	-142	12:48	6.5	-3.46	1	S
6	9 Oct. 2013	-240	16:14	7.3	-0.24	1	S
7	9 Oct. 2013	-288	14:45	7.9	-0.13	1	S

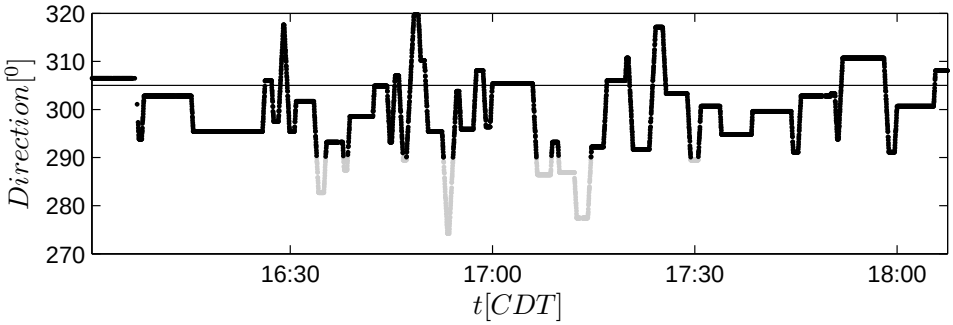

Figure 4.4: Eolos turbine nacelle heading from run 4. The black dots correspond to the measurement conditions satisfying the selected alignment window, while the gray dots indicates where the nacelle heading lies outside of the prescribed alignment. The solid horizontal line defines the lidar location with respect to the turbine and the time stamps correspond to the local time.

Unlike miniature turbines used in wind tunnel testing, the 2.5 MW Eolos turbine continuously adjusts specific parameters to produce the optimum power given the wind conditions and operating region. Among those, one key variable is the nacelle heading direction, which continually adjusts to the wind direction. The mean upwind velocity profiles presented herein were averaged over time periods when the turbine nacelle direction was within $\pm 15^o$ of the lidar-turbine tower direction. Figure 4.4 displays the nacelle orientation during run 4 and the sampling points contributing to averaged mean velocity profile. The lidar position is shown with the solid horizontal line.

Thermal stability is known to play a key role when gathering data in the atmospheric boundary layer due to its ability to alter turbulence intensities and the shape of the boundary layer profile (in particular, the mean shear). Studies in the SAFL atmospheric wind tunnel have shown that even a weak thermal stability regime has an impact in the wake flow (Chamorro and Porté-Agel 2010 [83], Zhang et al. 2013 [43], Howard et al. 2013 [1]). Field measurements have shown that thermal stability adjusts momentum transfer ([84]), turbulence interaction ([85]) and the size and orientation of the large-scale structures within the boundary layer ([65],[62]), which have a direct impact on wind turbine performance ([58]).

In this work, thermal stability was assessed through the Monin-Obukhov ratio ($\zeta =$

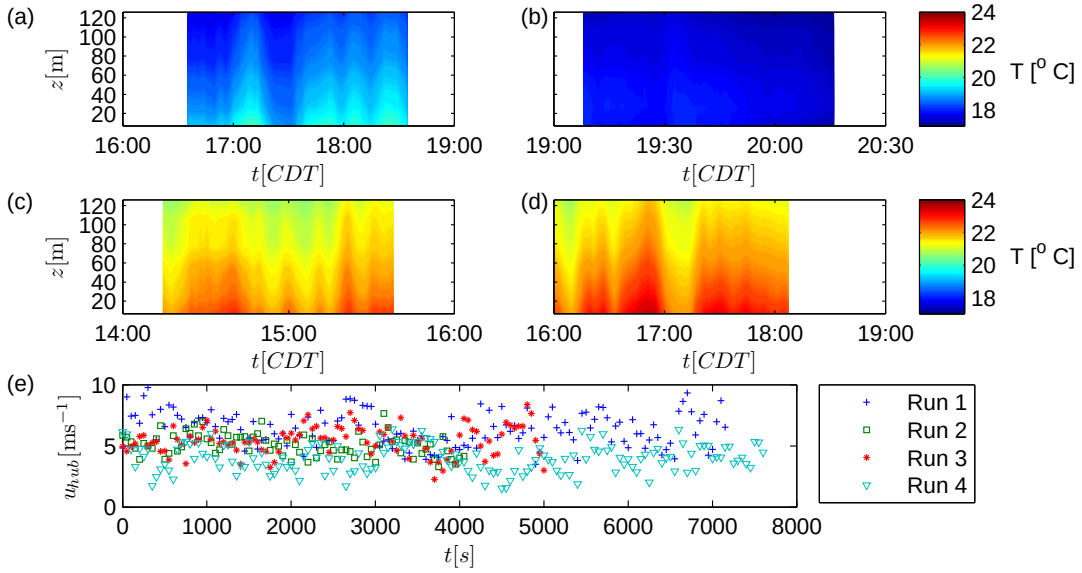

Figure 4.5: Temperature contours from the met tower as a function of local time and elevation z for (a) run 1, (b) run 2, (c) run 3 and (d) run 4. (e) The hub velocity taken from the sonic anemometer on the met tower is plotted to show the consistency of the mean velocity for each run. The time stamps correspond to the local time.

z/L), calculated using velocity and temperature high frequency measurements from the met tower. Here z was taken as the lowest sonic anemometer location at $z = 10$ m, and L is the Monin-Obukhov length, defined as: $L = \left(-u_*^3\overline{\theta_v}\right)/\kappa g(\overline{w\prime\theta\prime_v})_s$, where u_* is the shear velocity calculated by fitting a curve to the log-law corrected for stability by the phi function, $\overline{\theta_v}$ is the average virtual potential temperature, κ is the von Kármán constant, g is the gravitational constant and $(\overline{w\prime\theta\prime_v})_s$ is the virtual potential heat flux at the surface (precisely, at $z = 10$ m). The Obukhov length is interpreted as the height at which the turbulent kinetic energy (TKE) produced by buoyancy is equal to that produced by shear. Therefore for $|z/L| < 1$ we can assume that mechanical production of turbulence is dominant and boundary layer parametrization is acceptable.

Meteorological conditions were continuously varying throughout the duration of the runs. Velocity measurements for the upwind profile analysis have been hand picked from a larger data set to avoid major drift in direction and magnitude of the wind velocity over time (see Figure 4.5e). For each of the selected runs, the sun was continually changing

inclination and thus modified the surface heating throughout each test; the temperature and vertical velocity time histories were therefore linearly detrended before calculating the vertical heat flux $\overline{w\prime\theta\prime_v}$ and the Reynolds stresses $-\overline{u\prime w\prime}$ contributing to the estimate of z/L. In Figure 4.5(a) through (d), the temperature contour plots are shown for each of the runs described here. Note that, even though the largest difference between runs 1, 3 and 4 is the average temperature, these periods share the same thermal stability condition: z/L <0 denotes a convective boundary layer as expected for mid afternoon in summer and the contours display warmer temperatures towards the ground. Note also that even if run 2 is classified in the weak stable stratification regime (z/L>0) , the temperature profile was not observed to vary significantly (as expected just after sunset).

Wake measurements for the Eolos wind turbine were completed on a separate day in which the mean wind direction was from the south. The met tower, given its fixed placement due south of the turbine, measured the inflow conditions 160 m upwind of the turbine and the lidar was placed in local orientation, velocity calculation method (iii), at several downwind locations to capture the wake evolution. The mean wake velocity profiles from the utility-scale turbine are used here to understand the differences in wake development between the model wind turbine and the full-scale. Potential agreement between normalized wake profiles would allow the model turbines to be arranged in complex configuration (i.e. within a wind farm) that cannot be arranged at the field site, to evaluate the best locations for upwind preview measurements. It should be noted that turbine wake measurements were successfully captured by lidar in previous studies ([86], [87]).

4.2.3 Wind tunnel measurements

The laboratory scale experiments were conducted in the SAFL atmospheric boundary layer closed loop wind-tunnel at the University of Minnesota. The test section has a length of 16 m with a cross-section of 1.7 m by 1.7 m. The flow is conditioned by coarse wire mesh and a honeycomb flow straightener before entering a 6.6:1 aspect ratio contraction, located just upwind of the main test section. A 0.040 m picket fence trip was placed at the leading edge of the test section to promote boundary layer growth, and the resulting boundary layer height was $\sim$ 0.6 m at the turbine location. The flow develops

over a smooth floor surface made up of aluminum plates that can be heated or cooled to maintain a desired thermal stability condition. In the neutral regime experiments described here, the thermal system of the wind tunnel was able to hold the freestream air and the surface temperatures to within $\pm 0.2^{\circ}$C.

Miniature turbine and voltage generation

The scale-model wind turbine used in this study has a three-blade GWS/EP-5030x3 rotor (blade profiles are nearly flat) with a diameter of 0.128 m and a hub height of 0.104 m. Specific rotor geometry can be found in Howard et al. [58]. The turbine geometry and upwind flow conditioning ensure that the device is located within the lowest twenty-five percent of the boundary layer, which is typical for utility-scale turbines in the atmospheric boundary layer.

The tip-speed ratio for the model turbine was $\lambda \approx 4.5$, which is smaller than the optimal tip-speed ratio of the Eolos turbine ($\lambda \approx 8.5$) but within typical values for full-scale wind turbines, ranging between $\lambda \approx 3.5$ and 10. Upwind experiments were conducted keeping the mean velocity at hub height at the constant value of U_{hub} =5.0 ms^{-1}. The Reynolds number based on the rotor diameter and boundary layer height are $Re_D = U_{hub}D/\nu = 4.310^4$ and $Re_\delta = U_\infty \delta/\nu = 2.210^5$, respectively. Wake measurements were completed at U_{hub} =7.2 ms^{-1} resulting in $Re_D = 6.110^4$.

The test turbine generated voltage through a DC generator directly connected to the turbine rotor shaft. The peak power coefficient for this rotor-turbine configuration is 0.17 at $\lambda \approx 2.9$ [58]. The voltage signal was validated through a set of experiments described in [58] and found to be (i) linearly proportional to the angular velocity of the turbine rotor and (ii) able to track the change in the rotor kinematics due to the large scale structure of turbulence or other upwind perturbations.

Flow measurement devices

A TSI PIV system was employed to capture detailed information on the flow field upstream of the turbine model. The PIV system uses the TSI Insight 4G software coupled with a TSI synchronizer, which controlled the timing between the Big Sky dual-head Nd:YAG Laser and a 2048 pixel x 2048 pixel CCD PowerView Plus camera. The 532 nm YAG laser was used to illuminate olive oil seeding particles injected into

the flow using a set of Laskin nozzles and a seeding chamber below the tunnel floor. The sampling frequency for the PIV system was 7.25 Hz. The laser optics and cameras were positioned to allow (i) the closest possible field of view to the rotor covering approximately 1.5D upstream of the turbine and (ii) the estimate of turbulent flow structures impinging on the the turbine rotor and influencing its angular velocity [see Figure 4.8(a) for example of upwind field captured].

Wake measurements behind the model wind turbine were completed using a two component hotwire anemometer, commonly referred to as a crosswire anemometer. The hotwire was placed on a traverse system to take successive vertical profiles at the multiple downwind distances on the centerline of the turbine. Each profile contained 23 points where data was gathered at 10000 Hz for 120 seconds. For more details on the hotwire setup and acquisition the reader is directed to [58],[66].

4.3 Results and Discussion

4.3.1 Incoming Flow Profiles

The conditions monitored during the field measurements included wind direction and speed, thermal stability condition, lidar upwind distance and orientation, and turbine SCADA data. The only variables inspected in detail with regards to incoming profile distortion, however, are the lidar-turbine spacing and the lidar orientation, (i) global, lidar LOS aligned with cardinal directions, versus (ii) local, two LOS aligned with mean wind.

All of the full-scale velocity profiles presented below are normalized by the turbine hub velocity, as measured by the sonic anemometer located on top of the turbine nacelle. First, the orientation of the lidar has a noticeable impact on the mean velocity profile (see Figure 4.6 for run 1 versus run 3). For the local alignment, when the north and south LOS measurements are aligned with the turbine centerline, the profile is found to have a greater reduction of mean velocity around the hub height, which is less apparent when the lidar is globally aligned and the incoming velocity profile thus has contributions from the velocity along the LOS measurements directed outside of the turbine influenced area.

A comparative analysis between the lidar run 4 measurements at $x/D = 0.80$ ($x =$

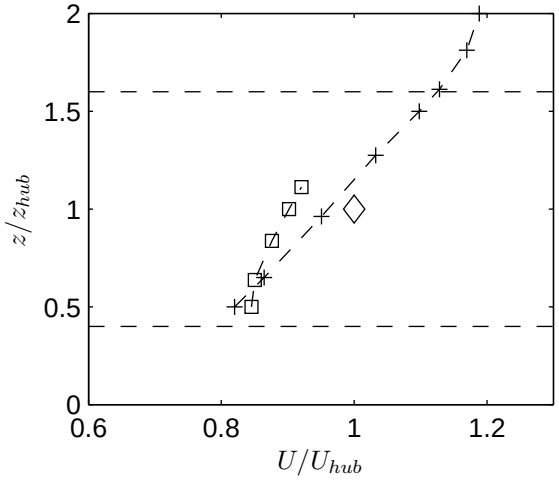

Figure 4.6: Comparison of lidar orientation on upwind mean velocity profile. Local lidar alignment shown as □ at a distance x/D of 0.64 and global lidar alignment shown as + at a distance x/D of 0.71. The normalizing mean velocity U_{hub} is measured by the sonic anemometer on the turbine nacelle (◊).

$76.8m$) and the met tower measurements is conducted to confirm the curvature change between the incoming wind profile and the undisturbed inflow. Figure 4.7(a) displays the upwind profile along side the cup (◁) and sonic (x) anemometers from the met tower. Given the the mean wind direction from northwest, and the location of the met tower (160 m south of the turbine), we can safely assume that the met tower wind measurements are undisturbed. The prominent difference in the two curves is indeed the change in curvature. The convex velocity profile from the lidar measurements points specifically to the mean flow distortion exerted by the blockage on the turbine frontal area, to which both the static turbine components (tower and nacelle) and rotor solidity, contribute. Such effect is confirmed in Figure 4.7(b) where both profiles exhibit the concavity change with a consistent reduction in mean streamwise velocity as the lidar (in local orientation) is moved closer to the turbine.

Wind tunnel data obtained by PIV in a plane centered on the miniature turbine hub [Figure 4.8(a)] also show a specific concavity consistent with field measurements, and opposite to the one observed in canonical boundary layer profile, thus pointing at

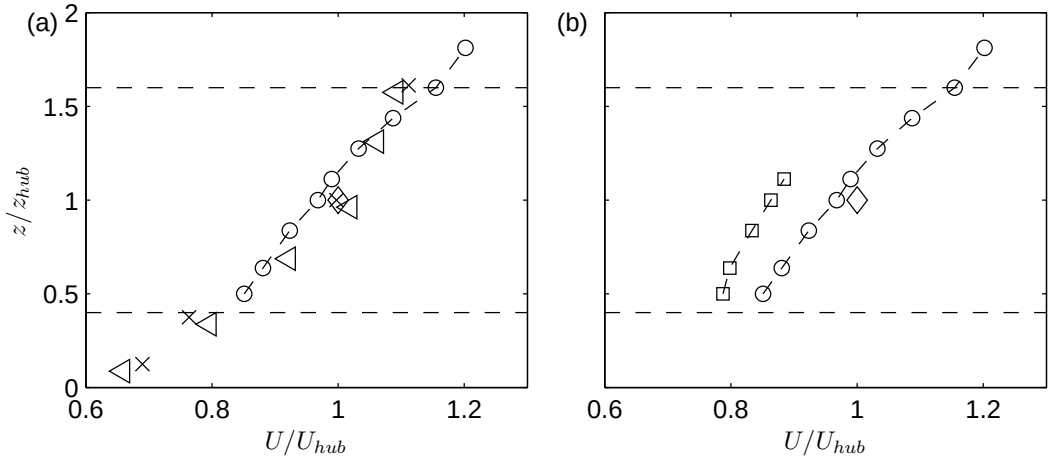

Figure 4.7: (a) Velocity profile comparison between the lidar upwind from run 4 (∘) and the undisturbed boundary layer, given by the met tower sonics (x) and met tower cups (◁). (b) Comparisons of upwind mean velocity profile: lidar distances at x/D of 0.64 (□) and x/D of 0.80 (∘) with wind from the NW (runs 3 and 4 from Table 4.1). The normalizing mean velocity U_{hub} is measured by the sonic anemometer on the turbine nacelle (shown as a ◊).

a distinct feature of the very-local incoming wind profile for wind turbines. The PIV sampled velocity profile presents a velocity reduction at $x/D = 0.80$ [Figure 4.8(b)] of 4.7%, as compared to $\sim 4\%$ for the Eolos turbine. Here, the vertical velocity profile from PIV is calculated with a spatial average consistent with the aligned method used in the lidar processing and with the LOS beam geometry, see Figure 4.8(a). The robustness of the mean velocity measured by lidar are summarized in a review by Mikkelsen [88], who provides an estimation for the error induced by the WindCube lidar averaging volume of less than 0.5% at an elevation of 80 m, an error which reduces with increased height. Therefore, the good agreement between the field and laboratory experimental findings remains even when considering the lidar and PIV measurement errors, confirming the strength of our result. The small discrepancy between the two upwind flows can be due to observed differences in the mean shear upwind of the the full- and model-scales, specific turbine geometry and operating conditions (tip-speed ratio, power coefficient). These factors will also have a minor impact on the turbine induced velocity reduction

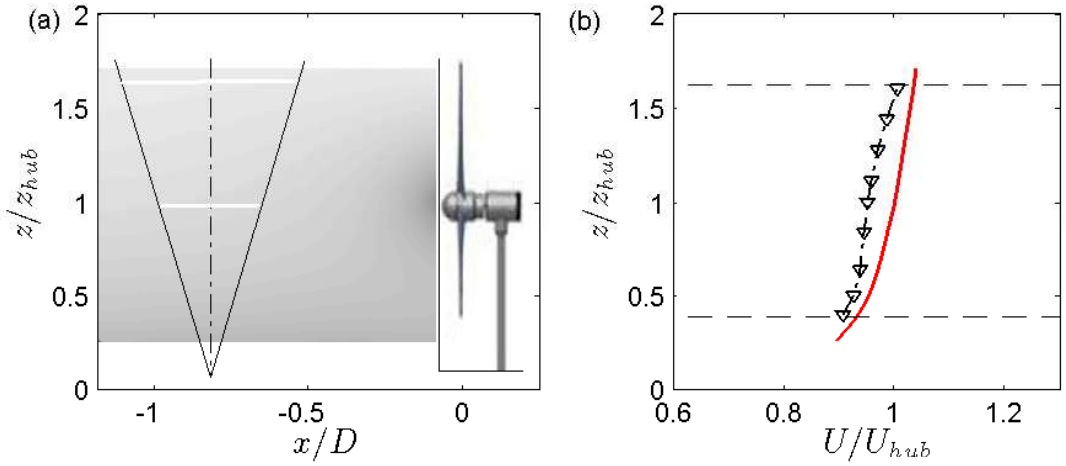

Figure 4.8: (a) PIV measurement of the mean velocity field upwind of the turbine model. (b) Comparison between the mean velocity profile $x/D = 0.8$ upwind of the model turbine obtained by a spatial averaging consistent with the lidar field measurements ($\triangledown$), and the baseflow profile (no turbine, shown with the solid red curve).

at larger radial distances from the hub, upwind of the rotor, or to the velocity deficit in the turbine near wake.

Our findings at the full- and wind tunnel-scale qualitatively and quantitatively confirm the turbine blockage effects shown in previous studies ([89], [1]). Here we point out that in run 3 ($x/D = 0.64$), the alignment of the LOS beams with the turbine centerline caused measurements obtained at elevations above $z/z_{hub} = 1.2$ to be contaminated by the rotating blades and were therefore dismissed. Also for clarification, the finding that the hub velocity measured by the turbine is higher than those in the undisturbed boundary layer profiles is likely due to the location of the sonic, mounted on top of the nacelle (on the downwind side) which thus tracks the slight velocity acceleration around the nacelle body. In addition, we note that the lidar mean velocity profile tracks an acceleration region nearing the top-tip elevation ($z/z_{hub} = 1.6$), above which the profile switches to a concave curvature, as in the undisturbed boundary layer.

4.3.2 Turbine Response

The analysis is now shifted toward tracking the response of the turbine to temporal variation of the instantaneous incoming velocity (i.e. wind gusts). Specifically, we focus on the cross-correlation between the time history of turbine-specific variables (power/voltage output and blade strain) and that of the instantaneous streamwise velocity at each elevation sampled within the rotor swept area. Figure 4.9(a) shows the timeseries of two velocities (at hub and top-tip locations), turbine power output and blade strain from the root on the high pressure side from a selected run among the full-scale experiments. A visual inspection of Figure 4.9(a) reveals that the blade strain (black dots) follows the power time-history signal (magenta line) closely, with a negligible lag. Note that near the peaks in the power timeseries, velocity fluctuations are also observed [see close up view in Figure 4.9(b)]. These similarities in the time signals allude to the obvious conclusion that the wind turbine feels the changes in wind conditions and displays the signature of large turbulent fluctuations in the SCADA data.

Figure 4.9(b) provides a short time window focused on a particular wind event, a gust occurring at 18:00 CDT as reported by the lidar velocity at hub height (blue dashed line), though surprisingly not at the top-tip elevation (red dashed line). The blade strain (black dots), exhibits a local maximum with a slight delay (on the order of a few seconds) from 18:00 CDT corresponding to the initial flexing of the blade out of the rotor plane as it responds to the wind gust. Immediately after this peak ($\sim$ half the turbine frequency or 2.7 seconds later) a local blade strain minimum occurs, which results from an aeroelastic effect as the high pressure blade surface responds to the blade bending back into the rotor plane due to the mechanical properties of the blade's composite construction.

During the next minute between 18:00:00 CDT and 18:01:00 CDT, the wind at both elevations drops back down to pre-gust levels and remains relatively constant while the power time history shows a peak just after 18:00:30 CDT. This power peak is attributed to the torque increase from the wind gust. The combined inertia of the rotor and drivetrain impose a finite time delay before the turbine operation and control registers a change in the rotor angular velocity; therefore, only after a significant delay from the gust response of the blade, the torque (indicated as reactive power), rotor angular velocity and blade pitch are observed to gently vary as prescribed by the turbine control

system. The mean blade strain is also observed to increase and decrease following the instantaneous power on this relatively slow time scale ($\sim$ 1 minute), consistent with the variation in pitch and angular velocity due to the resulting aerodynamic forces.

Statistical representation of power-velocity correlations: field-scale

As both the instantaneous power and blade strain were observed to reasonably follow the incoming velocity temporal fluctuations, we can imagine to use the latter to predict (or as a control input for) wind turbine performance and blade structural loads. The statistical tool chosen to confirm the trends outlined in Figure 4.9 is the cross-correlation function, in the time domain, between the simultaneously sampled time histories of the instantaneous power $P(t)$ and streamwise flow velocity $u(z,t)$ estimated by the lidar. Temporal cross-correlation coefficients $\rho_{Pu}(z,\tau)$, ranging from 0 to 1 as they are normalized by the product of the respective standard deviations, are shown in Figure 4.10(a). The $\rho_{Pu}(z,\tau)$ curves have a peak at a time lag τ which depends on the delay between wind gusts and the turbine response (due to the turbine rotor inertia, operational control as well as on the z-dependent mean convection velocity), and a peak magnitude which measures the similarity between the two timeseries. The identified peak values in the time lag phase space are then plotted as a function of the measurement height, leading to the curve $\rho_{Pu_{max}}(z)$ shown in Figure 4.10(b). This provides a clear indication of where (in elevation) the velocity is predominantly correlated to the turbine power and thus where an instrument sensing the flow would optimally gather data to serve as an input for the turbine control. Specifically, the difference in peak correlation spreads from roughly $\rho_{Pu} \approx 0.5$ to 0.8, with the maximum value located at about $z/z_{hub} \approx 1.3$ (corresponding to $z = z_{hub} + D/4$), thus significantly higher than hub height. From a physical perspective, it is reasonable that the peak occurs in the upper half of the rotor (where the wind is stronger, providing both greater lift and torque contributions) away from the tip (where the blades have a very small residence time) and away from the hub height (where no lift is produced, even though it roughly provides the average velocity across the rotor).

Also shown in Figure 4.10(b) is the peak value of the cross-correlation between the turbine power and the rotor-averaged velocity (spatially, not temporally averaged). This value is higher than the peak value of the individual elevation signals because the

spatially averaged velocity time signal (i) takes into account the wind influencing the blades throughout the full rotor swept area and (ii) reduces the influence of intermittent, local, gusts at very specific elevations.

The power-velocity cross-correlations are presented in Figure 4.11(a) for varying lidar upwind locations to ensure that the peak cross-correlation profile shown in Figure 4.10(b) is a statistically robust feature. $\rho_{Pu_{max}}(z)$ curves are shown for $x/D = 0.71$ and $x/D = 1.02$, from runs 1 and 2, respectively, where the lidar was in global alignment. The peak above hub height is persistently observed, though shifted towards reduced correlation values (on average), as expected when the lidar is moved away from the turbine (from $\Diamond$ to $\triangle$ profiles). Indeed, the wind must travel a larger distance before reaching the rotor, during which turbulent processes modify the instantaneous velocity before it impacts the blades and influence the power timeseries. A reduction in peak correlation with increasing upwind distance x/D is also observed when using the rotor-averaged velocity signal.

The time signals presented in Figure 4.9 show that the strain on the high pressure side of the blade root ϵ also feels the variations of the incoming velocity, suggesting to test the strain-velocity correlation $\rho_{\epsilon u}(z, \tau)$ as well. Figure 4.11(b) displays the blade strain to velocity correlation peak profiles $\rho_{\epsilon u_{max}}(z)$ estimated at the root and at 37.5% of the blade length. Again, the peak cross-correlation value occurs at $z/z_{hub} \approx 1.3$, though with a reduced value ($\rho_{\epsilon U} \approx 0.675$ versus $\rho_{PU} \approx 0.8$). The rotor averaged velocity signal, similar to power-velocity case, confirms the same elevation to be the most representative input option also for blade deformation. This statistical analysis stresses the importance of upwind measurements for turbine control and operation, but also that, in the absence of rotor-averaged velocity, a single point measurement of $u(z/z_{hub} \approx 1.3, t)$ would be almost as useful and likely more affordable to implement.

Statistical representation of voltage-velocity correlations: wind tunnel scale

There are two reasons to obtain power-velocity cross-correlation statistics using the miniature turbine models in the SAFl wind tunnel: first, we want to make sure that the profile of the power to velocity cross-correlation is not related to instrument-specific spatial averaging performed by the lidar; second, we hope to explore a variety of inflow conditions that cannot be implemented at the Eolos research field station, as for instance

the case of multiple interacting turbines. The question behind the next set of tests is indeed on the representativeness of the $u(z/z_{hub} \approx 1.3, t)$ location when the reference turbine is in a multi-unit wind power plant. This said, there are a few limitations to scale-model testing that need to be acknowledged: (i) the model turbine does not have a control strategy and does not operate at peak efficiency, however, the DC voltage produced is representative of the true production as it tracks the variation in angular velocity for an approximately constant generator torque [58]; (ii) as an attribute of the PIV measuring system, the incoming velocity is adequately resolved in space (x, z), though, poorly resolved in time (7.25 frame rate). The correct time stamp for the incoming velocity (from PIV) was provided through simultaneous acquisition of the Q-switch TTL signal triggering the first laser pulse for the PIV with the miniature turbine voltage.

Each run consisted of 30 seconds of synchronized measurements of voltage timeseries (sampled at 10kHz) and 110 PIV vector fields. A total of 18 repeated PIV-voltage runs were performed equating to a sum of 540 seconds in voltage timeseries and 1980 PIV realizations, which ensured the convergence of the voltage and velocity statistics. Each PIV vector field represents a snapshot of the incoming flow to the turbine model that can be reduced into a x-averaged profile obtained at a known time (again from the laser pulse timeseries), specifically $u(z, t)$. The x-axis averaged velocity was calculated using two different methods to inspect the reliability of the spatial averaging utilized by the lidar: first, an average over a fixed Δx for each height z; second, an average within the lidar-specific half angle [triangle shown in Figure 4.8(a), producing a different x averaging-interval at each height z].

The timeseries from the individual acquisitions, small window time length corresponding to about 10 times the largest turbulent boundary layer structure evolving in the wind tunnel test section, produce 110 voltage-velocity pairs $u(z, t), V(t)$, with which to calculate a cross-correlation function. The turbine voltage is low pass filtered (based on [58]) and resampled at the PIV capture rate. The peak cross-correlation value is then ensemble averaged for each height z over the 18 runs, leading to the $\rho_{Vu_{max}}(z)$ profile. First we inspect the averaging method of the lidar ($\triangledown$) in comparison to a fixed x-distance average (solid line) using nearly the entire horizontal distance of the PIV

field, shown in Figure 4.12(a). We exploit the full vertical resolution of the PIV measurements showing that a core region around hub height, $z/z_{hub} = 0.8 - -1.3$ is fairly representative when using a lidar-cone angle spatial averaging. However, when using the full window spatial average, which provides a more robust estimate of large scale velocity, the correlation peak remains above hub height, $z/z_{hub} \approx 1.2$, indicating that lidar-cone averaging leads to a reduced height of the cross-correlation maximum. This suggests that the correlation peak at $z/z_{hub} \approx 1.3$ computed with field scale data may even be slightly underpredicted.

The model-scale peak cross-correlation profile, even with low-temporal resolution, is qualitatively comparable with the one obtained at the Eolos field, as shown in Figure 4.12(b). Although the turbine responds to large scale fluctuations of the incoming velocity field, which are still observed to vary in the reduced frequency voltage-velocity series, the reduction in the magnitude of the correlation, as compared to field data, is in fact due to the inability of the cross-correlation to pick up rapid changes in voltage corresponding to quick fluctuations in the streamwise velocity. A difference to point out, besides the peak magnitude, is the sharp reduction in correlation above hub height for the wind tunnel case. Here the important factor to consider is the mean shear over the rotor [compare $\triangleleft$ in Figure 4.7(a) to the solid curve in Figure 4.8(b)]. The higher shear observed at the field-scale equates to more torque produced in the upper portion of the rotor $z > z_{hub}$, due to significant increase in velocity, which ultimately contributes to shifting peak correlation toward higher elevations.

Voltage-velocity correlations for turbine-turbine configurations

Along with the single turbine case, the case of two streamwise aligned turbines was investigated in the wind tunnel with the same PIV setup by adding a second model turbine upwind of the voltage producing unit. First, to ensure the validity of the model turbine wake characteristics, we compare the mean wake profiles from both the Eolos turbine, measured with the lidar, and the model turbine, acquired with a hotwire anemometer. Figure 4.13 displays the wake profiles for three downwind distances with the inflow boundary layer profile (U_{in}) removed. Again, U_{in} for the Eolos turbine was measured by the met tower (wind from the south meant the met tower was directly upwind of the turbine) and U_{in} for the model was measured by PIV for the baseflow

condition (no turbines). In the near wake ($x/D < 3$), the profiles share similar shapes, however, the overall deficit and location of maximum deficit are different. Note that i) the velocity deficit profile at the closest turbine location in the field was obtained at noon, in highly convective conditions, and ii) the incoming flow profile was estimated using a power law fitted to sonics and cups averaged values for each period of time where lidar was operating (runs 5,6,7); both arguments may explain the vertical shift in the velocity minimum. Other potential sources for the deviation between the two profiles can be the specific geometry of the two turbines and the specific load with which the turbines are operating. The miniature turbine has very little load (see [58]) and therefore it does not remove a significant amount of energy from the flow, as compared to the Eolos turbine. However, as the wake profiles are measured farther away, the full- and model-scale wakes begin to collapse; thus we assume that the model wake is representative at downwind distances greater than $3D$. PIV measurements with a second turbine $6D$ upwind of the test model turbine resulted in the correlation curve shown in Figure 4.14, which is thus deemed representative for turbine interaction within a wind farm. In this case the correlation peak is shifted towards the hub height, which is consistent with the lower mean velocity gradient in the rotor area observed in the far wake of the turbine model and the homogeneization of the flow in the wake (see [66]).

Note that the dependency of the most representative elevation, according to the $\rho_{Vu_{max}}(z)$ peak value, on the mean shear of the flow impacting the rotor was further confirmed by wind tunnel tests in the weakly stratified and convective regimes (not shown here); we infer that in wind power plants, where the signature of the incoming boundary layer is essentially lost through the wake of the upwind turbines and the mean shear is thus reduced, we expect the most representative height for upwind preview to approach hub height. We must acknowledge that blade strain values cannot be estimated at the miniature turbine scale.

4.4 Conclusions

Full-scale lidar measurements in proximity to a 2.5 MW wind turbine and wind tunnel experiments were used to investigate how the monitoring of inflow conditions may help to predict wind turbine performance for various inflow conditions. The synchronization

of the turbine SCADA data, blade sensors, micro-meteorological information and lidar data gathered at the Eolos wind energy research station is at the core of this experimental study; it enables the quantification of the turbine blockage effect on the incoming mean velocity profile, and allows the tracking of the turbine response to wind temporal variations. Statistical results on the turbine response to wind variations are reported in the form of temporal cross-correlation between the instantaneous streamwise velocity, at specific elevations, turbine power and blade strain. Wind tunnel tests confirm the results obtained in the field and prove the robustness of the power-incoming velocity peak correlation feature over a Reynolds number $Re_D = U_{hub}D/\nu$ range spanning nearly three orders of magnitude. PIV results from the wind tunnel also, (i) ruled out the possibility that statistical artifacts were created by the spatial averaging procedure embedded in the velocity estimate by the lidar and (ii) open up the possibility to study more complex turbine arrangements using miniature turbine models. Important conclusions from this study are:

- A single wind turbine exerts a blockage effect on the upwind mean velocity profile, in the proximity of the rotor, responsible for a bluff body-like distortion of the flow field. The upwind velocity deficit (blockage induced), inferred to weakly depend on specific turbine geometry and tip-speed ratio, was observed to increase as the upwind profile approaches the rotor plane ($x/D = 0$), with a maximum observed reduction of approximately 15% at hub height for a lidar(ground based)-turbine distance of $x/D = 0.64$.

- The turbine power and blade strain carry the temporal signature of wind gusts, implying that the incoming wind velocity can be used for both power prediction and mitigating unsteady loads. Temporal cross-correlation between turbine power and upwind velocity time signals at multiple elevations revealed that the turbine power is most correlated to the velocity time signal captured at $z/z_{hub} \approx 1.3$, corresponding to $z \approx z_{hub} + D/4$ (with D indicating the rotor diameter).

- The peak correlation value is observed to (i) decrease with increasing distance between the turbine and the measurement location, and (ii) is largest if the representative incoming velocity is spatially averaged across the rotor plane. These

findings suggest that either spatially averaged or fixed point upwind measurements can be efficiently used as input data for turbine control operations.

- The peak cross-correlation profile [initially provided in Figure 4.10(b)] is observed at various upwind distances, for different thermal stability regimes for both the field and the wind tunnel scale and for the blade strain to velocity correlation at full-scale. It is thus a robust feature of joint flow-turbine statistics observed for utility-scale devices in the atmospheric boundary layer as well as for miniature turbine models in wind tunnel experiments.

- In the case of two aligned turbines (wind tunnel only), the peak power-velocity cross-correlation is observed to move closer to hub height, consistent with the reduced mean shear of the incoming flow and the greater vertical homogenization of the structure of turbulence observed in the wake of the upwind turbine (see Singh et al. [66]).

Insight into general turbine operation under variable conditions is presented by these findings, in addition to detailed flow and measurement location information useful for the wind turbine controls community. The peak power-velocity correlation profiles highlight a precise elevation where sampled wind velocities have the greatest influence on the turbine power and blade loads.

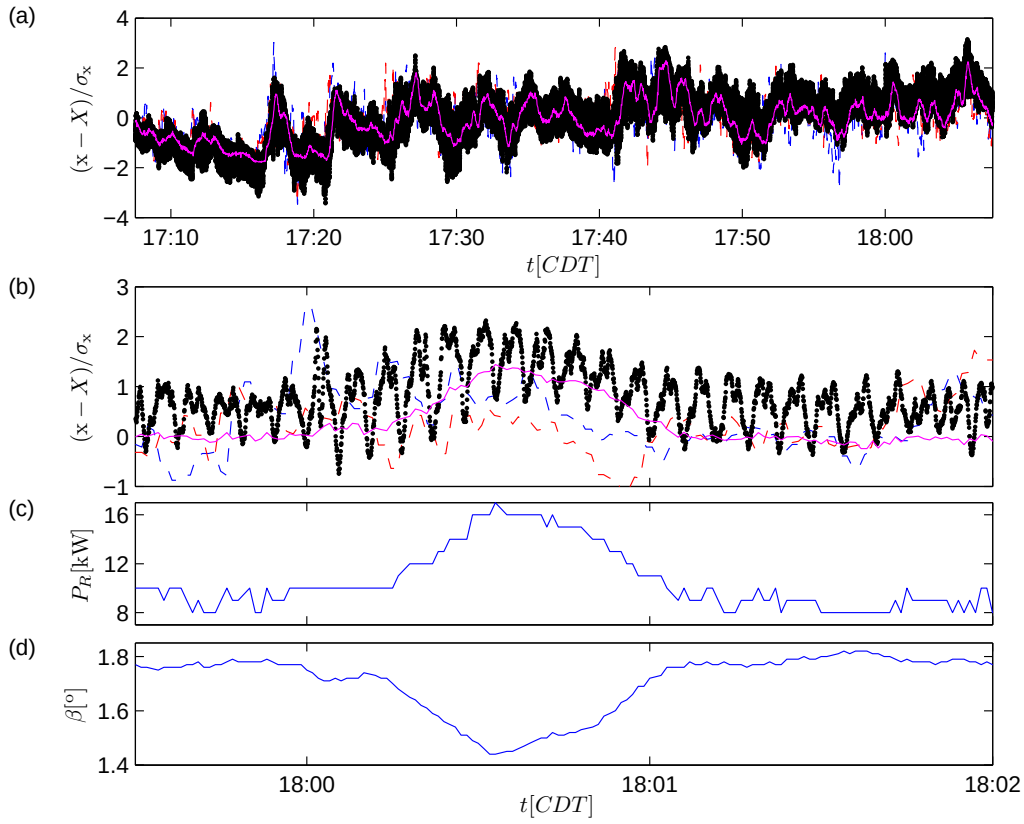

Figure 4.9: (a) Time signal comparison between the power (magenta line), blade strain on the high pressure surface at the root (black dots) and two velocities at different elevations (blue is hub velocity from the lidar, red is velocity at top-tip $z/z_{hub} = 1.6$ from the lidar). (b) displays a wind gust (localized gust at 18:00 CDT) and subsequent response of blade and turbine power. The time signal segments were taken from run 4 and each signal was plotted with the mean removed and normalized by r.m.s. to allow direct comparison of fluctuations in time. (c) Torque (indicated in terms of reactive power P_R) and (d) blade pitch display the turbine control response.

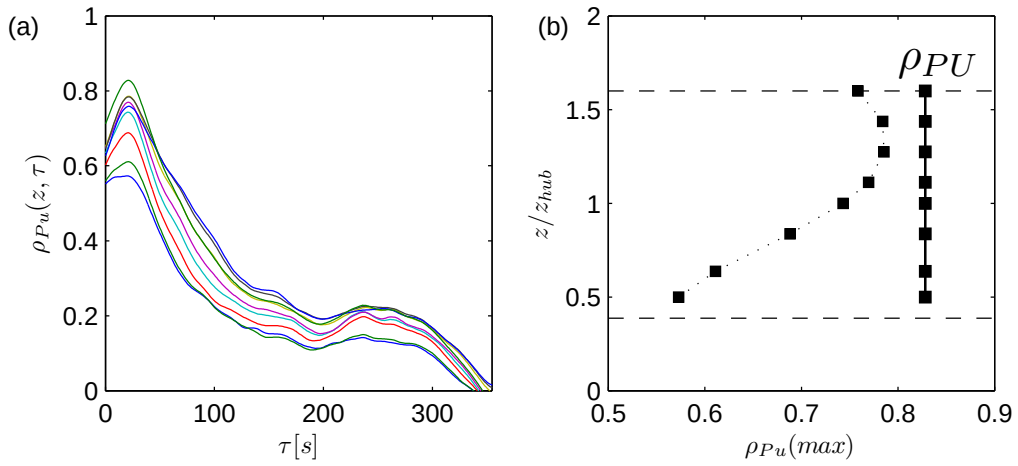

Figure 4.10: (a) Correlation of turbine power with the velocity time signals at various elevations z/z_{hub} shown for time lags τ up to the first zero-crossing. (b) Peak power to velocity correlation values for each velocity elevation shown with symbols as well as the power to rotor averaged velocity time signal (shown as solid vertical line). Correlation data and peak correlation tracking were obtained from run 4.

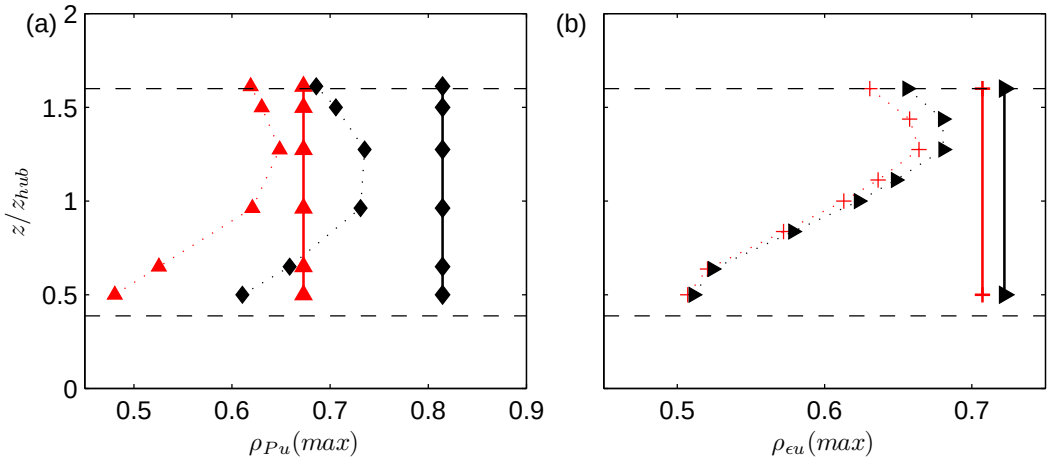

Figure 4.11: (a) Peak cross-correlation of turbine power to lidar measured velocity comparison between $x/D = 0.71$ (run 1) shown with black $\Diamond$ for both specific elevation velocities (curve) and rotor averaged velocity (solid vertical line) and $x/D = 1.02$ (run 2) plotted with red $\triangle$, for velocity time signals from specific elevations (curve) and rotor averaged (solid vertical line). (b) Peak cross-correlation between blade strain ϵ from the high pressure side of the airfoil and incoming velocity, for strain values at the root (+) and 37.5% ($\triangleright$) of the blade length (blade radii of 0 m and 18 m respectively) from run 4. Curves represent peak correlation between the strain and velocity at specific elevations, while the solid vertical lines are the correlation between strain and rotor averaged velocity.

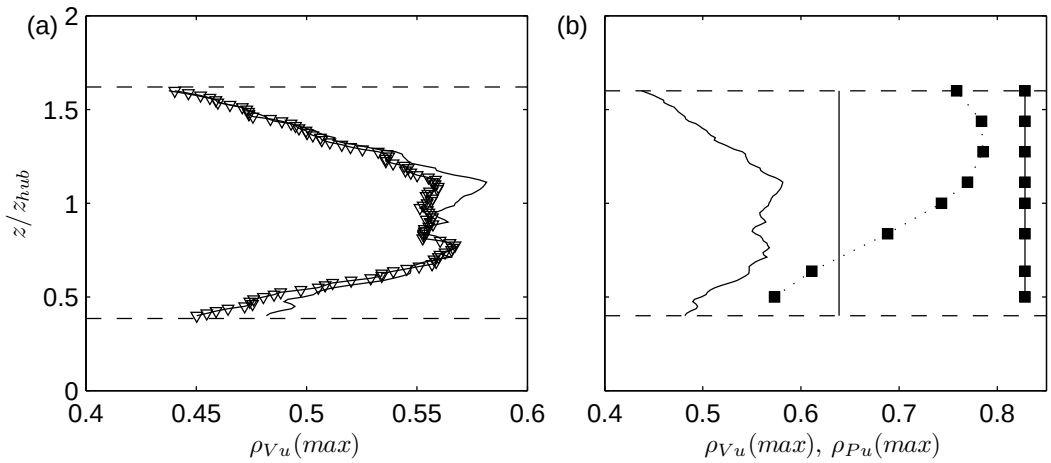

Figure 4.12: (a) Peak cross-correlation comparison investigating impact of lidar spatial averaging using PIV averaged with the lidar cone angle ($\triangledown$) and a constant averaging distance (solid line) for an upwind location of $x/D = 0.8$ for the case of a single turbine at the full vertical resolution of the PIV. (b) Peak cross-correlation curve comparison for single turbine arrangement between model-scale (solid line) and full-scale ($\square$). Vertical lines indicate the cross-correlation between the turbine production and rotor averaged velocity.

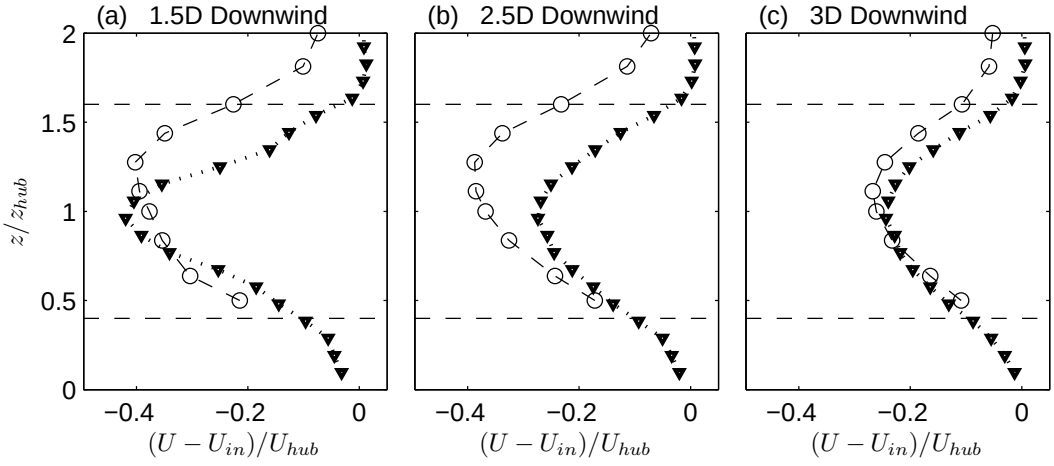

Figure 4.13: Wake comparison between lidar measurements (○) and hotwire measurements (▽) in the wind tunnel behind the model turbine for (a) 1.5D, (b) 2.5D and (c) 3D downwind of the turbines. U_{in}, or the inflow velocity profile, for the Eolos turbine with a southerly wind was measured by the met tower at approximately 1.7D upwind, and for the wind tunnel case U_{in} came from the baseflow (undisturbed) boundary layer profile.

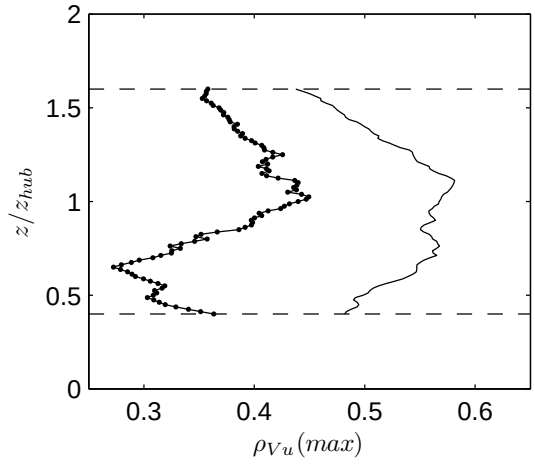

Figure 4.14: Peak cross-correlation between the turbine voltage and the PIV measured incoming velocity for $x/D = 0.8$ for the case of single turbine (solid line) and two aligned turbines (.).

Chapter 5

On the statistics of wind turbine wake meandering: an experimental investigation

The analysis presented in the previous chapter on upwind preview, specifically within wind farms, spurred the question and subsequent detailed analysis of the turbine wake movement. Information provided by this analysis on wake characteristics can be used to develop more accurate models that include meandering and other turbulence induced movements in addition to providing insight on the wake dynamics that moderate downwind turbine operation and structural loading. For this chapter, the instantaneous wake motion of a model wind turbine placed in the boundary layer wind tunnel at St. Anthony Falls Laboratory was captured through the use of a wall-parallel oriented particle image velocimetry (PIV) system. Each PIV vector frame was used to investigate mean (expansion angle, wavelength and convection velocity) and higher order (slope, curvature and correlation) wake meandering characteristics, allowing the comparison of four different wind turbine operating configurations. Here the inspected wakes include a single turbine operating with two different tip-speed ratios and the wakes of two aligned turbines (one viewing the wake of the upwind turbine and the second viewing the wake of the downwind turbine). Differences between the cases in the expansion angle and wavelength were found to be connected to the mean wake convection velocity, as was the

curvature of the filtered wake. The slope (characterized by the first order increments of the profile of the filtered wake signal) of the wake, on the other hand, was found to be influenced more by turbine configuration (single turbine versus two aligned turbines). Finally, analysis of the auto-correlation of the fluctuations about the filtered wake signal reveals a distinct signature of wake meandering on these fluctuations suggesting an influence of larger scales on smaller scales. This implies that the fluctuations at the wake edges, near the wake edge shear layer, have different characteristics than those at the mean wake centerline.

To be Submitted to *Physics of Fluids*, August 2014.

5.1 Introduction

Meanders are primarily observed in erosional and depositional geophysical systems, such as rivers, tidal or submarine channels and glaciers, where they are found to have different geometrical characteristics depending on local geomorphological processes, terrain and sediment characteristics, side and wall erosional rates, vegetation, among many other factors [90, 91, 92, 93, 94, 95, 96, 97]. Meandering flow patterns can however occur in other natural and anthropogenic systems, such as ocean streams, river mouth and planar jets [98, 99, 100, 101], in the wakes of bridge piers, marine hydro-kinetic turbines and wind turbines [102, 103, 29], and, at least qualitatively, share similar attributes with those observed in river networks and landscapes.

Among the different anthropogenic perturbations leading to meandering flows, we focus here on wind turbines and their wakes. Wake meandering has been addressed in detail by Sorensen et al. [104] and has also been found to originate from other rotating devices, (i.e. hydro-kinetic turbines), designed to extract energy from river flows [34, 29, 104]. Research in the area of renewable energy has been conducted in order to understand the complex flow produced in the wake of turbines, and subsequently, to formulate reduced complexity wake models, simulate large arrays at the power plant scale and eventually optimize turbine siting under boundary conditions imposed by river bathymetry or terrain topography. The main reason for increased reliability in wake prediction is that the preceding turbine's wake becomes the inflow for the next turbine and, consequently, controls its performance and operating condition, as well as

its unsteady loads and structural health.

First order turbine wake models (i.e. [105, 106]) utilize a constant wake expansion angle along with a uniform velocity deficit which decreases at a defined rate, similar to a bluff body wake profile [107]. The differences between hydro- and wind turbines, however, includes the Reynolds number of the incoming flow, specific blade and nacelle geometries, optimal tip-speed ratio, the relative position of the rotor within the boundary layer, terrain roughness and complexity, among many other factors. While these low order models are valuable to give initial estimates for either a hydro- or wind turbine wake, models which consider the incoming turbulence provide the best results for evaluating flow statistics within turbine arrays [108] or wind turbine wake flows on complex terrain [59]. Further development upon these initial models, with the inclusion of dynamic wake characteristics [109], have not necessarily lead to an increase in accuracy in terms of the velocity deficit [110], but have shown that wake meandering characteristics need to be further investigated in terms of both additional large scale flow features in the wake and the influence of wake motion on downwind turbine performance and structural loading. Several journal articles investigated turbine wake motion (i.e. [111, 112, 113, 109, 114]), however, to the best of our knowledge none has provided a detailed statistical description of wake meandering.

Here we focus on wind turbine wakes immersed in the lowest $\tilde{2}5\%$ of the turbulent boundary layer, as is the typical design configuration for utility-scale turbines in the atmospheric boundary layer [82]. We employ miniature turbines in the SAFL wind tunnel using PIV flow measurements to investigate wake meandering characteristics for different turbine configurations. Cal et al. [24] showed that the turbulence change within the developing wind farm adjusts the momentum transfer into the individual turbine wakes, which impacts the total power production of the turbine array. In this study, we adopt a set of basic turbine arrangements to reproduce typical turbine operating conditions within an array: first, single turbine at two different tip speed ratios, mimicking the adjusting of operating conditions for turbines; second, two aligned turbines in the mean flow direction, representing turbines within the turbine array experiencing the effect of the upwind turbine wakes. The major goal is to describe wake meandering statistically, and quantify the changes undergone for the investigated turbine operating conditions or geometrical configurations.

This paper is outlined as follows. Section 5.2 provides a descriptions of the wind tunnel, miniature wind turbine models, particle image velocimetry (PIV) setup and acquisition, baseline flow, as well as a table listing the experiments conducted. Details on wake capture from the PIV and variable definitions and the results are presented and discussed in Section 5.3. The conclusions drawn from the research are provided in the final section.

5.2 Experimental setup

Experiments were conducted in the closed circuit, atmospheric boundary layer wind tunnel at the University of Minnesota's St. Anthony Falls Laboratory. The tunnel has a 200 horsepower fan that blows down the 16 m long, 1.7 m by 1.7 m test section. A 0.040 m tall picket fence trip was placed after the 6.6:1 contraction to promote boundary layer growth. The boundary layer was developed over smooth aluminum floor panels that can be temperature controlled independently from the free stream air in order to simulate various atmospheric thermal conditions. Herein, the floor and air temperatures were held equal at 24 ^{o}C to provide thermally neutral conditions. The ceiling panels in the test section were adjusted to maintain a nearly zero pressure gradient growth of the boundary layer.

The wind turbine model used herein consisted of a fixed pitch, three-blade (GWS/EP-5030x3) rotor with a diameter D =0.128 m. The rotor, placed with the blade high pressure surfaces facing the inflow, was directly connected to a DC generator fixed at a hub height of 0.104 m, able to produce a differential voltage signal proportional to the rotor angular velocity [58]. The generator has been characterized to have a linear increase in output with velocity, a characteristic of the motor design and internal friction [58], and therefore maintains a nearly constant tip-speed ratio (TSR) of ≈ 5.2 in the free-spinning condition (i.e. when no outside voltage is applied to the generator). To adjust the TSR, and subsequently the power coefficient, an outside voltage is applied to the generator opposing the turbine rotation direction. The second TSR of 3.2 was selected, based on the miniature turbine performance curve, to provide the optimal power coefficient ($C_p \approx 0.27$).

A TSI PIV system consisting of two, 4 megapixel PowerView cameras, Insight 4G

software, synchronizer and a Big Sky 532 nm Nd:Yag laser was situated in a wall-parallel orientation such that it allowed the capture of streamwise and spanwise velocity fluctuations on a plane at hub height. Stitching the images from the two cameras together provided a field of view (FOV) of roughly $3.6D$ ($\approx 0.46\ m$) in the streamwise direction and $1.8D$ ($0.23\ m$) in the spanwise direction. This setup was used to capture the spanwise meandering and fluctuations in the wind turbine wake at hub height, where the rotation about the x-axis is assumed to be symmetric. The full FOV and camera arrangement is shown in Figure 5.1(a) with respect to an upwind and downwind turbine. The sampling rate for each case was 7.25 Hz, which is not fast enough to have time resolved movement of the wind turbine wake, but still provides data for ensemble averaging as well as spatially resolved instantaneous flow fields for the estimate of wake meandering statistics. The number of image pairs used herein was 700 for all of the cases except for the single turbine free-spinning test, where 1000 images were captured.

The PIV could not be used to calculate the boundary layer statistics, due to the horizontal orientation, therefore a vertical profile was taken with a two component hotwire anemometer. The hotwire was calibrated at the same 24 ^{o}C at ten angles between +/- 30^o for nine velocities. The Dantec hotwire probe was connected to an A.A. Lab System amplifier and boundary layer data was acquired with LabVIEW at 10000 Hz for 120 seconds at each elevation in the profile. More details on the hotwire setup and data acquisition can be seen in Howard et al. [58] and Singh et al. [66]. The resulting boundary layer profile is presented in Figure 5.1(b), and also noted on the profile is the elevation of the PIV plane. All runs were conducted at $U_{hub} \sim 5\ m\ s^{-1}$ under neutral thermal conditions. The corresponding Reynolds numbers Re_τ, Re_D and Re_δ were $\sim$ 9200, 42977 and 236440, respectively, where $Re_\tau = u_\tau \times \delta/\nu$, $Re_D = U_{hub} \times D/\nu$ and $Re_\delta = U_\delta \times \delta/\nu$, $u_\tau = 0.23\ m\ s^{-1}$ is the shear velocity, δ =0.6 m is the boundary layer thickness and $\nu = 1.5 \times 10^{-5} m^2 s^{-1}$ is the kinematic viscosity of air. See Table 5.1 for all flow related details.

Four different turbine configurations were tested in this study. The first is the single turbine operating as a free-spinning turbine (no applied load), denoted hereafter as ST Free. The second test condition used a voltage applied to the turbine such that the turbine is operating at its optimal TSR, hereafter called ST Opt. The comparison of

Table 5.1: Flow statistics for turbulent boundary layer with $U_{hub} \approx 5\ m\ s^{-1}$ as measured by a hot-wire anemometer.

δ $[m]$	u_τ $[m\ s^{-1}]$	U_{hub} $[m\ s^{-1}]$	U_δ $[m\ s^{-1}]$	Re_τ [-]	Re_D [-]	Re_δ [-]
0.6	0.23	5.0	5.91	9200	42977	236440

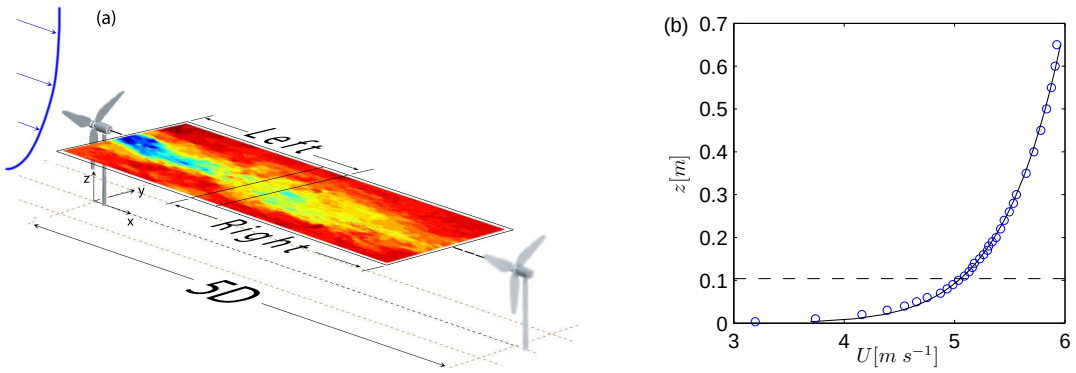

Figure 5.1: (a) Schematic of the PIV sampling area in proximity to the turbines. The combined left and right cameras are capturing a wall-parallel field of view at hub height with a total streamwise length of just under $3.6D$ ($\approx 0.46\ m$) and spanwise breadth of $1.8\ D$ ($0.23\ m$). (b) Boundary layer mean velocity profile as measured by the two component, hot-wire anemometer. The horizontal dashed line denotes the elevation where the wall-parallel PIV was captured (turbine hub height) and the solid black curve is a power law with an exponent of 0.09, for $U(z) = U_{hub}(z/z_{hub})^{1/0.09}$.

these first two tests not only provides an inspection of TSR effect on wake meandering, but coupled with that, the influence of the velocity deficit on wake characteristics. The last two experiments were designed to provide initial data on wake development in a turbine array by aligning two turbines in the streamwise direction with $5D$ spacing (spacing selected as it is a nominal distance used in wind farms today); PIV measurements captured the wake of the first turbine (TT) and the wake of the second turbine (TT wake). Details on these cases can be found in Table 4.1.

Table 5.2: Wind turbine cases implemented in the wind tunnel. When two turbines are tested, they are aligned in the streamwise direction at a spacing of $5D$ measured from rotor plane to rotor plane. TSR denotes the tip-speed ratio and FOV is the PIV field of view in the x-direction in reference to the rotor plane of the upwind turbine, or first turbine in the case of two aligned turbines.

	Single Turbine-Free (ST Free)	Single Turbine-Optimal (ST Opt)	Turbine-Turbine (TT)	Turbine-Turbine Wake (TT Wake)
TSR	5.2	3.2	5.2	5.2
FOV $[x/D]$	0.5 - 4.1	0.5 - 4.1	0.5 - 4.1	5.5 - 9.1

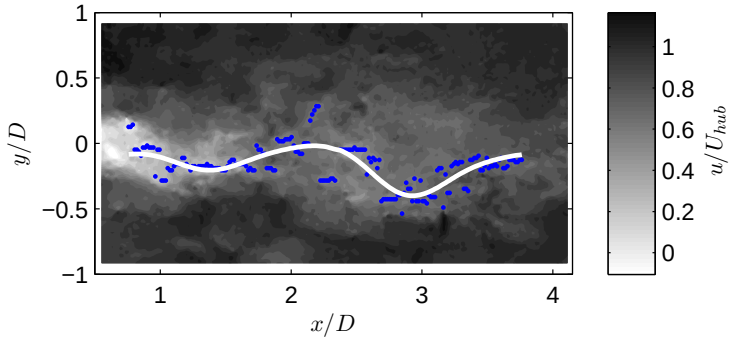

Figure 5.2: An instantaneous velocity field contour from PIV is shown from the single turbine case with the blue dots marking the minimum streamwise velocity. The wake minima at each x-location are then low-pass filtered to form smooth wake signal, plotted as the white curve. The filtered wake provides the basis for estimating the meander wavelength, which for this PIV instance would be $\lambda/D \approx 1.5$ as calculated from the local minima at $x/D \approx 3$ and 1.5.

5.3 Results and discussion

5.3.1 Wake capture and definitions

The instantaneous wake meander is defined as the minimum streamwise velocity $u(x, y)$, found within a rectangular area in the wake for each x-location. The full PIV spatial resolution is used here to locate the minima in the y-direction (y range of +/- $0.75D$), as shown in Figure 5.2(a). The resulting wake meander for each PIV realization starts just downwind of the hub and wanders, along with some smaller scale fluctuations, about a general oscillating trend. It should be clarified that the wake of the wind turbine is highly three-dimensional and rotates opposite to the rotor rotation direction [113], therefore we are actually capturing a slice of the helicoidal hub vortex [104, 114]. Despite this rotational component, the wall-parallel PIV plane can still describe the spanwise meandering of the turbine wake and, if coupled with wall-normal measurements, could help define the three-dimensional oscillations of the wake.

By observing the instantaneous, raw, unfiltered, wake meander signature [$u(x, y)$ minima marked as dots in Fig. 5.2(a)], we recognize the oscillatory nature of the turbine wake and harken back to the smooth and gradual river meandering described in [90, 91,

94]. In order to follow the estimation of the mean meander quantities as introduced by the geomorphology community, the raw signal is low-pass filtered to produce a smooth, meandering wake, as shown by the white curve in Figure 5.2. Here, the cutoff frequency was defined as 50 Hz to allow the fluctuations on the order of the turbine frequency to persist in the wake while removing the higher frequency content. In Figure 5.3, a set of instantaneous vector fields are provided to demonstrate how the wake meandering large scale signature is modulated by small scale vortices generated in the turbine near wake. This figure displays four locations within the wake focused on the local flow minima. In each of the windows in Figure 5.3, a different streamwise (convection) velocity is removed from the instantaneous vector field to allow the exposure of vortices within the wake [115]; each window shows that the wake minima primarily occur at the edges of vortices located close to the large scale flow meander (the solid curve). The various sources of vorticity are the turbine nacelle (generating the hub vortex), the blade tips, and the shear layers around both the hub and the rotor, in addition to potential interactions between the above structures. As evidenced in Figure 5.3, the velocity minima method cannot distinguish between the large scale wake meandering and the small scale vorticity; thus the reason a spatial low-pass Fourier filter on the raw $u(x, y)$ minima was implemented (to provide data with scale separation). Each instantaneous PIV vector field is analyzed in the same way to produce both the low-pass filtered wake as well as the fluctuations about the filtered wake. $l_{raw}(x)$ is defined as the location of the $u(x, y)$ minima (in the y-direction, for each x location) and $l_f(x)$ as the spatially smoothed curve defining the filtered wake meander. The signal for the spanwise small scale fluctuation of the wake is then computed by $l' = l_{raw} - l_f$ and these fluctuations are due to the small scale vortices superimposed and interacting with the larger scale meandering motion. The result of this processing provides, for each turbine configuration, a number of instantaneous wake meanders $l_f(x)$ and fluctuations $l'(x)$ equal to the number of PIV vector fields.

We stress that the high spatial resolution measurements provided in Figure 5.3 confirm that the fluctuations l' of the wake minima are physical, not a source of erroneous vectors from PIV interrogation, and therefore deserve further investigation.

Next, we define the mean wake edge by marking the occurrence of the wake minima for all vector fields (the dots in Fig. 5.2) and defining a continuous, spatial x, y

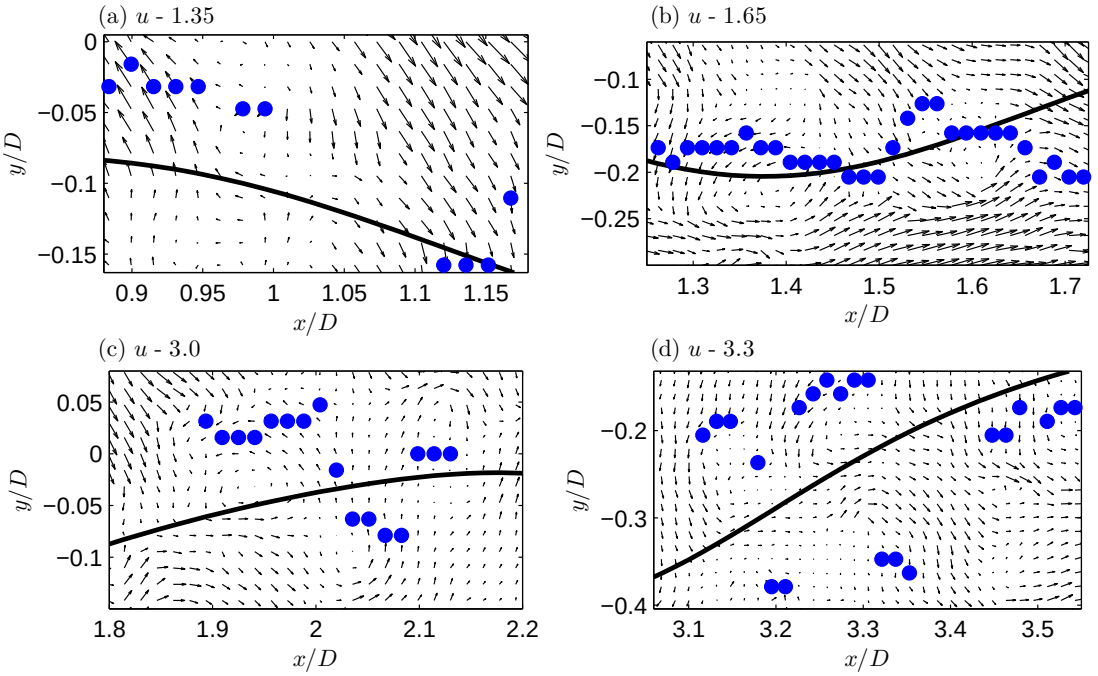

Figure 5.3: Snapshots of u, v vector fields around selected, local streamwise velocity minima (blue dots) in relation to the spatially filtered wake signal (solid black curve). Instantaneous velocity fields are displayed after the subtraction of a constant streamwise wake velocity U_C in the following x-range (a) $0.9 < x/D < 1.2$ with U_C=1.35 $m\ s^{-1}$ (b) $1.25 < x/D < 1.75$ with U_C=1.65 $m\ s^{-1}$, (c) $1.8 < x/D < 2.2$ with U_C=3.0 $m\ s^{-1}$, and (d) $3.05 < x/D < 3.55$ with U_C=3.3 $m\ s^{-1}$.

domain where instantaneous wake meanders traveled at least one time. The specific $y(x)$ position of the mean wake edge is then selected as the point, at each x location, delimiting an uninterrupted domain in the spanwise direction. The result is two, fairly symmetrical curves, one at each side of the nacelle marking the left and right edges of the meander domain along the wind direction.

It is important to recall that the wake domain is chosen to be spatially continuous, implying that no gaps exist in the y-distribution of wake minima occurrence; Figure 5.4(a) shows how the edges are defined for each x-location, distinguishing between the continuous wake meandering domain in the spanwise direction and the occurrence of rare velocity minima outside of such domain. These outer minima take place on average 0.3%

of the time up to $x/D = 2$ and only increase to an occurrence of 1% at approximately $x/D = 4$; they are thus regarded as extreme wake oscillation events and are not included in the mean wake edge definition. Statistically, the edge points correspond to the first and last empty bins of the spanwise distribution of wake minima. The resulting left (+ y) and right (- y) edges identified for the single turbine case are shown in Figure 5.4(b) as white dots plotted on top of the mean streamwise velocity contour. The mean expansion angle is then computed as the angle between the x-axis and a line fit through the points defining the edge.

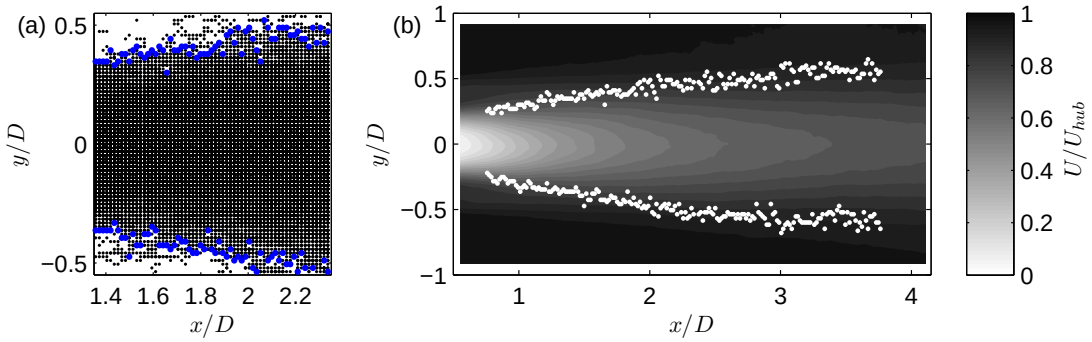

Figure 5.4: (a) Local sample of the wake minima (black dots) representing the unconditioned wake domain (the continuous portion is delimited by the blue dots, defining the wake edges). (b) Full-scale distribution of the estimated wake edges (white dots) superimposed on the mean streamwise velocity contour as captured by wall-parallel PIV.

5.3.2 Mean wake statistics

Before investigating the comparison between the four cases, we highlight a couple of interesting features observed in Fig. 5.4(b): first, by tracking $\partial U/\partial y$ in the mean velocity contours, we note that the beginning of the wake edge (with respect to the rotor plane) is found to follow the shear layer introduced by the root and hub vortices interaction; second, for $x/D > 1.75$, the wake edge experiences a higher variability in position (y) about the mean as measured by the spanwise variance; it is hypothesized that this is due to the reduced strength of the wake edge shear layer with increased x/D position, especially after the hub shear layer interacts with the tip vortex shear layer. This second finding helps to understand the evolution of the wake characteristics

presented by [114] near $x/D \approx 2$, where in our data we note a significant change in the fluctuations of the wake edges, especially on the left side [upper side in Figure 5.4(b)]. We stress again that turbine wake flow is highly three-dimensional, with a non zero mean streamwise vorticity induced by the rotor angular velocity, which results is an asymmetrical wake. The largest wake edge variation occurs near x/D on the left edge, and it is hypothesized that this variation is induced by the wake flow interacting with higher momentum fluid (creating a means of momentum transfer), caused by the wake counter rotation which makes the component of velocity through the PIV plane at the left wake edge in the $+ z$ direction; this increased variance only arises after the wake edge is out of the sheltering effect of the velocity deficit produced by the rotor ($x/D > 2$). We infer that the instantaneous fluctuations of the wake edges and the spatial evolution of the near-wake meandering motions are governed by the interaction between the hub vortex and the higher momentum fluid entrained along the tip vortex shear layer, occurring at $x/D \approx 2$ for the data presented in Fig. 5.4(b). Precise details on this interaction, studied for hydro-kinetic turbines by [114], which may be used to define the limit between near and far turbine wakes, are currently being investigated for this model wind turbine and will be presented in future work.

The comparison between the mean edge expansion angle γ for the four different cases is presented in Figure 5.5(a). It can be seen that for all of the turbine configurations, the left and right edge expansion angles are different. We hypothesize that the asymmetric expansion angle is caused by the primary rotation direction of the wake about the x-axis, shown by [113], induced by the equal and opposite reaction to the flow impacting the rotor. To ensure that this feature was not due to the streamwise velocity inhomogeneity in the spanwise axis of the tunnel, wall-parallel PIV measurements were conducted in the baseline flow as well, confirming variations of $U(y)$ smaller than 0.9% of the hub velocity, across the sampling region. Moreover, when comparing the two single turbine operating conditions we found that the difference between the left and right edge angle is enlarged for the ST Opt case where the turbine has a reduced TSR, as compared to ST Free. In the ST Opt case, the turbine is operating at peak efficiency, which means that the torque on the blades is increased and subsequently, the counter rotation of the wake is expected to be larger with respect to the ST Free case (higher TSR, but negligible torque). It is proposed that the inherent asymmetry of the turbine wake is amplified by

the increased strength of the counter rotation, causing the greater discrepancy between the two wake edges. The turbine rotor used in this set of experiments rotated in the counter-clockwise direction, when viewed from upwind; therefore, the wake flow was expected to rotate in a clockwise manner such that, at the left edge of the wake ($+ y$), the primary out-of-plane velocity direction is in the $+ z$ (out of the PIV domain) and oppositely for the right edge. The wake flow along the right edge then serves to transfer high momentum fluid down, towards the wall, and the rotation acts to pull the right wake edge in the direction of rotation, similar to the expanding diameter of a vortex ring when it impacts a solid boundary (see for e.g., [116]).

The second noteworthy trend in Figure 5.5(a) is the difference in mean expansion angle between the different cases studied here. The single turbine ST Free and the upwind turbine wake in the turbine-turbine configuration (TT) exhibit relatively higher mean angles, as compared to the single turbine at optimal TSR (ST Opt) and the downwind turbine-turbine wake (TT wake). The similarity is understandable as both rotors are exposed to the same incoming flow, have the same TSR and thus induce the same velocity deficit. The trend between the four cases is confirmed through inspection of the amplitude of filtered wake signal, shown in Figure 5.5(b). However the difference between ST Opt and ST Free is more subtle: a turbine operating at peak performance induces a larger velocity deficit and thus has a larger mean shear (at the wake edge) able to sustain the tip vortices along the x-axis. A strong tip vortex structure, harbored in the shear layer produced between the high momentum fluid outside the wake and a large velocity deficit, keeps the wake confined and limits the entrainment of high momentum fluid, resulting in a smaller expansion angle. It is also argued that the expansion angle for the less efficient turbine cases must be a function of the pressure downwind of the rotor; however, as no direct pressure measurements were taken, we focused on the filtered wake meandering data and its interaction with the surrounding flow to gain a better perspective. Howard and Temberger [91] suggested a range of approximately 50 to 60 meanders (a meander is classified as one wavelength) for good statistical convergence, implying that our number of captures per turbine configuration of > 700 is well beyond the suggested length on an ensemble basis.

A comparison of the mean wavelength from the filtered wake signals for the different turbine configurations is shown in Figure 5.6(a). The wavelength is estimated as the

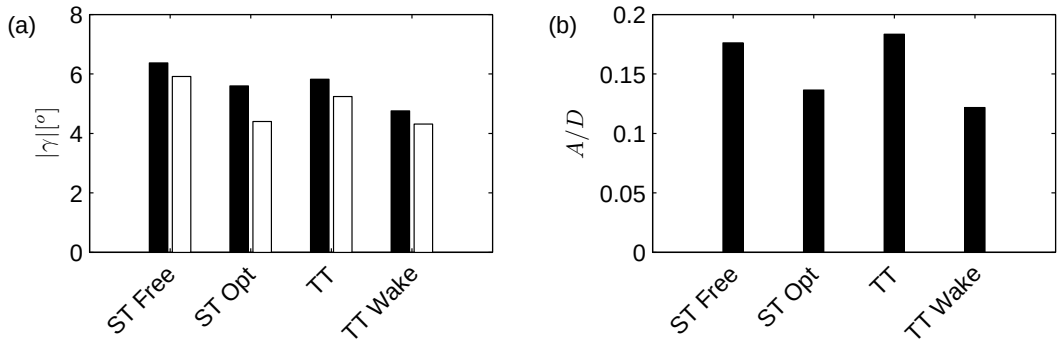

Figure 5.5: (a) Comparison of edge expansion angle γ between multiple turbine configurations. The expansion angles calculated with the right edges (- y) are the black bars and the left edge (+ y) angles are shown in white bars. (b) Amplitude of meander, computed as an average from local maximum to local minimum.

length scale comprised between two consecutive local minima or local maxima of the low-pass filtered meandering signature: for instance, if we consider the meander in Figure 5.2, the local minima are precisely located at $x/D \approx 1.5$ and $x/D \approx 3$, therefore, we estimate $\lambda = 1.5D$, and so on for each realization. The overall change of the mean wavelength, between the various cases, follows the same trend presented by the edge expansion angle: larger expansion angle implies weaker wake shear layer, a lower velocity deficit (higher mean wake velocity) and a stretched meandering signature in the $x-$ direction (thus a larger λ). Accordingly, when the wake is produced by an efficient turbine, more streamwise momentum is extracted by the device, resulting in a larger velocity deficit in the wake (lower wake velocity) and a wake meander which has a lower wavelength. In the case of the aligned downwind turbine (TT wake), we infer that the deflection of large turbulent structures by the upwind turbine [66] to the wake edges are keeping the downwind turbine wake more confined; in addition the velocity deficit is further increased, with respect to the undisturbed hub velocity, resulting in increased shear and lower wake velocity (hence low γ, low λ). The mean wake velocity in the wake U_c appears thus to be the key governing parameter for meandering that we can extract from PIV measurements.

U_c is calculated using an area defined by the wake edge for each of the instantaneous PIV fields. As shown in Figure 5.6(b), the wake velocity for the cases with longer wavelengths (and greater wake expansion) is higher, as anticipated, as a higher wake velocity

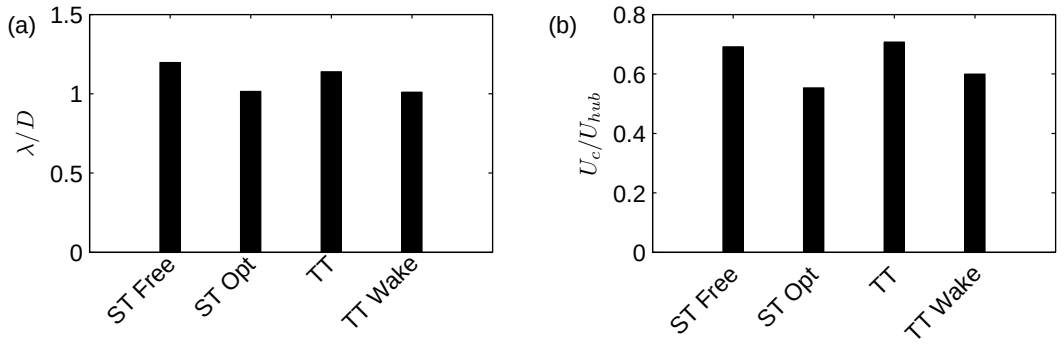

Figure 5.6: (a) Comparison of wavelengths between the different experiments investigated herein. (b) Mean wake velocity U_c comparison in the wake of the different cases. U_{hub} for all cases is the hub velocity in the undisturbed boundary layer.

stretches the hub and tip vortex structures in the streamwise direction (measured by the increase in wavelength), but reduces the shear layer intensity at the wake edges. This wake edge shear layer contributes to confine the spanwise wake meandering expansion (measured by the edge expansion angle). The main driver of these mean wake meandering statistics (γ, λ) appears therefore to be the wake velocity, or in another words, the wake velocity deficit. A greater velocity deficit compresses the wake meanders in both horizontal directions, while a lower velocity deficit induces the opposite effect.

5.3.3 Higher order wake statistics

Utilizing the instantaneous turbine wake PIV fields and the filtered meander signal, we can further analyze wake statistics to understand the effect of the shear on the meander as well as the small scale vorticity on the l' fluctuations, induced by small scale vortices generated by sub-shear layers within turbine wake itself. On the low-pass filtered meander l_f, the normalized slope C_1 and curvature C_2 can be calculated using,

$$C_n = \frac{1}{D}\left(\frac{\partial^n l_f(x)}{\partial x^n}\right), \tag{5.1}$$

where D is the rotor diameter (used for normalization), and n is the order of the derivative (1 or 2) to provide a measure of the slope or curvature of the signal, respectively. The probability density function (pdf) $F(x)$ of the computed slope is presented in Figure 5.7(a). The distribution of the slope for all of the cases can be approximated by a

Gaussian distribution, however, a slight shift in the mean is observed (skewed distribution), suggesting an asymmetric wake, as evidenced in the expansion angle statistics. The pdfs in Figure 5.7(a) can be further separated into two groups. In contrast to the trend observed for γ and λ as a function of the mean wake velocity, the ST Free and ST Opt are shifted together off-center away from the symmetric Gaussian profile while the TT and TT wake cases remain on-center and show slight asymmetry towards the right. The slope C_1, when put in terms of the turbine wake, elucidates the directionality of the wake meander. A divergence from a mean slope of zero for the single turbine case shows that there is a primary slope (or direction other than parallel to the x-axis) that occurs for an individual turbine (independent of the TSR). While the slope pairing (ST Free with ST Opt) is opposite to those noted by γ, λ, U_c, both the wake amplitude A (another measure of the wake expansion) and wavelength λ increase or decrease together when comparing ST Free and ST Optimal. Therefore, the wake is manipulated in both the x and y directions together, which allows the slopes to be very similar between the two cases, hence the collapse of C_1. However, when that turbine is placed into a more complex situation, for example the turbine-turbine, the wake directionality (as defined by the shape of the C_1 pdf) is shifted back toward zero (aligned with the x-axis) due to the influence of the downwind turbine [this is also seen in the reduction of wake expansion angle γ for the TT case versus ST Free, see Fig. 5.5(a)]. Upon interaction of the upwind turbine wake with the second turbine, the new wake formed has a further homogenized scale composition [66] and thus produces a more symmetric pdf of the wake slope. For reference, a sine wave would produce a slope pdf that is perfectly symmetric about zero; therefore any deviation from symmetry points to a unique identifier of the turbine wake meandering.

The curvature C_2, shown in Figure 5.7(b), displays the influence of the incoming and surrounding flows on the wake meander characteristics. Note here that a line has zero curvature, and a circle has a constant curvature. Now looking at Figure 5.7(b), the four test cases are split again into two sets being ST Free with TT and ST Opt with TT wake, which are the same groupings presented by the expansion angle, wavelength and mean wake velocity. This similarity is not a coincidence, as the curvature is very much linked to the strength of the wake edge shear layer and to the opening angle of the wake. In the plot, the ST Free case is the least symmetric followed by the TT, as the

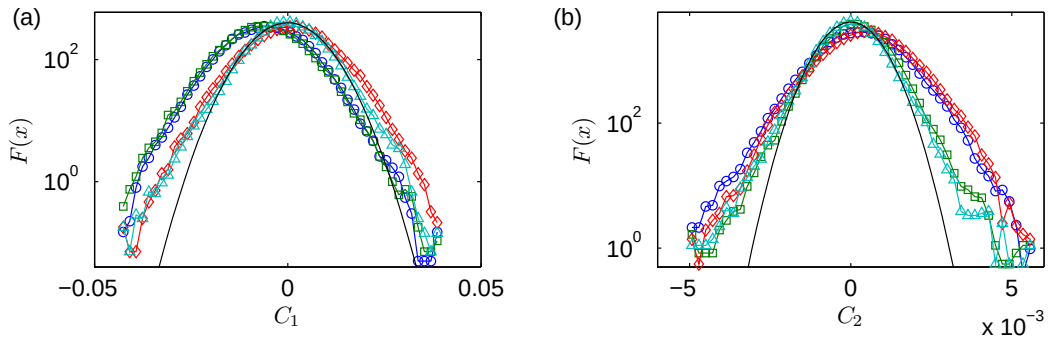

Figure 5.7: The low-pass filtered wake is analyzed through the pdfs $F(x)$ normalized such that the area under the curve is equal to unity for (a) the slope and (b) the curvature for each of the turbine tests. The statistics are calculated using all of the instantaneous PIV fields available for each of the runs. ∘ represents the single turbine free, □ the single turbine optimal, ◊ the turbine-turbine upwind wake, and △ the turbine-turbine downwind wake cases. The solid black curve is a Gaussian distribution with the same mean and standard deviation as the TT wake case.

front turbine wake is expected to produce more positive wake curvature than negative because of the difference between the left and right wake edge angles. Note, positive curvature is measured at local minima while negative curvature at local maxima. Two key features observed in the small range of curvature for the ST Opt and TT wake sets, are the near symmetry of the pdfs and the sharp increase in curvature for $C_2 >$ 4e-3. The symmetry of the pdfs point out that the wake meanders for these two cases are closer to a (relatively) low amplitude periodic function, gently increasing in x. It is proposed that the leveling off of curvature near $C_2 \approx$ 4e-3 (introduced at higher positive curvature) is the reaction of the wake to the changing intensity of the wake edge shear layer, also reflected in the left-right asymmetry of the wake expansion angle.

To investigate the mutual effect of the wake meander on the fluctuations ($l' = l_{raw} - l_f$, where l_f is the spatially filtered curve describing the large scale wake meander), we compute the pdf $F(x)$ of the fluctuations for each of the cases, shown in Figure 5.8(a). The pdfs in the semilog plot suggest a deviation from the Gaussian distribution, and can in fact be well approximated by a double exponential distribution. Here we point to the increase in turbulent fluctuations and the homogenization of turbulent scales observed in the wake [66] to explain the increase in the variability of the instantaneous wake signature. Note that in the recent study by Singh et al. [66], it was observed that

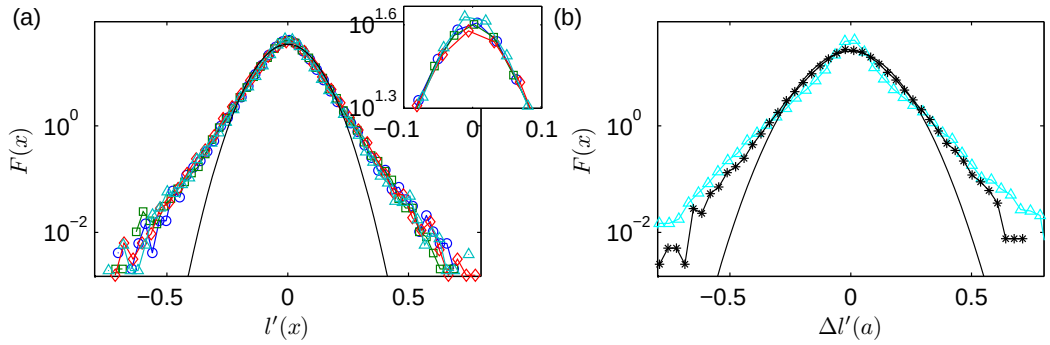

Figure 5.8: (a) Semilog plot of the pdfs $F(x)$ of the fluctuations for the four cases with the insert showing a zoomed view of the peak; the symbols o, □, ◊ and △ represent the single turbine free single turbine optimal, turbine-turbine, and turbine-turbine wake cases, respectively. (b) PDF of scale-dependent increments $\Delta l'(x,a) = l'(x+a) - l'(x)$ for $a = \Delta x$ (△), $a = 0.5\lambda$ (▽) and $a = \lambda$ (.) on the Turbine-Turbine wake case. The solid black curve is the pdf of a Gaussian distribution with the same mean and standard deviation as the turbine-turbine wake case. All the plots are normalized such that the area under each curve is equal to unity.

wind turbines reduce the intermittency and asymmetry in the wake flow by breaking and/or deflecting the large-scale flow structures of the incoming flow, thus rendering the structure of the velocity fluctuations more homogenized, as compared to the boundary layer flow.

A Gaussian pdf with the same mean and standard deviation as the TT wake case is plotted for comparison in Figure 5.8(a). The four cases here have the same $l'(x)$ pdf profiles over the entire slope range, however, upon closer inspection of the pdf (inset plot showing peak), we find that the TT wake (△) has higher peakedness (kurtosis) compared to other cases. The slight increase in the pdf of the fluctuations $l'(x)$ for this case shows that the higher occurance of low displacement from the filtered meander is linked to the reduced mean wake velocity U_c and reduced spanwise expansion A/D (less outside forcing limits the deviation from the smooth meander).

Following the findings of Singh et al. [66] for scale-dependent velocity increments, we define a spatially varying, meandering raw signature using $\Delta l'(x,a) = l'(x+a) - l'(x)$ based on the fluctuations $l'(x)$ and a length scale a comparison between $a = \Delta x$ and $a = \lambda$ (where λ is the mean wavelength). The pdfs of the l' increments change their shape from double exponential toward Gaussian, a signature of multiscale processes [117, 118],

as shown in Fig. 5.8(b) where the solid black curve shows a Gaussian distribution with the same mean and standard deviation for the TT wake case. We note that the tails of the pdf for $a = \lambda$ departs from the Gaussian distribution (thicker tails) due to the lack of data at the larger slopes. This finding suggests that fluctuations in the meandering wake manifest a multiscale type of behavior, a key physical phenomenon which has been observed in many natural processes denoting non-local energy transfer and strong interactions ([117, 118] etc.). Both non-local energy transfer and strong interactions are expected to occur in the turbine wake, where a large scale meandering, low velocity region delimited by a likely annular shear layer, interacts with the tip vortices and the surrounding high momentum, large scale structures to produce the small scale vortices observed in the instantaneous realization (Figure 5.3) and referred to here as wake fluctuations. Such interactions are investigated below using the auto-correlation of the streamwise velocity $\rho_{l'l'}(r)$.

In particular, $\rho_{l'l'}(r)$ is calculated to further investigate if the wake fluctuations have a memory of outside forcing due to their location in the wake, or in other words, if the fluctuations manifest some type of structure as they depart from the wake centerline. Here we define the mean as the trace of the large scale wake meandering patterns l_f, while the fluctuations $l'(x)$ represent the locations of the wake minima departing from the meander due to small vortices generated along the wake. The spatial auto-correlation defined below is Lagrangian in nature, as the meander signature varies in each instantaneous flow field.

$$\rho_{l'l'}(r) = \left\langle \frac{\langle l'(x,n)l'(x+r,n)\rangle_x}{\sigma^2_{l'(n)}} \right\rangle_n , \tag{5.2}$$

where l' is the $y(x)$ location of the fluctuation about the filtered wake, r is the spatial lag variable and n marks the instantaneous PIV flow field over which the ensemble average is performed. $\rho_{l'l'}(r)$ is computed for each instantaneous wake $l'(x,n)$ and then ensemble averaged over all runs, producing the four curves presented in Figure 5.9. It can be seen from Fig. 5.9(a) that the correlation coefficient reduces from $\rho_{l'l',r=0}$=1 (as imposed by the normalization) and exhibit, after the first zero crossing, a periodic oscillation for increasing spatial lag r, with a the local minima at $r/D \approx 0.2$, (anti-correlation), and a local maxima at $r/D \approx 0.5$ (positive correlation). Note that the auto-correlation coefficient of a sine wave produces a perfect correlation at $r = 0$, and

is perfectly anti-correlated at $r = \pi$. This correlated/anti-correlated trend continues indefinitely, thereby producing a smooth, oscillating correlation coefficient. With this comparison in mind, we can show that the fluctuations about the filtered wake do in fact have a signature (memory) of their location in the wake. The local maxima of the correlation coefficient are roughly spaced at (gradually increasing) $r/D \approx 0.5$, which when referring to Fig. 5.6(a) is approximately 0.5 of λ for each of the cases.

This suggests that the fluctuations occurring near the spanwise extremes (local minima and maxima) about the filtered wake l_f have similar tendencies (and similar forcing from an outside source) for all x locations, and are thus driven by their location on the large scale meander developing in the wake. The spatial lag of 0.5 r/D is also consistent between the various turbine configurations and highlights the fact that the fluctuations located at the filtered wake minima and maxima exhibit similar trends consistently with the meander curvature. The significance of $0.5r/D$ is that (i) the fluctuations do not specify at which wake extreme (+/- y) they are located, but that the outside forcing (wake edge shear layer) produces a statistically similar vortex in an alternated pattern with respect to the meander signature and (ii) another estimate of the wavelength could then be calculated through the auto-correlation of the fluctuations. It is proposed that the signature of these outer/inner edge fluctuations is due to the interaction between the wake edge shear layer and the wake meander, resulting in stronger instabilities at maximum curvature locations. It is not clear yet if wake meander oscillations are the cause or the effect of these smaller eddies near the mean wake centerline; it could be speculated that the hub vortex fuels the near wake instability, where smaller eddies are generated, while the latter interacting with the wake shear layer contributes to the wake meander large scale instability.

Figure 5.9(b) shows the zoomed view of the ACF up to the third zero crossing. In this frame we see that again, two groups are formed from the four different test configurations. The two cases with the shorter oscillaion period are ST Opt and TT wake, which shows that indeed the wavelength is the defining feature in the ACF as these two tests have the shortest wavelengths [Fig. 5.6(a)]. The ensemble averaged ACF from the ST Free and TT cases have a similar magnitude of the correlation value when compared with the shorter wavelength cases, but show a slight increase in period, as was recorded by the increase in wavelength.

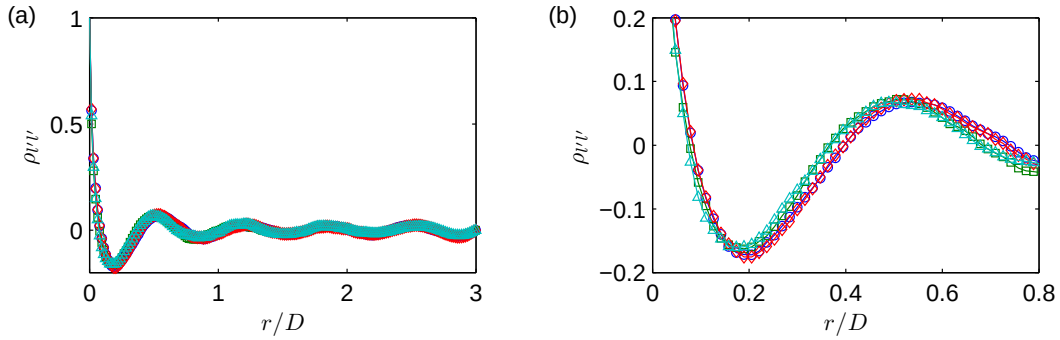

Figure 5.9: The auto-correlation of the fluctuations about the filtered wake signals. (b) focuses on the first and second zero crossings to show the shift in length scales between the different cases. The single turbine free single turbine optimal, turbine-turbine, and turbine-turbine wake cases are shown by symbols o, □, ◊ and △, respectively.

5.4 Summary and Conclusions

Two dimensional velocity measurements collected up to $4D$ downwind of a model wind turbine via a spatially resolved wall-parallel PIV setup were analyzed to quantitatively describe wake meandering under four different turbine operating conditions and configurations. The turbine wake meander signature was first identified as the low-pass filtered signal of the minimum streamwise velocity at each x-location. The spatial filter was introduced to distinguish between the smooth meandering pattern, resembling those observed by geomorphology community in rivers and streams, from smaller eddies formed around the center of the meander and statistically representing spatial fluctuations. Wake statistics, including the mean expansion angle, meander wavelength and mean wake velocity, along with higher order statistics relating the meandering signature (slope, curvature) with the nearby eddies (auto-correlation function) allowed us to highlight the following results:

- The wake expansion angle, measured from the centerline axis of the turbine to the left ($+y$) and right ($-y$) wake edges, (i) is not symmetric about the mean wake centerline due to the fixed rotation direction of the turbine rotor, (ii) the discrepancy between the edge expansion angles is influenced by the tip-speed ratio (coupled to the power coefficient) and (iii) the velocity deficit influences the mean wake expansion angle.

- The wavelength of the wake meander, calculated using local minima and maxima in the low-pass filtered wake signal, was found to be directly changed by the mean wake velocity. For example, an increase in the convection velocity causes the wake meandering to stretch, thereby increasing the wavelength.

- Statistical analysis of the low-pass filtered wake found that the asymmetry and shift in the slope pdf was driven by the convection velocity, whereas the curvature was controlled by the variance induced by outside forces on the wake meander.

- The fluctuations about the low-pass filtered wake were found to have (i) an exponential pdf for all of the cases due to the homogenization of turbulent scales [66] and (ii) the highest variability when a turbine is downwind (blockage influences wake movement).

- The auto-correlation of the fluctuations about the wake meander shows that the fluctuations have a memory of the original wake signal, meaning that they have an imbedded signature of their location in the wake. Also because of this memory, the wake wavelength can be identified through the auto-correlation. Here it was proposed that the wake fluctuations near the local minima and maxima are introduced to higher shear, which increased the variability at those locations and produced an auto-correlation signal that modulates with the wake wavelength.

The findings presented above can not only provide checks for turbine wake models but also detailed information on wake movement that may be useful for downwind turbine performance and structural loading. Also, I note here that the discussion during my final oral defense led to the idea that in this chapter, the near and far wakes of the turbine are not distinguished. It is clear that the evaluation presented herein is highlighting the near wake and for publication, this fact should be stated, as the far wake also has a meandering characteristic that will be investigated in future research. It is even possible that the current research has details which provide insight into the separation of the near and far wakes.

Chapter 6

Investigation into control modifications for increased wind farm performance: a wind tunnel study

The research into improving and understanding large wind farm performance was inspired by the unique findings of Chapters 2,3 and 5, coupled with the fact that the number of wind turbines within these farms are growing. This increase in wind farm size, incorporated with knowledge that the wind magnitude and direction is not constant from day to day, fueled the idea to test simple modifications to turbine operating variables that will reduce the production of the individual turbine while allowing the total wind farm production to increase. The investigated modifications, that can be implemented into existing technology through control logic changes, are specifically (i) yaw misalignment and (ii) tip-speed ratio adjustment. To test the different turbine operating conditions, model wind turbines were situated in a boundary layer wind tunnel to form an aligned wind farm consisting of 15 turbines, with 5 streamwise rows and 3 spanwise columns. Turbine performance data (mean and fluctuating output) were monitored through the voltage output of each turbine within the array. Baseline data was gathered first from an aligned array with different streamwise spacing and from a

staggered array in order to provide a reference for the other test configurations. For a $4D$ streamwise by $3D$ spanwise spaced, aligned farm, front row yaw misalignment produced a reduction of total power -0.3% for a yaw of -15^o, due only to loss of production of the front turbine row. In a $5D$ (streamwise) by $3D$ (spanwise) aligned farm, tip-speed ratio adjustment increased the production of the last four rows by 1%, however, due to the method of implementing tip-speed ratio adjustment, the production change for front row of turbines is unknown. As a reference, a staggered farm with $5D$ by $3D$ spacing produced 11.9% more than the aligned case. A precursor study to the one presented below investigated mean voltage statistics for many different wind farm arrangements, speeds, etc. and was conducted by a high school student, to whom I was a mentor.

6.1 Introduction

A shift toward higher alternative energy production has occurred recently as communities and governments push for further separation from fossil fuels to reduce green house gas emissions [119]. This reinvigorated government and citizen support quickly placed wind turbines in the optimal locations, however, as the number of turbines has drastically increased worldwide, the amount of land for optimal performance has been severely decreased. Therefore, to increase energy production from the wind, wind turbine arrays (often called wind farms) have begun to include larger numbers of wind turbines.

The problem now facing these larger wind farms is that the turbines which comprise the farm are designed to operate most efficiently within the undisturbed boundary layer flow, and when placed into these large arrays, are only allowed the wake of an upwind turbine for an inflow condition. The large arrays are most often, especially when placed off-shore, placed in a grid pattern. The result is that as the wind directions changes throughout the course of operation, so does the influence of these turbine-turbine interactions on total wind farm production. A preemptive study of the wind resource can provide great insight into how the wind farm should be designed and this wind evaluation can be coupled with the many different types of design optimizations currently being developed (i.e. [120, 121, 122]). However, no matter how well the array is designed initially, the layout will not completely eliminate the interaction of upwind turbine wakes on downwind turbines for all wind directions. Therefore, it is the goal

of the research presented herein to investigate modifications to wind turbine operation that can be implemented simply through new control algorithms. Specifically, wind turbine yaw misalignment and tip-speed ratio adjustment are inspected and compared to the standard aligned and staggered wind farms through experiments in a boundary layer wind tunnel.

This chapter is outlined as follows. Section 6.2 provides descriptions of the wind tunnel, model wind turbines used, particle image velocimetry (PIV) acquisition, and boundary layer profile. A table citing the experiments conducted and details on the wind farms tested are included in Section 6.2.1. The results for the simple design variables of streamwise spacing and turbine column alignment are presented in Section 6.3.1 while the test results for the performance modification of aligned wind arrays are introduced and discussed in Section 6.3.2. A brief summary and conclusions section is found thereafter.

6.2 Experimental setup

All the experiments utilized the small test section of the closed loop, atmospheric boundary layer wind tunnel at St. Anthony Falls Laboratory. The 200 horsepower fan propels the air into a 6.6:1 contraction just upwind of this test section, which has a total fetch of 16 m and a cross-section of 1.7 by 1.7 m. A trip of 0.040 m was placed at the entrance of the test section on the floor surface to induce turbulent mixing which accelerates boundary layer growth. After passing over the smooth aluminum floor panels, which can be thermally controlled independent of the air to a desired temperature between 10 ^oC and 80 ^oC, the boundary layer at a location corresponding to a position between the fourth and fifth rows of the $5D$ by $3D$ wind farm was measured to have a height of δ =0.6 m. The testing presented in this chapter was conducted under neutral stability where both the floor and air temperatures were 24 ^oC. Note here that great care was taken to adjust the ceiling of the wind tunnel test section to ensure that the pressure gradient was maintained with the model wind farms in place.

A hotwire anemometer probe was used to characterize the boundary layer in addition to understanding where the wall parallel PIV was positioned with respect to the boundary layer. The hotwire data is the same that was used for the previous chapter, therefore

Table 6.1: Boundary layer flow statistics for $U_{hub} \approx 5\ m\ s^{-1}$. Measurements conducted through the use of hot-wire anemometry.

δ $[m]$	u_τ $[m\ s^{-1}]$	U_{hub} $[m\ s^{-1}]$	U_δ $[m\ s^{-1}]$	Re_τ [-]	Re_D [-]	Re_δ [-]
0.6	0.23	5.0	5.91	9200	42977	236440

a quick summary is provided here. The boundary layer profile for $U_{hub} \sim 5m\ s^{-1}$ is presented in Figure 6.1. The corresponding Reynolds numbers Re_τ, Re_D and Re_δ are presented in Table 6.1, where $Re_\tau = u_\tau \times \delta/\nu$, $Re_D = U_{hub} \times D/\nu$ and $Re_\delta = U_\delta \times \delta/\nu$, u_τ is the shear velocity, δ is the boundary layer thickness and $\nu = 1.5 \times 10^{-5} m^2 s^{-1}$ is the kinematic viscosity of air at 24 ^oC. For exact details on the hotwire setup and acquisition the reader is directed to [58] and the previous chapter. The PIV was utilized only for a hub velocity $U_{hub} \sim 5m\ s^{-1}$, however, wind farm performance data were also taken at $U_{hub} = 3, 7, 10, 12, 15\ m\ s^{-1}$ also. This chapter only presents findings from the $5\ m\ s^{-1}$.

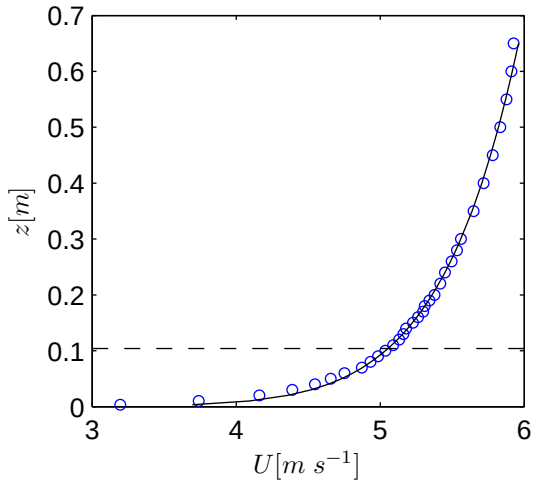

Figure 6.1: Boundary layer velocity profile as measured by the two component, hot-wire anemometer. The horizontal dashed line shows the turbine hub height where the wall-parallel PIV was captured. The solid black curve is a power law with an exponent of 0.09.

The wind turbine arrays were made up of individual model wind turbines with a fixed pitch, three-blade (GWS/EP-5030x3) rotor with a diameter D =0.128 m. As was the case for the previous two chapters in this thesis, the rotor was positioned with the high pressure surfaces facing the inflow and was directly connected to a DC generator mounted atop a mast with a height of 0.104 m (hub height). The generator was characterized in [58] to produce a differential voltage signal proportional to the rotor angular velocity with a linear variation in output with respect to the velocity. Under free-spinning conditions, the tip-speed ratio (TSR) is constant at $\approx$ 5.0, however, the TSR, and subsequently the power coefficient, can be modulated by applying an outside voltage to the generator opposing the turbine rotation direction. This ability to control the TSR was utilized for a portion of this testing presented below. The voltage data was acquired with a Measurement Computing DAQ board at 1000 Hz for 180 seconds, as previous examination of sampling time and frequency found that 180 seconds provides robust convergence for mean and higher order statistics.

A standard PIV system from TSI was positioned in a wall-parallel fashion linked two, 4 megapixel PowerView cameras and a Big Sky 532 nm Nd:Yag laser through a synchronizer and Insight 4G software. The resulting vector files produced by the two cameras were stitched together to provided a field of view (FOV) of roughly 3.6D ($\approx$ 0.46 m) by 1.8D (0.23 m). This FOV was positioned in two different ways for capturing flow details within the wind farm and were (i) the long axis (3.6D) aligned with the wind direction and (ii) the short axis (1.8D) aligned with the wind direction. Both FOVs were sampled between the fourth and fifth rows of the wind farm and are shown in Figure 6.2. The sampling region for FOV (i) started at 0.7D aft of the fourth row and was shifted off center to investigate the interaction of the turbine wake with the shear layer produced by the flow passing through the farm. FOV (ii) had a sampling region which was rotated 90^o with respect to FOV (i) and was placed to examine the flow into and through the fifth row of turbines. The PIV sampling rate was 7.25 Hz and the number of image pairs used herein was 2000. This number of vector fields ensured the convergence of the mean and higher order statistics.

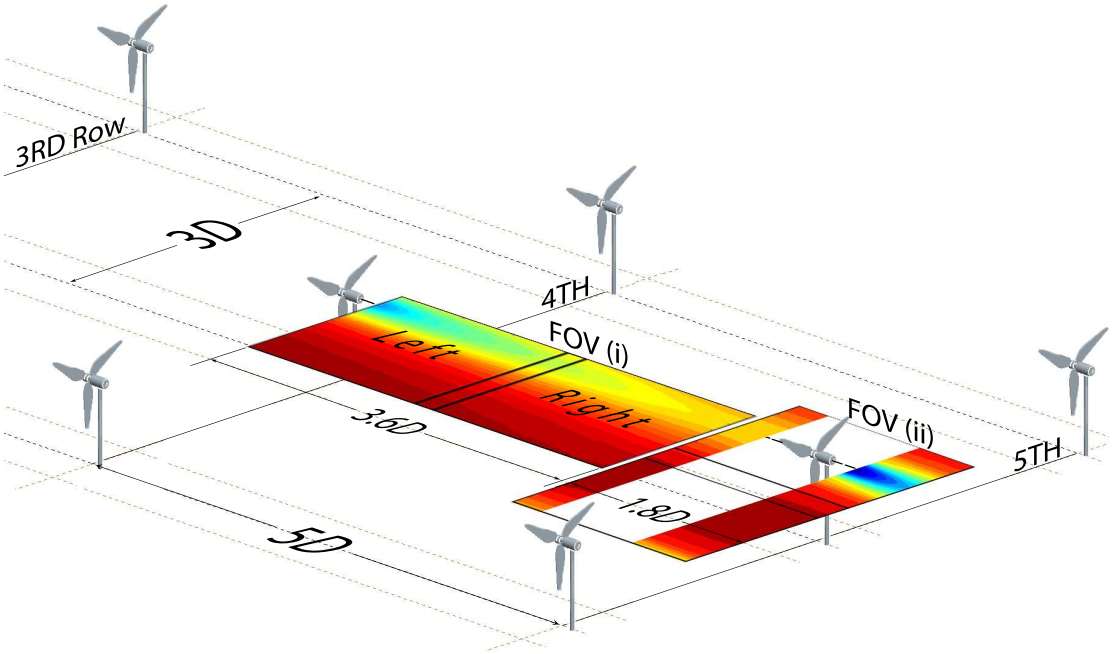

Figure 6.2: Schematic of PIV within the wind turbine array. When the cameras are aligned with the wind, the stitched left and right cameras are capturing a wall-parallel field of view at hub height with a total streamwise length of just under $3.6D$ (≈ 0.46 m) and spanwise breadth of 1.8 D (0.23 m). For the spanwise combined camera set up, the field of maintains the same dimension, but turned 90^o and is placed to capture flow through the fifth row of turbines.

6.2.1 Wind Farm Arrangements

Wind turbines in large on-shore wind farms are arranged primarily in a grid pattern, provided the terrain is relatively homogeneous. Also, these grid patterns of turbines are used for off-shore wind power production, and for example, the Horns Rev 1 off-shore wind farm has 80 turbines arranged in a eight by ten grid array (see [123] for more details). Optimizing the layout of the wind turbine arrays is the subject of significant current research ([120, 121, 122], etc.), however, moving installed turbines is not a cost effective solution for wind farms already in place. Therefore, herein we investigate the two ends of the spectrum for wind farm arrangements, which are aligned and staggered turbines, and the goal is to understand what changes to the control logic of existing turbines may be implemented to approach the total production for the staggered farm

Table 6.2: Wind farm array arrangements tested in the wind tunnel. l_x and l_y are the streamwise and spanwise turbine spacings, respectively. Yaw misalignment refers to the yaw γ of the front row of turbines. The TSR adjustment was implemented only on the front row, center turbine for this testing.

Wind farm spacing	$4D$ by $3D$	$5D$ by $3D$	$6D$ by $3D$
Aligned Columns	X	X	X
Staggered Columns		X	X
Yaw Misalignment	X		
TSR Adjustment		X	

when the turbines within the array are aligned. The spanwise spacing l_y is maintained throughout all testing, however, the streamwise distance l_x is changed between 4, 5 and $6D$ to inspect the change in total wind farm performance. In addition, two methods, (i) yaw misalignment and (ii) TSR adjustment, are examined to determine the modified wind farm performance in the aligned configuration. More details on the two modifications to the wind turbines are discussed in Section 6.3.2. The wind farm arrangement for all cases is presented in Table 6.2 and a top view schematic of the wind farms in question along with definitions of the coordinate system and PIV placement are shown in Figure 6.3. All data presented below was acquired for $U_{hub} \sim 5m\ s^{-1}$, measured in the undisturbed flow. For clarity, a row within the farm is defined as the turbine position in the streamwise direction, and a column is the turbine position in the spanwise direction. For example, the aligned farm presented in Fig. 6.3 is spaced l_x by l_y and has five rows and three columns.

6.3 Results and discussion

The voltage output from each of the turbines will be the main focus in this section and the PIV data will be used as supplemental information to elucidate why certain turbine arrangements perform in a specific manner.

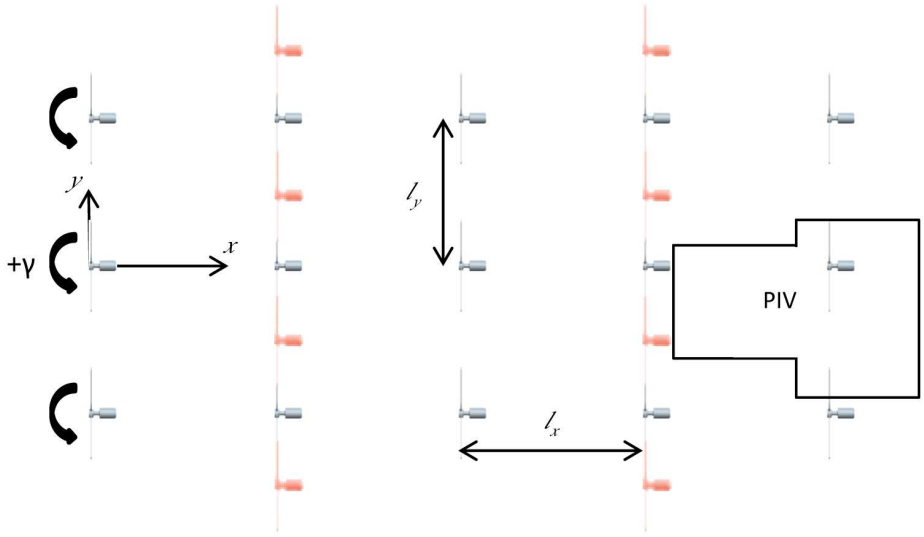

Figure 6.3: Schematic of wind farm arrangements for aligned (all gray turbines) and staggered (gray turbines of rows 1, 3, and 5 with the red turbines of rows 2 and 4). The positive yaw direction ($+\gamma$) is shown for the front row of turbines.

6.3.1 Wind farm arrangement design variables

Before a wind farm is installed, a measurement of the wind resource available at the selected site must be attained. At this point, the primary wind direction and magnitude will be known and the turbine layout can be designed. Here we look at the streamwise spacing l_x and column offset (staggered farm versus aligned) as design variables.

Streamwise spacing between rows

It is well known that increasing the spacing between turbines in an aligned array will increase production, and much research has shown the details of this (i.e. [124, 12, 125]). The following data on spacing is therefore to provide a baseline reference for the cases of aligned arrays with modified turbine control. Figure 6.4(a) shows that as the space between rows l_x is reduced from $6D$ down to $4D$, the mean production for each turbine, averaged across each row, is reduced by 10% as compared to the same row in the larger $6D$ spaced farm. The $5D$ case is reduced by roughly half, thus approximately 5% due to changing l_x= $6D$ to l_x= $5D$. Here the values are normalized by a single turbine

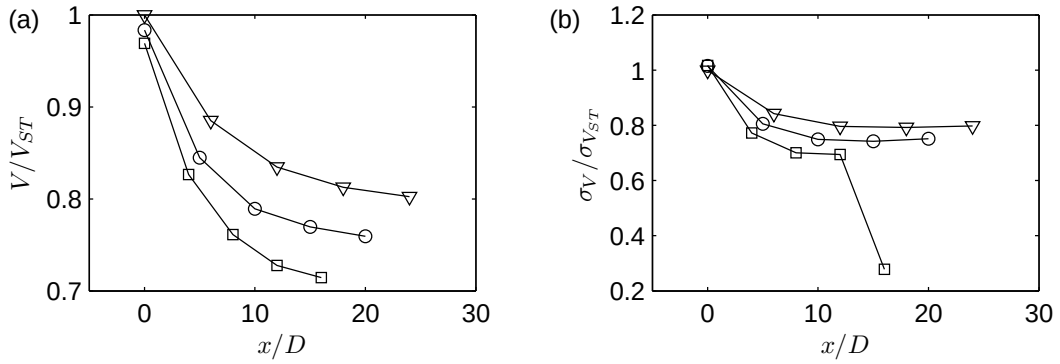

Figure 6.4: Comparison of streamwise spacing l_x for a wind farm at 5 $m\ s^{-1}$ as recorded by the center row of turbines. □, o and ▽ represent $l_x = 4D$, $5D$ and $6D$, respectively. V_{ST} and $\sigma_{V_{ST}}$ are the values of mean voltage production and fluctuations for the single turbine operating alone in the boundary layer.

operating in the boundary layer. The total power output from the entire turbine array was reduced from the $l_x = 6D$ case by 4% and 7% for the $l_x = 5D$ and $l_x = 4D$ farm spacings, respectively. Note that the $l_x = 6D$ case has a total loss of production of 13% as compared to the sum of 15 individual turbines producing at peak efficiency. Similar reductions in the output fluctuations (equivalent to turbine loading [58]) can be found by viewing Figure 6.4(b). The fluctuations recorded at the fifth row, center turbine are not correct, but are included for completeness.

An interesting feature of the difference in mean production between the different spacing is the decrease of output from the front row of turbines. As l_x is shortened, the front turbine mean output reduces slightly. As the cross sectional blockage has not changed, the reduction in production for the front row of turbines is assumed to be due to the increase in back pressure due to the proximity of the downwind turbine rows.

Staggered versus Aligned

Again, it is intuitive that the staggered farm will perform better for total output (shown by [126, 17, 127], etc.), but this data will provide at baseline reference for the model turbines used herein. Figure 6.5 displays the adjustment in performance for a staggered farm in comparison to an aligned farm for each turbine row, averaged across the three columns. The mean production change is shown in Fig. 6.5, and it can be seen that the

first row is nearly the same between the two farm arrangements. However, upon moving downwind in the farm, the next three rows in the staggered farm have an increase of over 15 % for individual performance. The increase for the second row is due to the funneling effect produced by the preceding row of turbines (due to the offset of the columns), such that the turbines in the second row are exposed to at least the original undisturbed hub velocity, if not a greater velocity. The remaining downwind rows (3, 4, and 5) also have a higher production due to the increased relative spacing between aligned turbines. Again due to the offset between the columns in the staggered wind farm, the relative streamwise spacing between a turbine directly aligned with another is actually twice the row spacing l_x. Therefore, the velocity deficit created by the upwind turbine has been far reduced by turbulent mixing within the farm by the time it reaches the downwind turbine. The increase of inflow velocity to the fifth row of turbines is shown in Figure 6.6. Here we note that the inflow velocity of the fifth row ($x/D = 19.5$, $y/D = 0$) in the aligned case is 0.65 of U_{hub} versus 0.80 of U_{hub} for the staggered. Also shown in Fig. 6.6 is that the flow velocity between the turbines is more homogeneous, as compared to the aligned, such that the shear layers created by the turbine wakes are not as intense (measured by the gradient of U in the y-direction). In summary, the staggered wind farm with $l_x = 5D$ and $l_y = 3D$ had an 11.9% increase in production over the aligned wind farm with the same spacing.

Figure 6.7 displays the percent change in fluctuations recorded by the rows of turbines in the staggered configuration, as compared to the array with aligned columns. Coupled with the increase in production is an increase in fluctuations of roughly the same magnitude. An interesting finding introduced in Chapter 3 was the change of large turbulent scale influenced by the terrain and by the thermal stability impacting the fluctuations measured by the wind turbine. It was shown in [58] that the turbulent flow scales do indeed influence the unsteady loading of the turbine and in [66] that the turbine homogenizes scales within the wake. To utilize these findings, we now investigate the turbulent length scale present within the wind farms and the changes in those length scales that occur between the aligned and staggered configurations, such that we can provide a better understanding for the increase in loading measured by the turbines within the staggered array.

The two-point correlation ($R_{u'u'}$) method introduced in Chapter 3 was implemented

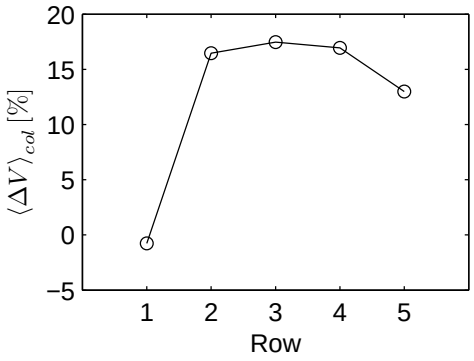

Figure 6.5: Change in wind turbine performance comparing staggered versus aligned wind farm. Percent change is shown for the mean output for each turbine row. The average for each row was computed using the three columns $\langle\rangle_{col}$. For the staggered case, every other row was shifted by $1.5D$, while l_x and l_y were constant between the cases at $5D$ and $3D$, respectively.

using two separate, fixed reference points within the FOV. As stated in the previous chapter, this method correlates the full velocity field with a velocity at a set reference location. The result provides statistical, quantitative information on the length and orientation of the dominant structures present in the flow. The equation is defined for a fixed reference point (x_{ref}, y_{ref}) as,

$$R_{u'u'}(x, y, x_{ref}, y_{ref}) = \frac{\langle u'(x_{ref}, y_{ref}, n)u'(x_{ref} + r_x, y_{ref} + r_y, n)\rangle_n}{\sigma_{u(x_{ref},y_{ref})}\sigma_{u(x_{ref}+r_x,y_{ref}+r_y)}}, \qquad (6.1)$$

where u' is the fluctuating velocity in the x-direction, r_x is the radius separating the two inspection points and n refers to the vector field number. The results are shown in Figure 6.8 for the aligned (a),(c) and staggered (b),(d) wind farms. The downwind (fifth) row for both aligned and staggered configurations is located at $x/D = 20$, and therefore, when comparing (a) and (b) in Fig. 6.8 it can be seen that the length scales present upwind of the center turbine ($y/D = 0$) are notably larger for the staggered array. This finding corroborates the increase in voltage fluctuations recorded by the turbines in the staggered configuration. The second fixed reference point, shown in Fig. 6.8 (c),(d), investigates the turbulent length scales present within the shear introduced by the wake of the preceding turbine row. The fixed reference point ($x/D = 16$, $y/D =$ -0.5) for the aligned case corresponds to the tip vortex location of the upwind turbine (rotor axis at $x/D = 15$) and we see that the shear layer which is produced between

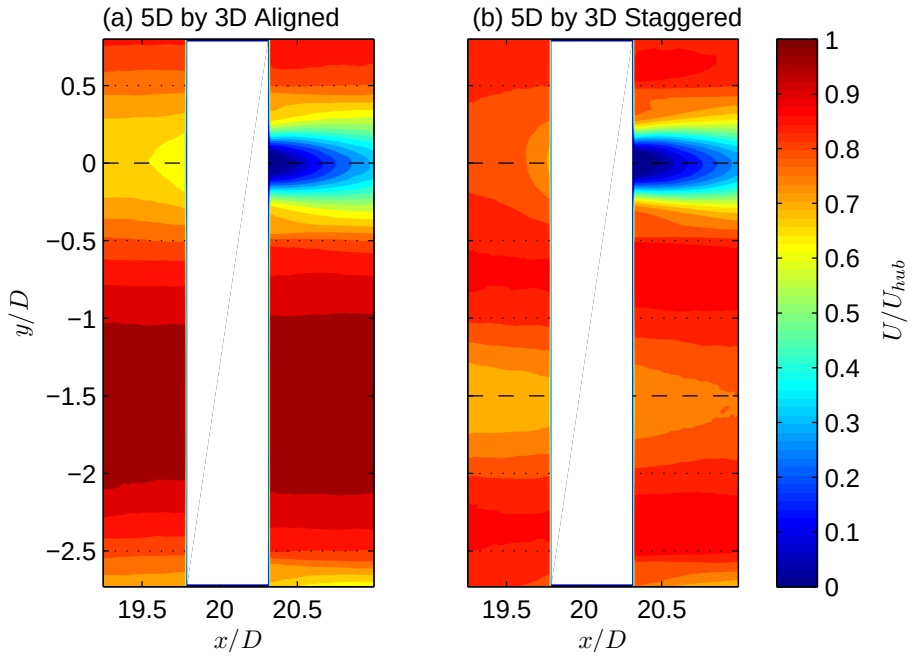

Figure 6.6: Flow comparison within (a) an aligned and (b) a staggered wind farm arrangement. For the staggered case, every other row was shifted by $1.5D$ and l_x and l_y were constant between the cases at $5D$ and $3D$, respectively. The horizontal dashed lines represent the centerline of turbine columns and the dashed lines represent the blade tip extremes.

the turbine wakes and the open channel [gap between rows, see Fig. 6.6(a)] is fairly weak, as measured by the spanwise growth of the correlation contours. Conversely, the staggered configuration shows a more confined shear layer in Fig. 6.8(d), which promotes turbulent mixing and subsequently, energy transfer within the wind turbine array [see Fig. 6.6(b)].

6.3.2 Performance changes for existing wind farms

Wind turbine arrays are placed in a location where the wind resource is known and are designed for a primary wind direction such that the turbines provide the best power production; however, the wind never comes from the same direction, meaning that for some duration of operation, the wind turbine array will be arranged in a sub-optimal orientation. While the production from a staggered wind farm is much higher than that

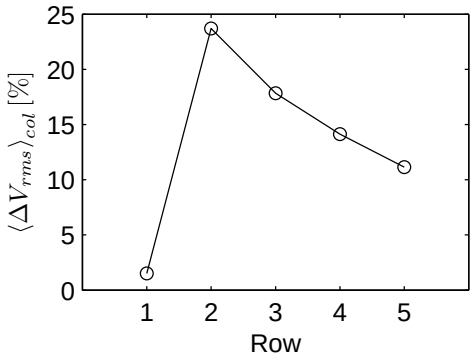

Figure 6.7: Change in wind turbine performance comparing staggered versus aligned wind farm. Percent change is shown for (b) mean r.m.s. for each turbine row. The average for each row was computed using the three columns $\langle \rangle_{col}$. For the staggered case, every other row was shifted by $1.5D$, while l_x and l_y were constant between the cases at $5D$ and $3D$, respectively.

of an aligned farm, a wind direction change (for instance a 45^o direction change) will turn a staggered designed wind farm into an aligned case. From above we in fact see that the aligned wind farm is least productive, and we now investigate two changes that may be implemented to pre-existing wind farms to increase production. It is the goal of this testing that a reduction in the performance of the front row of turbines will favor increased power production for the downwind turbines and as a result increase total production for the array. The principle is to adjust the operating condition of the front row to allow a more energy through, such that this higher energy will increase mixing and transport of mean kinetic energy to the remaining turbines downwind. The first adjustment is the yaw angle γ and the second is through adjustment of the tip-speed ratio (TSR), both inspected here on the front row of turbines. The wind turbine arrays inspected are $l_x = 4D$ and $l_y = 3D$ for the yaw adjustment testing and $l_x = 5D$ and $l_y = 3D$ for the TSR adjustment experiment.

Yaw misalignment effects on wind farm production

Yaw adjustment is one of the methods studied by Flemming et al. [128] to maximize the wind turbine array performance. They found that adjusting γ was able to shift wake in the spanwise direction, thereby changing the inflow condition for the downwind

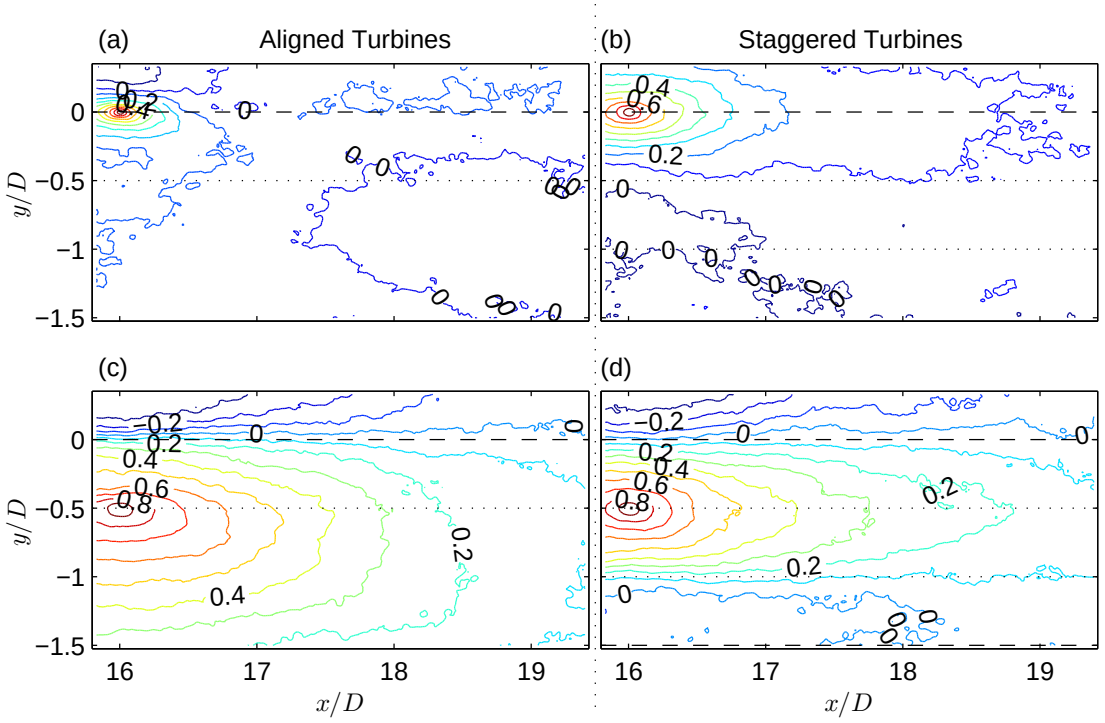

Figure 6.8: Correlation comparison produced within (a),(c) an aligned and (b),(d) a staggered wind farm arrangement. (a),(b) use the fixed reference point of $x/D = 16$, $y/D = 0$, while (c),(d) investigate the reference point of $x/D = 16$, y/D = -0.5. The preceding row is at $x/D = 15$ and the trailing row of turbines is at $x/D = 20$. The staggered case has the preceding row shifted by $1.5D$. The horizontal dashed lines represent the centerline of turbine columns and the dashed lines represent the blade tip extremes.

turbine. Also recorded from their computational study was a reduction in production due to the change in γ. While, Flemming et al. [128] were able to quantify performance and loading data for the individual turbine, the study only utilized one turbine and therefore did not provide details on the change in performance of downwind turbines. Note that another article has been submitted for publication by the same group that inspected the change induced on a single downwind turbine. Herein we move to study the impact of yaw misalignment on the 5 row by 3 column aligned wind farm.

Figure 6.9 presents the performance change ΔV $[= (V_{\gamma\neq 0} - V_{\gamma=0})/V_{\gamma=0}]$ for each individual turbine. The front row has an average reduction of about 4%, which is very

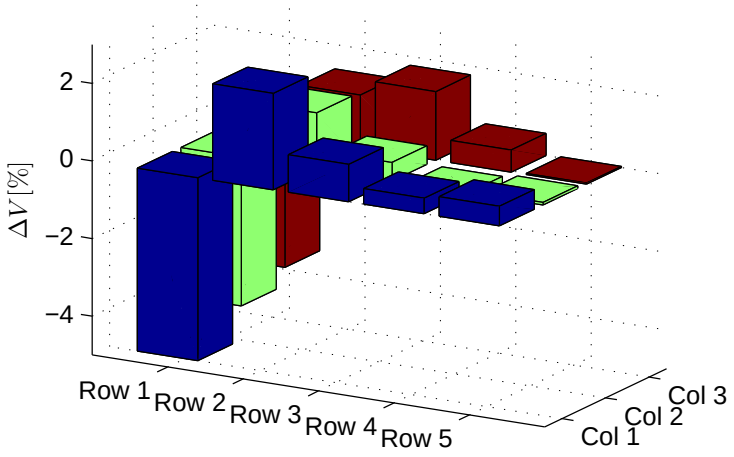

Figure 6.9: Production change for each turbine within the aligned wind farm with the each of the front turbines yawed + 15^o, as compared to the farm with front turbines with no yaw misalignment.

near to the 5.7% reduction found in Flemming et al. [128]. An increase in downwind turbine performance is noted, however, the average increase is only 1.7%. Rows 2 through 5 also show an increase in production, albeit lower than the second row, which is a measure of the increase of inflow velocity to the downwind turbines [58]. Table 6.3 shows that the yaw misalignment of the front row of turbines reduces the total production from the wind turbine array for all of the tested yaw configurations, due only to the drastic reduction in efficiency of the front three turbines. The front three turbines with yaw misalignment recorded reduced fluctuations (not shown), which equates to reduced variance in loading ([58]) and corroborates the findings presented by by Kragh and Hansen [129] and Felmming et al. [128]. However, as more flow is allowed to pass by the front turbine on to the remaining turbine rows, an increase in the fluctuations for the downwind turbines was recorded. Detailed flow analysis for the effect of turbine yaw angle remains for future work.

Table 6.3: Wind farm production comparison for various front row yaw γ angles. The streamwise l_x and spanwise l_y turbine spacings were held constant at $4D$ and $3D$, respectively. For the + and - angles, all of the turbines in the front row were yawed in the same direction. +/-, on the other hand, equates to the front row of turbines alternating from + 30^o to - 30^o between columns (i.e. if the front turbine in column 1 was turned - 30^o, the front turbine in column 2 was turned + 30^o, and so on for the remaining column). ΔV is the percentage change in total turbine production from the standard (no yaw misalignment) $4D$ by $3D$ aligned array.

γ [^{o}]	+ 30	+ 15	- 15	- 30	+/- 30
ΔV [%]	-1.1	-0.4	-0.3	-1.3	-1.6

TSR effects on wind farm production

The second area for modification of control strategies in existing wind farms is TSR adjustment. Adjusting the TSR is called many different names, including derating the turbine, changing the turbine induction factor and adjusting the thrust coefficient. The TSR of the model turbine used herein was controlled through applying an outside power source opposing the rotation direction of the DC generator on the turbine. This method was used in Howard et al. [58] to find the power coefficient (C_p) for the model turbine (note that the C_p curve presented in [58] is for a different blade orientation). The model turbine used for this wind farm testing, again, has a peak C_p of 0.27 at a TSR of 3.1. All of the testing presented previously has operated the turbine in a free-spinning (nearly zero load) state with a constant TSR of about 5.0. The previous chapter in this thesis inspected the change in wake characteristics due to changing the TSR, and we now extend the implementation of TSR adjustment to investigate wind farm performance through the evaluation of the individual turbines output.

The front, center turbine (row 1, column 2) was the only turbine to have TSR adjustment for this testing. Limiting the modification to a single turbine, rather than the entire front row, meant that we could inspect full wind farm performance changes linked to a specific turbine. Figure 6.10 shows the production of the wind farm with the front, center turbine operating at the minimal load case (higher TSR) relative to peak efficiency (lower TSR) for the aligned wind farm [$\Delta V = \left(V_{TSR=5.0} - V_{TSR=3.2}\right)/V_{TSR=3.2}$]. We

confirm that the front, center turbine is operating less efficiently at the lower TSR by observing an increase in voltage output from each of the turbines downwind [58]. When comparing to the yaw misalignment testing (Fig. 6.9), the change in production for the second, center turbine (row2, column 2) is greater than that of the yawed turbine.

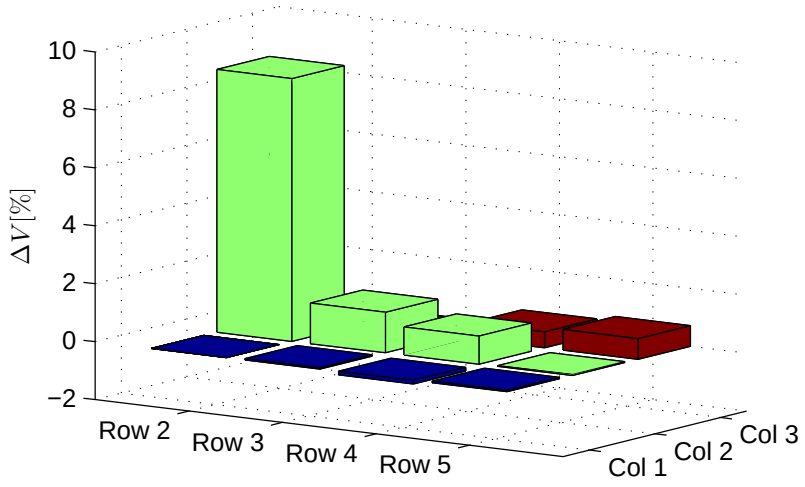

Figure 6.10: Production change for each turbine within the aligned wind farm with the front, center turbine operating at a TSR of 5.0 in reference to the case that has the front, center turbine with a TSR of approximately 3.2.

Total production difference for the last four rows of the aligned wind turbine array for five other TSRs are displayed in Table 6.4. The positive values equate to a gain in overall output with respect to the optimal TSR case (peak efficiency). The optimal TSR was utilized as the reference because in an existing utility-scale wind farm, the simple feed-back control logic for all of the turbines would attempt to operate each turbine at the optimal point given the inflow conditions, i.e. at a TSR of 3.2 for the model turbines here. Therefore, we see that even adjusting the TSR away from the peak efficiency for only the front, center turbine, registers an increase in overall performance. Like the loss of production for the yaw misalignment, however, a method for quantifying the change in production for the TSR adjusted turbine needs to be developed. This is another topic for future endeavors.

Table 6.4: Wind farm production comparison for different tip-speed ratios (TSR) of front row, center turbine. The streamwise l_x and spanwise l_y turbine spacings were held constant at $5D$ and $3D$, respectively. ΔV is the percentage change in total turbine production referencing the case when the front row, center turbine was operating at optimal TSR.

TSR	5.0	4.6	3.8	3.4	3.2	3.0
ΔV [%]	0.98	0.70	0.44	0.59	REF	0.17

6.4 Summary and Conclusions

The voltage outputs from model turbines and velocity data captured via a spatially resolved wall-parallel PIV setup were combined to investigate the effects of wind turbine array orientation on total production and output fluctuations (a measure of turbine loading [58]). Testing was conducted in the St. Anthony Falls Laboratory wind tunnel under neutral thermal conditions at several reference velocities. The results when comparing the production for the aligned and staggered wind farms confirmed that a staggered arrangement produces more power, precisely in this study, an 11.9% increase was found for a 5 $m\ s^{-1}$ reference hub velocity. Higher fluctuations were also recorded for the turbines within the staggered farm and were linked to an increase in turbulent length scales through the analysis of the fixed reference, two-point correlation.

While the staggered case is the best grid type design to implement when installing a wind turbine array, a wind direction shift from the primary wind direction will cause the turbines within the array to become an aligned wind farm. Therefore, beginning with the thought that all full-scale wind farms do not operate in the most efficient orientation due to wind direction changes, two methods of limiting individual wind turbine production (for the front row of turbines) were investigated in an attempt to increase total production from a wind turbine array with turbines aligned in the wind direction. The two modifications, that could be implemented into existing turbines through updated control logic, were (i) yaw misalignment and (ii) adjustment of tip-speed ratio (TSR). Method (i) was introduced to the front row of turbines and (ii) only to the front, center turbine. Interesting findings are:

- Yaw misalignment produces an increase in output for downwind turbines, however, the loss of production for the yawed turbine counteracts the gain. Also, while yaw misalignment reduces the loading of the specific turbine ([128, 129]), it increases the fluctuations felt by downwind turbines.

- Adjusting the TSR of a single turbine produced nearly 1% change in overall wind farm production, when comparing the the front, center turbine operating at an optimal TSR versus the same turbine with a higher one TSR. The increase in notable for the farm production, however, a method to quantify change in production of the model turbine due to TSR adjustment needs to be developed to truly inspect total production modification.

- For a relative comparison between yaw misalignment and TSR adjustment, the output for the second turbine in the center column is inspected and found that TSR adjustment allowed the downwind turbine to produce 9% (at $l_x = 5D$) more over the reference case, whereas for yaw misalignment the second, center column turbine only produces 1.4% (at $l_x = 4D$) more.

The data introduced in this chapter shed light on flow intricacies within wind farms and presented a few ideas that can be implemented for aligned wind farms to increase production.

Chapter 7

Summary of findings

The operation of harnessing power from the wind appears like an easy task on the surface, as humans have utilized the wind as a resource for centuries. However, as presented in this thesis, in order to be more effective at capturing energy from our invisible ally, the intricate details of turbulent flows, surface roughness influence, lift production and subsequent wake development, and control algorithm influence, to name a few, is required. The research presented herein has provided the wind energy community with many new techniques and findings to further the understanding of what makes wind turbines spin, and how turbines and surrounding environment interact with one another.

A list of the most significant tools and findings from this research is presented below.

- The wind turbine model and related diagnostic tools: utilizing a scaled turbine rotor attached to a simple DC generator, the performance of a turbine placed in any wind tunnel situation can be monitored through the voltage output of the DC generator.

- Thermal stability and terrain influence on turbine operation: findings presented information that the change in turbulence levels for the given thermal stability do impact the mean production and fluctuations (loading) of the turbine; in the case of inhomogeneous terrain, the thermal regime does not precisely dictate the turbine loading, however it is influenced by a complex link between the terrain and thermal stability.

- Wind turbine scale model flow representativeness: research was conducted at both the model-scale and full-scale and it was found that the model turbine responds to inflow conditions similarly (even noting the significant change in rotational inertia between the two scales), and produces a mean wake profile which is very representative for downwind distances larger than $x/D = 1.5$.

- Upwind preview information (used primarily for load reduction): correlation of velocity time signals (measured by a lidar) to the full-scale turbine's power production and structural loading produced a correlation (it is a wind turbine after all) and, most significantly, were most correlated for (i) an averaged time signal over the entire rotor and (ii) an elevation of $z/z_{hub} \approx 1.3$, corresponding to $z \approx z_{hub} + D/4$; these findings were corroborated by experiments conducted in the wind tunnel for the model turbines as well.

- Turbine near wake meandering: statistical evidence of wake meandering in a horizontal slice of the turbine wake was presented and found that (i) the hub wake expansion is not symmetrical about the mean wake centerline, (ii) the fluctuations about the filtered wake signal have a signature unique to their y location in the wake and (iii) the wake meandering is found to be a multiscale process.

- Aligned wind farm performance increase: adjusting the tip-speed ratio of a front turbine had the greatest influence on the following rows and increased the production of the four downwind turbine rows by 1%; the turbine directly behind the tip-speed ratio adjusted turbine had a production increase of 9%.

References

[1] Howard K B, Chamorro L P, and Guala M. An experimental case study of complex topographic and atmospheric influences on wind turbine performance. *AIAA Aerospace Sciences Meeting*, (Grapevine, TX, January), 2013.

[2] Old technology: a short history of wind power. *Countryside and small stock J.*, 82:80, 1998.

[3] Hosansky D. Wind power. *CQ Researcher*, 21:289–312, 2011.

[4] Nielsen K H. Technological trajectories in the making: two case studies from the contemporary history of wind power. *Centaurus*, 52:175–205, 2010.

[5] Buck J W and Renne D S. Observations of wake characteristics at the goodnoe hills mod-2 array. *National technical information service, U.S.*, 1985.

[6] Okulov V L and Sørensen J N. Refined betz limit for rotors with a finite number of blades. *Wind Energ.*, 11:415–426, 2008.

[7] Chamorro LP and Arndt R E A. Non-uniform velocity distribution effect on the betz-joukowsky limit. *Wind Energ.*, 16:279–282, 2013.

[8] Griffith D T and Ashwill T D. The sandia 100-meter all-glass baseline wind turbine blade: Snl100-00. *Sandia Nationa Laboratories*, (SAND2011-3779), 2011.

[9] Global wind energy council. Global wind statistics 2013. 2014.

[10] Yang Z, Oxbay A, Sarkar P, and Hu H. An experimental investigation on the wake interference of wind turbines sited over complex terrains. *AIAA Aerospace Sciences Meeting*, 2012.

[11] O'Sullivan J P, Pecnik R, and Iaccarino G. Investigating turbulence in wind flow over complex terrain. *Proceedings of the Summer Program*, (129), 2010.

[12] Yang X, Kang S, and Sotiropoulos F. Computational study and modeling of turbine spacing effects in infinite aligned wind farms. *Phys. Fluids*, 24(doi: 10.1063/1.4767727), 2012.

[13] Troldborg N, Larsen G C, Madsen H A, Hansen K S, Sørensen J N, and Mikkelsen R. Numerical simulations of wake interaction between two wind turbines at various inflow conditions. *Wind Energ.*, 14:859–876, 2011.

[14] Politis E S, Prospathopoulos J, Cabezón D, Hansen K S, Chaviaropoulos P K, and Barthelmie R J. Wake effects in large wind farms in complex terrain: the problem, the methods and the issues. *Wind Energ.*, 15:161–182, 2012.

[15] Gravdahl A R, Rorgemoen S, and Thogersen M. Power prediction and siting–when the terrain gets rough. *The World Wind Energy Conference and Exhibition*, 2002.

[16] Hu H, Yang Z, and Sarkar P. Dynamic wind loads and wake characteristics of a wind turbine model in an atmospheric boundary layer wind. *Exp. in Fluids*, 52:1277–1294, 2012.

[17] Chamorro L P, Arndt R E A, and Sotiropoulos F. Turbulent flow properties around a perfectly staggered wind farm. *Boundary-Layer Meteorology*, 141:349–367, 2011.

[18] Tampieri F, Mammarella I, and Maurizi A. Turbulence in complex terrain. *Bound.-Layer Meteorol.*, 109:85–97, 2003.

[19] Chamorro L P and Porté-Agel F. Velocity and surface shear stress distributions behind a rough-to-smooth surface transition: A simple new model. *Boundary-Layer Meteorology*, 130:29–41, 2009.

[20] Chamorro L P and Porté-Agel F. A wind-tunnel investigation of wind-tubine wakes: Boundary-layer turbulence effects. *Boundary-Layer Meteorology*, (132):129–149, 2009.

[21] Gonzáles-Longatt F, Wall P, and Terzija V. Wake effect in wind farm performance: steady-state and dynamic behavior. *Renewable Energ.*, 39:329–338, 2012.

[22] Husien W, El-Osta W, and Dekam E. Effect of the wake behind wind rotor on optimum energy output of wind farms. *Renew. Energ.*, 49:128–132, 2013.

[23] Meneveau C. The top-down model of wind farm boundary layers and its applications. *Journal of Turbulence*, 13(N7), 2012.

[24] Cal R B, Lebron J, Castillo L, Kang H S, and Meneveau C. Experimental study of the horizontally averaged flow structure in a model wind-turbine array boundary layer. *Journal of Renewable and Sustainable Energ.*, 2(013106), 2010.

[25] Lebron J, Castillo L, and Meneveau C. Experimental study of the kinetic energy budget in a wind turbine streamtube. *J. of Turbul.*, 13(N43), 2012.

[26] Guala M, Metzger M, and McKeon B J. Interactions within the turbulent boundary layer at high reynolds number. *J. Fluid Mech.*, 666:573–604, 2011.

[27] Chamorro L P, Arndt R E A, and Sotiropoulos F. Reynolds number dependence of turbulence statistics in the wake of wind turbines. *Wind Energ.*, 15, 2012.

[28] Brunn H H. Hotwire anemometry: principles and signal analysis. *Oxford University Press, U.K.*, page 507, 1995.

[29] Chamorro L P, Hill C, Morton S, Ellis C, Arndt R E A, and Sotiropoulos F. On the interaction between a turbulent open channel flow and an axial-flow turbine. *J. of Fluid Mech.*, 716:658–670, 2013.

[30] von Kármán T. *Nachr. Ges. Wissenschaft. Göttingen*, pages 509–517, 1911.

[31] Chamorro L P, Guala M, Arndt R E A, and Sotiropoulos F. On the evolution of turbulent scales in the wake of a wind turbine model. *J. of Turbulence*, 13:1–13, 2012.

[32] Balakumar B and Adrian R. Large scale and very large scale motions in turbulent boundary layers and channel flows. *Phil. Trans. R. Soc. A*, (365):665–681, 2007.

[33] Adrian R. Hairpin vortex organiation in wall turbulence. *Phys. of Fluids*, 19(doi: 10.1063/1.2717527), 2007.

[34] Vermeer L J, Sørensen J N, and Crespo A. Wind turbine wake aerodynamics. *Prog. Aerospace Sci.*, 39:467–510, 2003.

[35] Sørensen J N. Aerodynamic aspects of wind energy conversion. *Annu. Rev. Fluid Mech.*, 43:427–448, 2011.

[36] S Frandsen. On the wind-speed reduction in the center of large clusters of wind turbines. *J. Wind Eng. Ind. Aerodyn.*, 39:251–265, 1992.

[37] Corten GP, Schaak P, and Hegberg T. Velocity profiles measured above a scaled wind farm. *Eur. Wind Conference*, 2004.

[38] Chamorro L P and Porté-Agel F. Turbulent flow inside and above a wind farm: a wind-tunnel study. *Energies*, 4:1916–1936, 2011.

[39] Ivanova L A and Nadyozhina E D. Numerical simulation of wind farm influence on wind flow. *Wind Energ.*, 24:257–269, 2000.

[40] Calaf M, Meneveau C, and Parlange M. Large eddy simulation study of a fully developed thermal wind turbine array boundary layer. *Direct and Large-Eddy Simulation VIII*, 15:239–244, 2011.

[41] Porté-Agel F, Wu Y T, Lu H, and Conzemius R J. Large-eddy simulation of atmospheric boundary layer flow through wind turbines and wind farms. *J. Wind Eng. Ind. Aerodyn.*, 99:154–168, 2011.

[42] Stull R B. *An introduction to boundary-layer meteorology.* Kluwer Academic Publishers, Dordrecht, 1988.

[43] Zhang W, Markfort C D, and Porté-Agel F. Wind turbine wakes in a convective boundary layer: a wind-tunnel study. *Bound.-Layer Meteorol.*, 146:161–179, 2013.

[44] Brunet Y, Finnigan J J, and Raupach M R. A wind-tunel study of air flow in waving wheat: single-point velocity statistics. *Bound.-Layer Meteorol.*, 70:95–132, 1994.

[45] Ishihara T, Hibi K, and Oikawa S. A wind tunnel study of turbulent flow over a three-dimensional steep hill. *J. Wind Eng. Ind. Aerodyn.*, 83:95–107, 1999.

[46] Finnigan J J, Raupach M R, Bradley E F, and Aldis G K. A wind tunnel study of turbulent flow over a two-dimensional ridge. *Bound.-Layer Meteorol.*, 50:277–317, 1990.

[47] Castro I P and Snyder W H. A wind tunnel study of dispersion from sources downwind of three-dimensional hills. *Atm. Envir.*, 16:1869–1887, 1982.

[48] Arya S P S and Gadiyaram P S. An experimental study of flow and dispersion in the wakes of three-dimensional low hills. *Atm. Envir.*, 20:729–740, 1986.

[49] Snyder W H and Britter R E. A wind tunnel study of the flow structure and dispersion from sources upwind of three-dimensional hills. *Atm. Envir.*, 21:735–751, 1987.

[50] Finnigan J J and Brunet Y. Ï-turbulent airflow in forests on flat and hilly terrain¨. In Ed. Grace J Coutts MP, editor, *Wind and trees*, pages 3–40. Cambridge University Press, New York, NY, 2004.

[51] Carpenter P and Locke N. Investigation of wind speeds over multiple two-dimensional hills. *J. Wind Eng. Ind. Aerodyn.*, 83:109–120, 1999.

[52] Kanda I, Yamao Y, Uehara K, and Wakamatsu S. Particle-image velocimetry measurements of separation and re-attachment of airflow over two-dimensional hills with various slope angles and approach-flow characteristics. *Bound.-Layer Meteorol.*, (DOI 10.1007/s10546-013-9806-1), 2013.

[53] Ayotte K W and Hughes D E. Observations of boundary-layer wind-tunnel flow over isolated ridges of varying steepness and roughness. *Bound.-Layer Meteorol.*, 112:525–556, 2004.

[54] Harman I N and Finnigan J J. Flow over a narrow ridge covered with a plant canopy: a comparison between wind-tunnel observations and linear theory. *Bound.-Layer Meteorol.*, 147:1–20, 2013.

[55] Neff D E and Meroney R N. Wind-tunnel modeling of hill and vegetation influence on wind power availability. (Proceedings from 2nd European and African conference on wind engineering, June), 1997.

[56] Takahashi T, Kato S, Murakami S, Ooka R, Yassin M F, and Kono R. Wind tunnel tests of effects of atmospheric stability on turbulent flow over a three-dimensional hill. *J. Wind Eng. Ind. Aerodyn.*, 93:155–169, 2005.

[57] Cheng Y, Parlange M B, and Brutsaert W. Pathology of monin-obukhov similarity in the stable boundary layer. *JGR: Atmospheres*, 110, 2005.

[58] Howard K B, Hu J S, Chamorro L P, and Guala M. Characterizing the response of a wind turbine model under complex inflow conditions. *Wind Energ.*, (doi: 10.1002/we.1724), 2014.

[59] Yang X, Howard K B, Guala M, and Sotiropoulos F. Effects of a three-dimensional hill on the wake characteristics of a model wind turbine. *Phys. Fluids*, (Submitted 14-0664).

[60] Melling A. Tracer particles and seeding for particle image velocimetry. *Meas. Sci. Technol.*, 8:1406–1416, 1997.

[61] Adrian R J, Meinhart C D, and Tomkins C D. Vortex organization in the outer region of the turbulent boundary layer. *J. Fluid Mech.*, 422:1–54, 2000.

[62] Chauhan K, Hutchins N, Monty J, and Marusic I. Structure inclination angles in the convective atmospheric surface layer. *Bound.-Layer Meteorol.*, 147:41–50, 2013.

[63] Marusic I and Heuer W D C. Reynolds number invariance of the structure inclination angle in wall turbulence. *Physical Rev. Letters*, 99(114504), 2007.

[64] Wu Y and Christensen K T. Spatial structure of a turbulent boundary layer with irregular surface roughness. *J. Fluid Mech.*, 655:380–418, 2010.

[65] Carper M A and Porté-Agel F. The role of coherent structures in subfilter-scale dissipation of turbulence measured in the atmospheric surface layer. *J. Turbul.*, 5(N40), 2004.

[66] Singh A, Howard K B, and Guala M. On the homogenization of turbulent flow structures in the wake of a model wind turbine. *Phys. Fluids*, 26(2), 2014.

[67] Hutchins N and Marusic I. Evidence of very long meandering features in the logarithmic region of turbulent boundary layers. *J. Fluid Mech.*, 579:1–28, 2007.

[68] Smits A J, McKeon B J, and Marusic I. High-reynolds number wall turbulence. *Annu. Rev. Fluid Mech.*, 43:353–75, 2011.

[69] American Wind Energy Association (AWEA). AWEA 1st quarter 2012 public market report. 2012.

[70] Buckney N, Green S, Pirrera A, and Weaver P M. On the structural topology of wind turbine blades. *Wind Energ.*, 16:545–560, 2013.

[71] Muljadi E and Butterfield C P. Pitch-controlled variable-speed wind turbine generation. *IEEE Industry Applications Society Annual Meeting*, (Phoenix, October), 1999.

[72] Larsen T J, Madsen H A, and Thomsen K. Active load reduction using individual pitch, based on local blade flow measurements. *Wind Energ.*, 8:67–80, 2005.

[73] Ozdemir A A, Seiler P J, and Balas G J. Performance of disturbance augmented control design in turbulent wind conditions. *Mechatronics*, 21:634–644, 2011.

[74] Johnson S J, Larwood S, McNerney G, and van Dam C P. Balancing fatigue damage and turbine performance through innovative pitch control algorithm. *Wind Energ.*, 15:665–677, 2012.

[75] van Wingerden J W, Hulskamp A W, Barlas T, Marrant B, van Kuik G, Molenarr D P, and Verhaegen M. On the proof of concept of a 'smart' wind turbine rotor blade for load alleviation. *Wind Energ.*, 11:265–280, 2008.

[76] Lackner M A and van Kuik G. A comparison of smart rotor control approaches using trailing edge flaps and individual pitch control. *Wind Energ.*, 13:117–134, 2010.

[77] Johnson S J, Baker J P, van Dam C P, and Berg D. An overview of active load control techniques for wind turbine with an emphasis on microtabs. *Wind Energ.*, 13:239–253, 2010.

[78] Dunne F, Pao L Y, Wright A D, Jonkman B, and Kelly N. Combining standard feedback controllers with feedforward blade pitch control for load mitigation in wind turbines. *AIAA Aerospace Sciences Meeting*, (Orlando, January), 2010.

[79] Simley E, Pao L Y, Kelly N, Jonkman B, and Frehlich R. Lidar wind speed measurements of evolving wind fields. *AIAA Aerospace Sciences Meeting*, (Nashville, January), 2012.

[80] Mikkelsen T, Angelou N, Hansen K, Sjöholm M, Harris M, Slinger C, Hadley P, Scullion R, Ellis G, and Vives G. A spinner-integrated wind lidar for enhanced wind turbine control. *Wind Energ.*, 16:625–643, 2013.

[81] Moriarty P J, Holley W E, and Butterfield S. Effect of turbulence variation on extreme loads prediction for wind turbines. *J. Sol. Energ. Eng.*, 124:387–395, 2002.

[82] Howard K B and Guala M. Characterizing the effects of inflow on a 2.5 mw research utility turbine. *AIAA SciTech*, (32nd ASME Wind Energy Symposium, National Harbor, Maryland, January), 2014.

[83] Chamorro L P and F Porté-Agel. Effects of thermal stability and incoming boundary-layer flow characteristics on wind-turbine wakes: A wind-tunnel study. *Boundary Layer Metereology*, 136:515–533, 2010.

[84] Li D and Bou-Zeid E. Coherent structures and the dissimilarity of turbulent transport of momentum and scalars in the unstable atmospheric surface layer. *Bound.-Layer Meteorol.*, 140:243–262, 2011.

[85] Bou-Zeid E, Higgins C, Huwald H, Meneveau C, and Parlange M B. Field study of the dynamics and modelling of subgrid-scale turbulence in a stable atmospheric surface layer over a glacier. *J. Fluid Mech.*, 665:480–515, 2010.

[86] Rhodes M E and Lundquist J K. The effect of wind-turbine wakes on summertime us midwest atmospheric wind profiles as observed with ground-based doppler lidar. *Bound.-Layer Meteorol.*, 149:85–103, 2013.

[87] Abdelsalam A M, Boopathi K, Gomathinayagam S, Hari Krishnan Kumar S S, and Ramalingam V. Experimental and numerical studies on the wake behavior of a horizontal axis wind turbine. *J. Wind Eng. Ind. Aerodyn.*, 128:54–65, 2014.

[88] Mikkelsen T. On mean wind and turbulence profile measurements from ground-based wind lidars: limitations in time and space resolution with continuous wave and pulsed lidar systems - a review. (Wind Energy Division, Risø National Laboratory for Sustainable Energy, Technical University of Denmark).

[89] Medici D, Ivanell S, Dahlberg J Å, and Alfredsson P H. The upstream flow of a wind turbine: blockage effect. *Wind Energ.*, 14:691–697, 2011.

[90] Leopold L B and Langbein W B. River meanders. *Scientific American*, 214:60–70, 1966.

[91] Howard A D and Hemberger A T. Multivariate characterization of meandering. *Geomorphology*, 4:161–186, 1991.

[92] Seminara G. Fluvial sedimentary patterns. *Ann. Rev. Fluid Mech.*, 42:43–66, 2010.

[93] Peakall J, McCaffrey B, and Kneller B. A process model for the evolution, morphology, and architecture of sinuous submarine channels. *J. of Sedimentary Res.*, 70:434–448, 2000.

[94] Seminara G. Meanders. *J. Fluid Mech*, 554:271–297, 2006.

[95] Lauer J W and Parker G. Net local removal of floodplain sediment by river meander migration. *Geomorphology*, 96:123–149, 2008.

[96] Meiburg E and Kneller B. Turbidity currents and their deposits. *Ann Rev. of Fluid Mech.*, 42:135–156, 2010.

[97] Nelson P A and Seminara G. A theoretical framework for the morphodynamics of bedrock channels. *Geophys. Res. Lett.*, 39(L06408), 2012.

[98] Dracos T M, Giger M, and Jirka G H. Plane turbulent jets in a bounded fluid layer. *J. Fluid Mech.*, 241:587–614, 1992.

[99] Rowland J C, Stacey M T, and Dietrich W E. Turbulent characteristics of a shallow wall-bounded plane jet: experimental implications for river mouth hydrodynamics. *J. Fluid Mech.*, 627:423–449, 2009.

[100] Landel J R, Cauleld C P, and Woods A W. Meandering due to large eddies and the statistically self-similarity of quasi-two-dimensional jets. *J. Fluid Mech.*, 692:247–268, 2012.

[101] Mariotti G, Falcini F, Geleynse N, Guala M, and Fagherazzi S. Why meandering turbulent jets have high sediment eddy diffusivity: implications for levees formation. *J Geophys. Res. Earth*, 118:1908–1920, 2013.

[102] Medici D and Alfredsson P H. Measurements behind model wind turbines: Further evidence of wake meandering. *Wind Energ.*, 11:211–217, 2008.

[103] Espa na G, Aubrun S, Loyer S, and Devinant P. Spatial study of the wake meandering using modelled wind turbines in a wind tunnel. *Wind Energ.*, 14:923–937, 2011.

[104] Okulov V L, Naumov I V, Robert F, Mikkelsen R F, Kabardin I K, and Sorensen J N. A regular strouhal number for large-scale instability in the far wake of a rotor. *J. Fluid Mech.*, 747:369–380, 2014.

[105] Ainslie J F. Development of an eddy viscosity model for wind turbine wakes. (Proceedings of the 7th British Wind Energ. Association Conference, Oxford, March):61–66, 1985.

[106] Bastankhah M and Porté-Agel F. A new analytical model for wind-turbine wakes. *Renew. Energ.*, 70:116–123, 2014.

[107] Panton R L. *Incompressible flow.* John Wiley & Sons, Inc., Hoboken, New Jersey, 2005.

[108] Frandsen S, Barthelmie R, Pryor R, Rathmann O, Larsen S, Hojstrup J, and Thogersen M. Analytical modelling of wind speed deficit in large offshore wind farms. *Wind Energ.*, 9:39–53, 2006.

[109] Larsen G C, Madsen H A, Thomsen K, and Larsen T J. Wake meandering: a pragmatic approach. *Wind Energ.*, 11:377–395, 2008.

[110] Barthelmie R J, Folkerts L, Larsen G C, Rados K, Pryor S C, Frandsen S T, Lange B, and Schepers G. Comparison of wake model simulations with offshore wind turbine wake profiles measured by sodar. *J. Atm. Oceanic Tech.*, (doi:10.1175/JTECH1886.1), 2006.

[111] Whale J, Papadopoulos K H, Anderson C G, Helmis C G, and Skyner D J. A study of the near wake structure of a wind turbine comparing measurements from laboratory and full-scale experiments. *Solar Energ.*, 56:621–633, 1996.

[112] Whale J, Anderson C G, Bareiss R, and Wagner S. An experimental and numerical study of the vortex structure in the wake of a wind turbine. *J. Wind Eng. Ind. Aerodyn.*, 84:1–21, 2000.

[113] Medici D and Alfredsson P H. Measurements on a wind turbine wake: 3d effects and bluff body vortex shedding. *Wind Energ.*, 9:219–236, 2006.

[114] Kang S, Yang X, and Sotiropoulos F. On the onset of wake meandering for an axial flow turbine in a turbulent open channel flow. *J. Fluid Mech.*, 744:376–403, 2014.

[115] Adrian R J, Christensen K T, and Liu Z C. Analysis and interpretation of instantaneous turbulent velocity fields. *Exp. Fluids*, 29:275–290, 2000.

[116] Swearingen J D, Crouch J D, and Handler R A. Dynamics and stability of a vortex ring impacting a solid boundary. *J. Fluid Mech.*, 297:1–28, 1995.

[117] Malecot Y, Auriault C, Kahalerras H, Gagne Y, Chanal O, Chabaud B, and Castaing B. A statistical estimator of turbulence intermittency in physical and numerical experiments. *Eur. Phys. J. B.*, 16:549–561, 2000.

[118] Singh A, Foufoula-Georgiou E, Porté-Agel F, and Wilcock P R. Coupled dynamics of the co-evolution of gravel bed topography, flow turbulence and sediment transport in an experimental channel. *J. Geophys. Res.*, 117(F04016, doi:10.1029/2011JF002323), 2012.

[119] U.S. Department of Energy. 20% wind energy by 2030: Increasing wind energy's contribution to u.s. electricity supply. 2008.

[120] Chowdhury S, Zhang J, Messac A, and Castillo L. Unrestricted wind farm layout optimization (uwflo): investigating key factors influencing the maximum power generation. *Renew. Energ.*, 38:16–30, 2012.

[121] Wagner M, Day J, and Neumann F. A fast and effective local search algorithm for optimizing the placement of wind turbines. *Renew. Energ.*, 51:64–70, 2013.

[122] Chowdhury S, Zhang J, Messac A, and Castillo L. Optimizing the arrangement and the selection of turbines for wind farms subject to varying wind conditions. *Renew. Energ.*, 52:273–282, 2013.

[123] Hasager C B, Rasmussen L, Pe na A, Jensen L E, and Réthoré P-E. Wind farm wake: the horns rev photo case. *Energies*, 6:696–716, 2013.

[124] Meyers J and Meneveau C. Optimal turbine spacing in fully developed wind farm boundary layers. *Wind Energ.*, 15:305–317, 2012.

[125] Son E, Lee S, Hwang B, and Lee S. Characteristics of turbine spacing in a wind farm using an optimal design process. *Renew. Energ.*, 65:245–249, 2014.

[126] Markfort C D, Zhang W, and Porté-Agel F. Turbulent flow and scalar transport through and over aligned and staggered wind farms. *J. Turb.*, 13:1–36, 2012.

[127] Ozbay A. Experimental investigations on the wkae interferences of multiple wind turbines. *Graduate Theses and Dissertations*, (Paper 12427), 2012.

[128] Fleming P A, Gebraad P M O, Lee S, van Wingerden J-W, Johnson K, Churchfield M, Michalakes J, Spalart P, and Moriarty P. Evaluating techniques for redirecting turbine wkae using sowfa. *Renew. Energ.*, 70:211–218, 2014.

[129] Kragh K A and Hansen M H. Load alleviation of wind turbines by yaw misalignment. *Wind Energ.*, 17:971–982, 2014.